Modelling the lateral flow and sediment dynamics in esturaries

E. J. Burgers

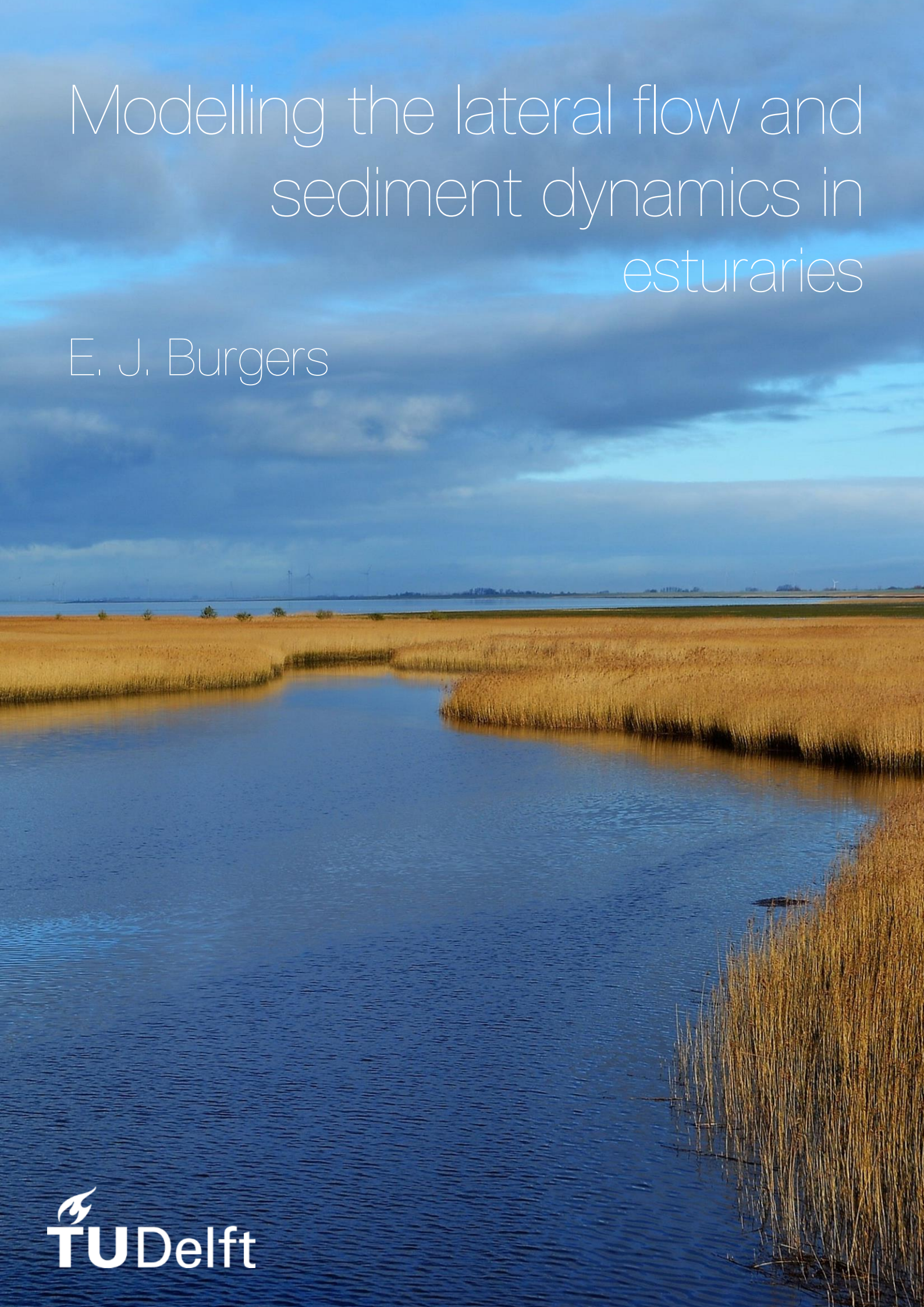

TU Delft

Modelling the lateral flow and sediment dynamics in estuaries

by

E.J. Burgers

to obtain the degree of Master of Science
at the Delft University of Technology,
to be defended publicly on Thursday November 26, 2020 at 14:30.

Student number:	4395476	
Project duration:	February 10, 2020 – November 26, 2020	
Thesis committee:	Dr. J. L. A. Dubbeldam	TU Delft
	Dr. ir. M. B. van Gijzen	TU-Delft
	Dr. H. M. Schuttelaars,	TU Delft, supervisor
	Ir. T. J. Zitman,	TU Delft, supervisor

An electronic version of this thesis is available at `http://repository.tudelft.nl/`.

TU Delft

Abstract

Estuaries have always been important for mankind and therefore it is essential to have a good understanding of the flow and sediment dynamics there. The goal of this thesis is twofold. One objective is to use an existing model to gain a more thorough understanding of the flow dynamics in an estuary. The second objective is to extend the model such that it can also compute the suspended sediment concentration in a cross-section.

The equations governing the flow dynamics are the shallow water equations. The advection-diffusion equation governs the sediment dynamics. To compute the flow and suspended sediment concentration in a cross-section, conditions are assumed to be uniform in the along-channel direction.

To solve the equations a coordinate transformation is applied first. After the transformation, the cross-section of the channel is represented in the computational domain by a rectangle. In the vertical direction, an eigenfunction expansion is used with eigenfunctions derived from a special case of the Sturm-Liouville eigenvalue problem. In the horizontal direction, derivatives are approximated with a central finite difference scheme. In the frequency domain, variables are expressed as the sum of tidal components. The Galerkin method is applied in both the vertical direction and the frequency domain to optimise the weight functions for every location along the transect. The system obtained with the Galerkin method is solved using Newton-Raphson iterations and an LU-decomposition. To find the distribution of the erosion coefficient corresponding to a morphodynamic equilibrium, a time integration method is used.

The effect of several parameters on the advective contribution to the cross-channel flow is systematically investigated. The results show that the steepness of the bottom slope affects the magnitude of the advective contribution to the residual lateral flow. For a steep bottom slope the contribution is large and for a gradual bottom slope the contribution is small. The curvature of the channel strongly affects the total cross-channel flow, depending on the magnitude of the radius of curvature, but hardly affects the flow caused by advection. The lateral density gradient can largely affect the cross-channel flow. Especially, the amplitude of the M_2 tidal component of the density gradient affects the advective contribution to the flow. Both the magnitude and characteristics of the advective contribution change when the amplitude of the M_2 tidal component of the density gradient is varied. The phase of the M_2 tidal component of the density gradient hardly affects the cross-channel flow and advective contribution of the flow.

Measurement data of a cross-section of the Ems is compared with a simulation of this situation. The magnitude of the lateral flow is similar for the measurements and model results but there is a difference in the direction of the flow in the upper part of the water column. This deviation could be caused by the description of the free surface. In the measurements there is a time-varying thickness of the water column whereas the rigid lid assumption is applied in the model. However, other differences between the simulation and the actual situation could have contributed to a deviation between the measurements and model results as well.

The results for the sediment module show that the model works as expected for a prescribed erosion coefficient and for computing the erosion coefficient in morphodynamic equilibrium for situations with only diffusive transport. For simple situations the analytical solution is approximated and for more complicated situations the results agree with the physical intuition. The main recommendation for further research is to investigate how the model can be extended such that it is also possible to compute the erosion coefficient in morphodynamic equilibrium for situations with both advective and diffusive sediment transport.

Preface

For a long time, I have been fascinated by the ways mathematics can be used to model real-world phenomena. This has been my main motivation to do a Masters in Applied Mathematics and to choose the specialisation Computational Science and Engineering. More specifically, the modelling of water motion and various constituents in coastal areas have already had my attention before starting this thesis. Both my Bachelor thesis and the internship I did during my Masters had a topic related to this. However, this project was entirely different than what I did before, which showed me once again how diverse this topic is. I really enjoyed learning more about the development of models for estuaries and I have worked on this thesis with great pleasure.

I would not have been able to deliver this thesis without help the help of my supervisors. I am very grateful Henk Schuttelaars and Tjerk Zitman were my two supervisors during this project. Both were always willing to help me out with a problem and lead me in a new direction when I was stuck. They taught me a lot about this specific topic and about conducting research in general and their critical view on my work has definitely led to improvements. Furthermore, I had a good laugh during our weekly meetings, which is maybe not essential but I definitely appreciated this a lot.

I would also like to thank Johan Dubbeldam and Martin van Gijzen for being part of my thesis committee and for taking the time to read my thesis.

Last, I would like to thank my family and friends. They provided some necessary breaks which definitely helped me to stay motivated during the past months. In particular, I would like to thank my housemates, due to Corona we spent a lot more time together than expected and they were great company for working on your thesis during a pandemic.

E.J. Burgers
Delft, November 2020

Contents

1 Introduction

This introduction is divided into four sections. In the first section some background information is given concerning estuaries and the water motion and sediment dynamics in these systems. This is followed by an overview of relevant previous research in Section 1.2. Next, the goal and research questions of this thesis are presented in Section 1.3. The last section outlines the structure of this thesis.

1.1. Background

1.1.1. Estuaries

An estuary is a body of water with one or more rivers flowing into it and an open connection with a sea or ocean [29]. Examples of estuaries in the Netherlands are the Western Scheldt (the mouth of the Scheldt river) and the Ems-Dollard (the mouth of the Ems river). Due to the open connection with the sea, the flow in an estuary is influenced by both tide and a river discharge. Because an estuary is a transition region between a river with fresh water and an ocean with salt water, the concentration of salt in the water strongly depends on location and time. Further from the ocean there is generally less salt in the water than closer to the ocean. Moreover, at the same location the concentration salt will typically vary during a tidal cycle. Figure 1.1 shows a schematic illustration of an estuary.

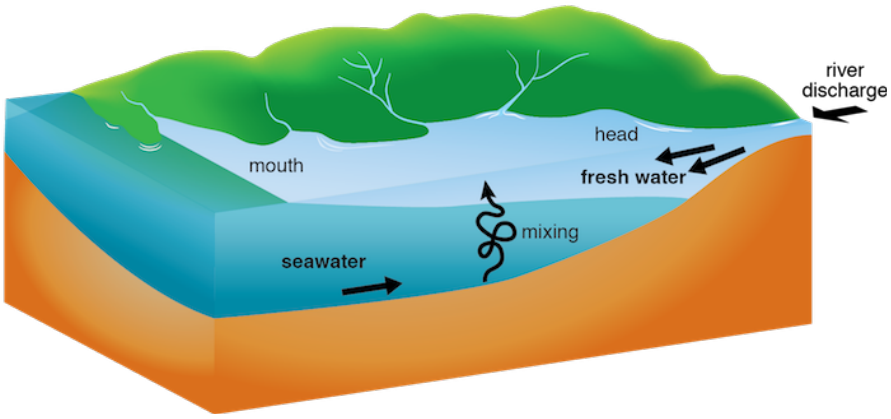

Figure 1.1: A schematic visualisation of an estuary. In this figure, the ocean is located on the left and the river on the right. The water originated from the ocean and the river mix in the estuary. Reprinted from [21].

Estuaries have always been important to mankind for various reasons. Many ports are located in estuaries and a large portion of the worlds fishery takes place in estuaries. Moreover, they are used for trade, transportation, recreation and when moving in the landward direction, estuaries can be a source of fresh water for irrigation and drinking water. Furthermore, estuaries are ecosystems with a great diversity of life [14]. These benefits of estuaries make it valuable to thoroughly understand the dynamics of flow, salinity, sediment and other constituents in estuaries. This thesis will focus on the water motion and sediment dynamics in estuaries.

1.1.2. Water motion

Estuaries are complex systems and the water motion in an estuary is affected by a large number of processes. Due to the river inflow and the open connection with sea, the flow dynamics is affected by the river discharge and the tidal prism (tidal volume of water entering and leaving the estuary during a tidal cycle). The mixing of fresh and salt water also leads to a salinity distribution which affects the density gradient in an estuary. The density gradient is also a forcing of the flow. Moreover, meteorological effects such as the wind can affect the flow in estuaries. The rotation of the earth contributes to the forcings of the flow due to the Coriolis effect. The topography affects the flow as well depending on properties such as the curvature of the estuary, bathymetry, water depth and more [7]. Identifying and investigating each of the contributions helps to understand the dynamics in estuaries more thoroughly and to make more accurate models for the flow in estuaries.

The observed motion of water results from a complex interaction of numerous three-dimensional mechanisms. This implies a three dimensional model is necessary to fully describe the water motion. However, these three dimensional models are difficult to analyse. To gain more fundamental knowledge, one can assume as a first step that the flow is homogeneous in one direction, resulting in a two dimensional model. In this thesis it is assumed that the estuary is homogeneous in the longitudinal direction, such that the focus is on the dynamics in a cross-section.

1.1.3. Sediment

Sediment is transported by the water, originating from both the river and the ocean. As a result of erosion, sediment particles can be suspended in the water, there they are transported along with the flow. Finally, due to gravity the sediment particles settle on the bed again. After deposition of sediment particles, this cycle can start over again. This means the distribution of sediment is mainly determined by the flow, the properties of the sediment grains and the availability of sediment at the bottom.

In many estuaries, there are locally large concentrations of sediment present. These elevated sediment concentrations are caused by a combination of physical and chemical processes [20]. The high amounts of sediment can cause siltation which is a problem for harbours and navigation channels [7]. Sediment can also cause ecological problems because sediment particles are often carriers of substances which can be polluting [7]. To prevent siltation and ecological problems, it is essential to have models that can predict where these areas with high sediment concentrations will be located.

1.2. Literature

To simulate the flow and sediment dynamics in estuaries, one can resort by complex numerical models such as ROMS [10], Delft3D [19] or TRIWAQ [26]. These are convenient for simulating realistic situations but they are less suitable for identifying the contribution of specific processes due to their complexity. Furthermore, these models are not developed to focus on cross-sections. Therefore, idealised models are developed, which are often analytical or use a combination of analytical and numerical techniques. These are especially suitable for investigating individual forcing mechanisms in idealised geometries.

Wong [32] was one of the first to develop an analytical model to study individual contributions to the flow in a cross-sectional model. In this study Wong found that both density gradients and local wind forcing can generate lateral variability in along-channel flows. Friedrichs et al. [8] developed an analytical model, that included the influence of density gradients, river discharge, sea-level variations and wind on the along-channel flow. Kasai et al. [15] focussed on the effect of the earths rotation on the along-channel flow. They concluded that Coriolis deflection can be an important factor in determining the flow pattern. The work of Kasai et al. is further extended by Valle-Levinson et al. [27] to include, among others, arbitrary bathymetries.

Using perturbation methods, Huijts et al. [11] extended these models to include sediment dynamics. They developed a model to investigate the effect of cross-channel density gradients and Coriolis forcing on both flow and sediment distribution. They concluded that the Ekman number determines which of these two processes is dominant. In Huijts at al. [12] the model is extended and used to examine the contribution of horizontal density gradients, tidal rectification processes, river discharge, wind, channel curvature and Coriolis deflection on both along-channel and cross-channel residual flows. Each of these contributions could be quantified and density-gradients were again identified as the most important contribution. They also concluded that the tidal rectification processes are crucial to the transverse

structure of the flows, because they lead to asymmetric distributions for relatively large tidal velocities or relatively steep and narrow channels. By Schramkowski et al. [22] the model in [11] was extended to investigate the effect of a partial slip bottom boundary condition on the cross-channel flow and sediment distribution. They found that there is only one maximum in the sediment distribution for a no-slip condition, whereas there are two maxima when a partial-slip condition is used. By Huijts et al. [13] the model in [11] was extended to include tidal variations in the density gradient, resulting in double circulations in the cross-channel flow profile.

In the analytical models discussed so far, the contribution of advection is assumed negligible. However, Lerczak and Geyer [18] and Cheng and Valle-Levinson [4] investigated the contribution of cross-channel advection with numerical models and concluded that advection can play an important role in the lateral circulation in weakly stratified estuaries [18] and in estuaries with a varying lateral bottom slope [4].

This motivated Yang et al. [33] to extend the model of Huijts et al. [11] to include advective transports in a perturbative approach, as well as more tidal components. With this extended model they explored the effect of the joint action of the M_2 and M_4 tidal flow, residual flow and spatial settling lag on the lateral entrapment of sediment. They found that the incorporation of M_4 tidal flow and spatial settling lag leads to an extra region of sediment trapping besides the region of sediment trapping caused by advective transport.

Zitman and Schuttelaars [34] developed a cross-sectional model for the water motion in which the advective contributions are taken into account at leading order. This model allowed for a decomposition of the various contributions of the water motion such as discharge, Coriolis forcing and curvature. Zitman and Schuttelaars concluded that advective and diffusive contributions have a noticeable effect on both the along-channel and cross-channel flow. They found that the relative importance of the along-channel advective forcing and cross-channel diffusion depends on the local characteristics of the lateral bottom profile. The model by Zitman and Schuttelaars [34] only considered the water motion. In this thesis this model is extended to include the sediment dynamics in a cross-section.

1.3. Research goals

As mentioned in the literature overview in the previous section, this project is based on the model developed by Zitman and Schuttelaars [34]. The goal of this project is twofold. The first objective is to use the existing model to gain a more thorough understanding of the flow dynamics in an estuary. In previous research often the contribution of advection is neglected, even though it can be an important influence on the lateral flow. To gain more understanding of the flow caused by advective contributions, simulations are performed with special attention for the effect of parameters on advective contributions. The second objective is to extend the model such that it can also compute the suspended sediment concentration in a cross-section. Because it is also required that the contributions of individual mechanisms can be quantified, this will contribute to gaining a better understanding of sediment dynamics in estuaries.

Six research questions are formulated to achieve these two goals. The first four concern the investigation of the advective contribution to the flow. The last two research questions apply to the development of the model extension to incorporate the suspended sediment dynamics. These research questions read:

1. What is the effect of the bottom slope on the advective contribution to the cross-channel residual flow profile?

2. What is the effect of the channel curvature on the advective contribution to the cross-channel residual flow profile?

3. What is the effect of the lateral density gradient on the advective contribution to the cross-channel residual flow profile?

4. Can the model reproduce the cross-channel residual velocity profile in measurements of the Ems in [24]?

5. Can the model be extended to incorporate the computation of the suspended sediment concentration for a prescribed erosion coefficient?

6. Can the model be extended to include the computation of the erosion coefficient corresponding to a morphodynamic equilibrium?

1.4. Outline

Following this introduction, Chapter 2 describes the equations and boundary conditions used to model the water motion and sediment dynamics. This chapter first contains the equations for the flow and then the equations for the suspended sediment concentration. Next, Chapter 3 discusses how the governing equations are solved in the model. Subsequently, Chapter 4 presents the results for the model, this section is subdivided in results for the flow and results for the suspended sediment concentration. Last, Chapter 5 contains the conclusion of this thesis by answering the research questions presented in Section 1.3. Some recommendations for further research are also given in this chapter. Afterwards multiple appendices can be found, elaborating on several details in the report.

2

Model description

This chapter explains the mathematical background of the model. The model is based on the model presented in [34]. In [34] only flow is computed and sediment is not taken into account. In this project the model is extended with the option to compute a sediment distribution.

First, the geometry is explained in Section 2.1. Next, the equations describing the flow are discussed in Section 2.2. Last, in Section 2.3, the equations describing the sediment distribution are discussed.

2.1. Geometry

As mentioned in Section 1.3, the objective of this thesis is to investigate the flow and sediment concentration in the cross-section of an estuary. To focus on the dynamics in a cross-section, it is assumed the dynamics does not depend on the along-channel coordinate. In Figure 2.1 the geometry of such an estuary is visualised, this figure is reprinted from [34]. It consists of two side walls and a smoothly varying bottom. The bottom profile can have any shape in the lateral direction but cannot contain vertical jumps. The channel can be either straight or curved, polar coordinates are a natural coordinate system allowing for both channels. The cross-channel coordinate is denoted by r, the along-channel coordinate is denoted by θ and the vertical coordinate is denoted by z. The θ coordinate increases in the seaward direction and when looking seaward the r coordinate increases towards the right. The vertical coordinate increases in the upward direction, with $z = 0$ at the undisturbed water level and $z = -H$ at the bottom.

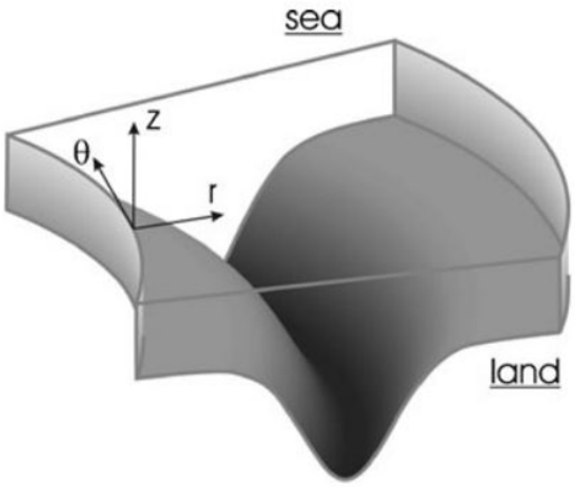

Figure 2.1: A sketch of the geometry of an estuary. Polar coordinates are used with θ pointing seaward and r pointing to the right when looking seaward. The bottom profile is arbitrary in the cross-channel direction and uniform in the along-channel direction. Reprinted from [34].

2.2. Dynamics of the flow

2.2.1. Governing equations

The flow is described by the shallow water equations. These are derived from the continuity equation and the Navier-Stokes equations in Appendix A. Several assumptions are made to derive the shallow water equations. First, the Boussinesq approximation is applied. This is the assumption that realistic temperature and salinity variations only lead to small variations in the density and the effect of these variations is only significant in the gravitational term [25]. Therefore, the density is assumed to be constant in all terms except the gravitational term.

Next, it is assumed the vertical scales are much smaller than the horizontal scales, this is called the shallow water assumption [30]. For example, the water depth must be much smaller than the width of the estuary.

Furthermore, the the rigid lid approximation is used. The rigid lid approximation uses that surface displacements are small compared to the water depth. As a consequence, variations in the surface level are ignored but the pressure gradient due to these variations is not neglected [9].

The goal of this project is to compute the flow and sediment concentration in a cross-section, which is assumed to be uniform in the along-channel direction. Because along-channel uniformity is assumed, the derivatives of the flow velocities with respect to θ are equal to zero in the equations. After applying along-channel uniformity on the result of Appendix A, transforming this to polar coordinates and assuming the atmospheric pressure to be constant, the governing equations read,

$$\frac{\partial u_r}{\partial t} + u_r\frac{\partial u_r}{\partial r} + u_z\frac{\partial u_r}{\partial z} - \gamma u_\theta - \frac{u_\theta^2}{r} = -\frac{g}{\rho_0}\int_z^0 \frac{\partial \rho}{\partial r}\,\mathrm{d}z' - g\frac{\partial \zeta}{\partial r} + A_v\frac{\partial}{\partial z}\left(\phi\frac{\partial u_r}{\partial z}\right) + A_h\frac{1}{r}\frac{\partial}{\partial r}\left(r\frac{\partial u_r}{\partial r}\right), \quad (2.1)$$

$$\frac{\partial u_\theta}{\partial t} + u_r\frac{\partial u_\theta}{\partial r} + u_z\frac{\partial u_\theta}{\partial z} + \gamma u_r + \frac{u_\theta u_r}{r} = -\frac{g}{\rho_0}\int_z^0 \frac{1}{r}\frac{\partial \rho}{\partial \theta}\,\mathrm{d}z' - g\frac{1}{r}\frac{\partial \zeta}{\partial \theta} + A_v\frac{\partial}{\partial z}\left(\phi\frac{\partial u_\theta}{\partial z}\right) + A_h\frac{1}{r}\frac{\partial}{\partial r}\left(r\frac{\partial u_\theta}{\partial r}\right), \quad (2.2)$$

$$\frac{u_r}{r} + \frac{\partial u_r}{\partial r} + \frac{\partial u_z}{\partial z} = 0. \quad (2.3)$$

The flow velocities are denoted by u_r, u_θ and u_z for the cross-channel, along-channel and vertical velocity, respectively. In the above expressions, γ is the Coriolis parameter, g is the gravitational acceleration, ρ is the fluid density, ρ_0 is the reference density and ζ is the surface level elevation. The horizontal eddy viscosity is denoted by A_h. The vertical eddy viscosity is written as $A_v\phi$ with ϕ a shape function and A_v a parameter indicating the strength of the vertical eddy viscosity. To obtain the parameters for the eddy viscosity, various turbulence models can be used [3]. Generally, more complicated turbulence models result in more sophisticated models but also make it harder to solve the system of equations. Here, A_h and A_v are taken time and space invariant. The normalised shape function is parameterising the profile of the vertical eddy viscosity. This profile is time invariant and does not depend on the horizontal coordinate. The vertical shape of ϕ is parabolic, this is a common assumption for tide dominated estuaries [17]. The density gradient of the water is determined by the salinity S, which is a diagnostic quantity in this model.

To obtain information about the tidal properties of the flow and sediment distribution, the model equations are solved in the frequency domain. Consequently, all time-dependent variables are described as a sum of tidal components. In this thesis M_0, M_2 and M_4 contributions are included.

2.2.2. Boundary conditions

Naturally, boundary conditions are required so solve the system of equations. At the two side walls and the bottom a no-slip condition is applied, this means the velocity directed parallel to the boundary is zero at these boundaries. Moreover, it is assumed the velocity normal to the boundary is zero since the water cannot flow through the boundaries. As a consequence, all velocity components must be zero at the side walls and the bottom. Since the rigid lid approximation is used, u_z is also zero at the surface.

A wind shear stress acting on the water surface determines the vertical gradient of the horizontal flow velocity at that surface, according to

$$A_v\frac{\partial u_r}{\partial z} = \frac{\tau_{w,r}}{\rho_0}, \qquad A_v\frac{\partial u_\theta}{\partial z} = \frac{\tau_{w,\theta}}{\rho_0}. \quad (2.4)$$

In all cases studied in this thesis, the effect of wind is not included, requiring the surface velocity gradients to be zero as a boundary condition.

By integration of the continuity equation (2.3) over depth and using the boundary conditions, one finds that,

$$\int_{-H}^{0} u_r \, \mathrm{d}z = 0, \tag{2.5}$$

at every point along the transect. In other words, the cross-channel water flux must be zero everywhere. The derivation of this condition can be found in Appendix B. This condition is used to compute the cross-channel surface slope.

Finally, there is a condition regarding the discharge,

$$\int_{0}^{W} \int_{-H}^{0} u_\theta \, \mathrm{d}z \, \mathrm{d}r = q. \tag{2.6}$$

Here q is the total discharge, which is the sum of the river discharge, assumed constant in time, and the tidal discharge, which is periodic in time and may consist of different tidal components.

In the model, either the discharge or the longitudinal surface slope must be prescribed. For a prescribed discharge, a suitable surface slope is computed such that the flow matches the assigned discharge following condition (2.6). On the other hand, when the surface slope is prescribed, the corresponding discharge is computed using condition (2.6). The cases studied in this thesis all have a prescribed discharge.

2.2.3. Decomposition of the flow field

To analyse and understand the dynamics of the flow field, it is useful to decompose the velocities in contributions from individual mechanisms. To do this, the horizontal velocity components are written as the sum of velocities caused by individual forcings,

$$u_r = \sum_i u_{r,i}, \qquad u_\theta = \sum_i u_{\theta,i}, \tag{2.7}$$

with i indicating a specific forcing and $u_{r,i}$ and $u_{\theta,i}$ the velocities resulting from this forcing.

The mechanisms that are considered in this report are Coriolis deflection, advection, curvature, density gradient, horizontal diffusion and discharge.

Each mechanism, except the discharge, results in two forcings, one for the cross-channel direction and one for the along-channel direction. In Table 2.1 the forcings and discharge corresponding to the mechanisms are tabulated.

To find the contribution to the flow associated to a specific mechanism, first the flow field has to be computed with the fully non-linear model. Next, the forcings defined in Table 2.1 are computed using the results obtained with the model. Finally, the contributions $u_{r,i}$ and $u_{\theta,i}$ are computed by solving the following equations,

$$\frac{\partial u_{r,i}}{\partial t} + g\left[\frac{\partial \zeta}{\partial r}\right]_i - A_v \frac{\partial}{\partial z}\left(\phi \frac{\partial u_{r,i}}{\partial z}\right) = F_i, \tag{2.8}$$

$$\frac{\partial u_{\theta,i}}{\partial t} + g\left[\frac{1}{r}\frac{\partial \zeta}{\partial \theta}\right]_i - A_v \frac{\partial}{\partial z}\left(\phi \frac{\partial u_{\theta,i}}{\partial z}\right) = G_i. \tag{2.9}$$

$$\int_{0}^{W} \int_{-H}^{0} u_{\theta,i} \, \mathrm{d}z \, \mathrm{d}r = Q_i, \tag{2.10}$$

$$\int_{-h}^{0} u_{r,i} \, \mathrm{d}z = 0. \tag{2.11}$$

For the velocity corresponding to each forcing mechanism the same boundary equations are used as in the model. This means at the bottom $u_{r,i}$ and $u_{\theta,i}$ must be zero and at the surface the derivative of $u_{r,i}$ and $u_{\theta,i}$ with respect to z must be zero as well.

Similar to the velocities, the surface slopes are also written as the sum of surface slopes caused by individual forcings. The along-channel surface slope caused by an individual forcing is computed

such that equation (2.10) holds for the velocity and discharge corresponding to the same forcing. The cross-channel surface slope for an individual forcing is computed such that (2.11) holds for the velocity caused by that forcing.

Table 2.1: The mechanisms that are distinguished to affect the flow field and their corresponding cross-channel and along-channel forcings and discharge.

Mechanism	Cross-channel forcing (F_i)	Along-channel forcing (G_i)	Discharge (Q_i)
Coriolis deflection	$-\gamma u_\theta$	γu_r	0
Advection	$u_r \frac{\partial u_r}{\partial r} + u_z \frac{\partial u_r}{\partial z}$	$u_r \frac{\partial u_\theta}{\partial r} + u_z \frac{\partial u_\theta}{\partial z}$	0
Curvature	$-\frac{u_\theta^2}{r}$	$\frac{u_\theta u_r}{r}$	0
Density gradient	$\frac{g}{\rho_0}\int_z^0 \frac{\partial \rho}{\partial r}\,\mathrm{d}z'$	$\frac{g}{\rho_0}\int_z^0 \frac{1}{r}\frac{\partial \rho}{\partial \theta}\,\mathrm{d}z'$	0
Horizontal diffusion	$-A_h \frac{1}{r}\frac{\partial}{\partial r}\left(r\frac{\partial u_r}{\partial r}\right)$	$-A_h \frac{1}{r}\frac{\partial}{\partial r}\left(r\frac{\partial u_\theta}{\partial r}\right)$	0
Discharge	0	0	q

2.3. Dynamics of suspended sediment

2.3.1. Governing equation

The suspended sediment dynamics is governed by an advection-diffusion equation. Along-channel uniformity is assumed and no sinks or sources in the water column are included, similar to the sediment mass balance equation in [11]. The governing equation for sediment in polar coordinates reads,

$$\frac{\partial c}{\partial t} + u_r \frac{\partial c}{\partial r} + (u_z - w_s)\frac{\partial c}{\partial z} = D_v \frac{\partial}{\partial z}\left(\phi \frac{\partial c}{\partial z}\right) + D_h \frac{1}{r}\frac{\partial}{\partial r}\left(r\frac{\partial c}{\partial r}\right). \tag{2.12}$$

In the equation above, c is the suspended sediment concentration, w_s is the settling velocity and D_v and D_h are the vertical and horizontal eddy diffusivity coefficients, which are chosen to be equal to their eddy viscosity counterparts.

2.3.2. Boundary conditions

The boundary conditions for sediment are different, compared to the conditions for the flow. The boundary conditions for this model are similar to the boundary conditions used in [11]. Since sediment cannot move through the side walls, the flux must be zero at those boundaries. As a consequence, the horizontal advective and diffusive transports must balance at the sides:

$$u_r c - D_h \frac{\partial c}{\partial r} = 0. \tag{2.13}$$

Because u_r is zero at the side walls, this simplifies to

$$\frac{\partial c}{\partial r} = 0. \tag{2.14}$$

No flux of sediment is allowed through the free surface, resulting in,

$$-w_s c - D_v \phi \frac{\partial c}{\partial z} = 0, \tag{2.15}$$

showing that the settling flux and diffusive flux must balance.

At the bottom, the diffusive flux normal to the bed is related to the erosion of sediment from the bed:

$$E = -D_h \frac{\partial c}{\partial r} n_r - D_v \phi \frac{\partial c}{\partial z} n_z = \frac{w_s \rho_s}{\rho_0 g' D_s} |\tau_b| a(r). \tag{2.16}$$

Here, ρ_s is the sediment density, ρ_0 is the water density, g' the reduced gravity which is defined as $g' = g(\rho_s - \rho_0)/\rho_0$, D_s is the characteristic grain diameter and $a(r)$ is the erosion coefficient. The outward pointing unit vector $\mathbf{n} = (n_r, n_z)$ reads,

$$n_r = \frac{dH}{dr}\left(1 + \left(\frac{dH}{dr}\right)^2\right)^{-1/2}, \; n_z = \left(1 + \left(\frac{dH}{dr}\right)^2\right)^{-1/2}, \tag{2.17}$$

and the bed shear stress is given by

$$|\tau_b| = \rho_0 A_v \phi \left|\frac{\partial u}{\partial z}\right| = \rho_0 A_v \phi \sqrt{\left(\frac{\partial u_r}{\partial z}\right)^2 + \left(\frac{\partial u_\theta}{\partial z}\right)^2}, \tag{2.18}$$

evaluated at $z = -H$.

When the bottom slope is small, $\frac{dh}{dr} \ll 1$, $n_r \approx 0$ and $n_z \approx 1$, simplifying the bottom boundary condition to,

$$-D_v \phi \frac{\partial c}{\partial z} = \frac{w_s \rho_s}{g' D_s \rho_0} |\tau_b| a(r). \tag{2.19}$$

One can prescribe an arbitrary function as the erosion coefficient and then use the model to compute the corresponding suspended sediment concentration in the cross-section. However, it is also possible to find the erosion coefficient corresponding to an equilibrium, this is discussed in the next section.

2.3.3. Morphodynamic equilibrium

Typically, the sediment availability changes on a time scale much larger than the tidal timescale but much smaller than the time scale over which river discharge or tidal amplitude change. Therefore, it can be assumed there is no mean evolution of the bed on the short timescale, this is called a morphodynamic equilibrium. For this equilibrium it is necessary that the averaged deposition and erosion of sediment balance. This can be achieved by prescribing an erosion coefficient $a(r)$ such that the divergence of the transport vanishes.

The erosion of sediment normal to the bed is given in equation (2.16). The deposition of sediment normal to the bed is defined at $z = -H$ by

$$D = w_s c \; n_z. \tag{2.20}$$

To have a morphodynamic equilibrium, the tidally averaged erosion and deposition should be equal, so

$$\langle D \rangle - \langle E \rangle = 0. \tag{2.21}$$

The angle brackets denote tidal averages.

This morphodynamic equilibrium condition can also be expressed as a balance between advective and diffusive transport of sediment. This condition can be obtained by the same approach as taken in [11]. First integrate equation (2.12) over depth, then apply Leibniz rule. Next, the boundary conditions from Section 2.3.2 and the relation in equation (2.21) are used. The step by step derivation can be found in Appendix C. The final result is

$$\int_{-H}^{0} \langle u_r c \rangle - D_h \frac{\partial \langle c \rangle}{\partial r} \, \mathrm{d}z = 0, \tag{2.22}$$

for every r. This is equivalent to stating that the total tidally averaged lateral sediment transport must be zero because this is defined as,

$$T_{tot} = \int_{-H}^{0} \langle u_r c \rangle - D_h \frac{\partial \langle c \rangle}{\partial r} \, \mathrm{d}z. \tag{2.23}$$

The total transport can be subdivided into the M_0 advective transport, the M_2 advective transport, possibly transports for higher tidal components and the diffusive transport. The tidally averaged lateral transports for M_0, M_2 and diffusion are defined as,

$$T_{M_0} = \int_{-H}^{0} u_{r,M_0} c_{M_0} \, \mathrm{d}z, \tag{2.24}$$

$$T_{M_2} = \int_{-H}^{0} \langle u_{r,M_2} c_{M_2} \rangle \, \mathrm{d}z, \tag{2.25}$$

$$T_{dif} = \int_{-H}^{0} -D_h \frac{\partial \langle c \rangle}{\partial r} \, \mathrm{d}z. \tag{2.26}$$

Summed these transports approximate again T_{tot} up to the M_2 tidal component.

In a morphodynamic equilibrium, the erosion coefficient is constant because the tidally averaged lateral transport is zero. If the divergence of the lateral sediment transport is positive at a location, the erosion coefficient decreases there, whereas a negative divergence of the lateral sediment transport results in a higher erosion coefficient at that point. This relationship can be expressed as

$$\frac{da}{dt} = -\nabla \cdot T_{tot}. \tag{2.27}$$

In Section 3.7 is explained how the time evolution of the erosion coefficient is used to find the erosion coefficient corresponding to a morphodynamic equilibrium. Note that $\frac{da}{dt}$ does not represent the actual derivative of a with respect to the physical time t since a is not a time-dependent variable. In this expression t indicates a kind of pseudo time which allows to use a time integration method to find $a(r)$ in morphodynamic equilibrium.

The morphodynamic equilibrium condition results in a specific spatial distribution of the erosion coefficient, which is determined up to a multiplication constant. This additional constant follows from prescribing the total amount of sediment, available for erosion, in the cross-section:

$$\frac{1}{B} \int_0^B a(r) \, \mathrm{d}r = a_* \, , \tag{2.28}$$

with a_* the reference value.

3

Solution Methods

In the previous chapter the model equations were presented. This chapter explains how these equations are solved in the model. To solve the equations, a further developed version of the method in [34] is used.

In the model the equations for the flow and concentration are solved consecutively, assuming that spatial variations in the suspended sediment concentration have a negligible effect on the flow pattern. First, the flow is computed, afterwards the obtained flow velocities are used to find a solution for the concentration equation. If the discharge is prescribed, the computation of the flow consists of two nested loops. In the inner loop, the shallow water equations are solved simultaneously based on an estimate for the along-channel surface slope. In the outer loop, the estimated along-channel surface slope is adjusted to obtain the prescribed discharge.

To find the concentration for a morphodynamic equilibrium, an iterative process is also required. In this iteration process the value of the erosion coefficient is varied to obtain the one erosion coefficient corresponding to a morphodynamic equilibrium. The iterative processes are schematically visualised in Figure 3.1.

The first sections of this chapter cover solving the model equations. In the last two sections the iterative procedures to obtain the correct discharge and erosion coefficient are discussed.

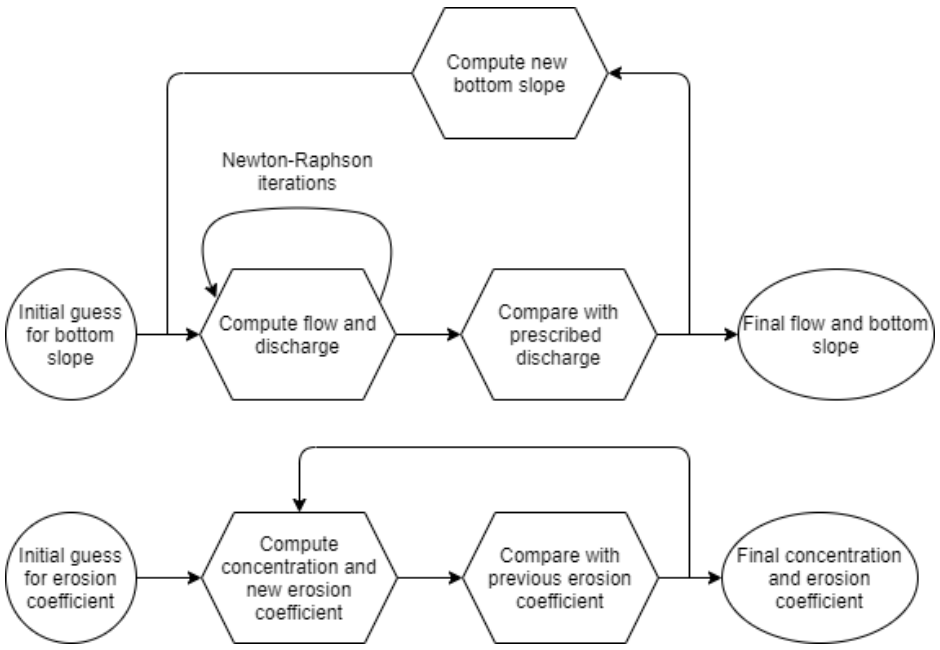

Figure 3.1: Schematic views of the iterative processes to obtain the flow (upper flow diagram) and concentration (lower flow diagram).

3.1. Computational grid

The number of grid points affects the accuracy of the results but also the computational time and storage space that are required. In the radial direction L grid points are used. In this report the default value of L is 301 but when for example computing the flow for a steep bottom profile, it is necessary to increase L. In the vertical direction, an eigenfunction expansion is used. The eigenfunctions are obtained numerically on a grid with 10001 points. In both the radial and vertical direction the grid points are uniformly distributed, so the distance between two neighbouring grid points is constant over the whole domain.

To solve the model equations (2.1), (2.2), (2.3), (2.5) and (2.12) several steps are taken. First, the cylindrical coordinate system (r, θ, z) used in the physical domain is mapped onto a system (ξ, θ, σ), in which the coordinates ξ and σ are defined such that the concerned cross-section of the channel is represented by a rectangle in the computational domain. The details of this transformation can be found in Appendix D, the transformed model equations are also given in this appendix.

3.2. Vertical series expansion

In the vertical direction, an eigenfunction expansion is used to express the variables u_r, u_θ and c. This means a variable is expressed as the sum of eigenfunctions multiplied by weight functions. For u_r, u_θ and c, this results in,

$$u_r(\xi, \sigma, t) = \sum_{m=1}^{M+N} U_m(\xi, t) f_m(\xi, \sigma), \tag{3.1}$$

$$u_\theta(\xi, \sigma, t) = \sum_{m=1}^{M+N} V_m(\xi, t) f_m(\xi, \sigma), \tag{3.2}$$

$$c(\xi, \sigma, t) = \sum_{m=1}^{M+N} C_m(\xi, t) d_m(\xi, \sigma), \tag{3.3}$$

with f_m the eigenfunctions for the flow, d_m the eigenfunctions for the concentration and U_m, V_m and C_m the weight functions. In Section 3.4 is explained how the weight functions are optimised using the Galerkin method. In this thesis, the eigenfunction expansion is based on the method used in [5]. In this method a special case of the Sturm-Liouville eigenvalue problem is used to derive the eigenfunctions,

$$\frac{\partial}{\partial \sigma}\left(\phi(\xi, \sigma)\frac{\partial f_m}{\partial \sigma}\right) + \lambda_m f_m w(\xi, \sigma) = 0, \tag{3.4}$$

with

$$f_m(\xi, 0) = \frac{\partial f_m}{\partial \sigma}(\xi, 1) = 0. \tag{3.5}$$

The λ_m are eigenvalues and $w(\xi, \sigma)$ is a weight function. The choice for the weight function affects the computational effort necessary to obtain the eigenvalues. A specific $w(\xi, \sigma)$ that is suitable for this model was advised by T.J. Zitman. The eigenfunctions of the Sturm-Liouville eigenvalue problem are orthogonal [2]. Because this case of the Sturm-Liouville eigenvalue problem is used, the vertical mixing term in the model equations is simplified a lot.

A number of M eigenfunction is determined. For M infinitely large, the exact solution to the equations would be obtained. To make it possible to compute the flow, a finite value for M is chosen. At both the bottom and surface boundary the flow cannot be represented when using these eigenfunctions. At the surface the boundary condition for the eigenfunctions is homogeneous, as a result these eigenfunctions cannot deal with an non-zero wind shear stress. At the bottom the eigenfunctions are zero and consequently cannot represent the vertical mixing term unless there is a zero pressure gradient, which is unlikely. This effect is called the Gibbs phenomenon. To deal with these inconsistencies, two differently defined eigenfunctions are introduced. The number N indicates the number of differently defined eigenfunctions added to the series expansion. In this model N equals two.

For d_m, the eigenfunctions for the concentration, a similar method is applied to obtain the eigenfunctions. More details about the derivation of the eigenfunctions can be found in Appendix E, the model equations including the expansions are also given there.

It is computationally expensive to compute the eigenfunctions. However, for the same bottom profile and eddy viscosity distribution ϕ, the eigenfunctions are equivalent regardless the other parameters. Therefore, the eigenfunctions only have to be computed for the first simulation and can be reused afterwards for multiple simulations with different parameters.

3.3. Frequency series expansion

The model equations are solved in the frequency domain. Consequently, all time-dependent variables are expressed as a sum of tidal components. The weight functions U_m, V_m and C_m are depending on both time and lateral location and are therefore expressed as a sum of K tidal components,

$$U_m(\xi,t) = U_m^{(o)}(\xi) + \sum_{k=1}^{K} U_{m,k}^{(c)}(\xi)\cos(k\omega t) + U_{m,k}^{(s)}(\xi)\sin(k\omega t), \tag{3.6}$$

$$V_m(\xi,t) = V_m^{(o)}(\xi) + \sum_{k=1}^{K} V_{m,k}^{(c)}(\xi)\cos(k\omega t) + V_{m,k}^{(s)}(\xi)\sin(k\omega t), \tag{3.7}$$

$$C_m(\xi,t) = C_m^{(o)}(\xi) + \sum_{k=1}^{K} C_{m,k}^{(c)}(\xi)\cos(k\omega t) + C_{m,k}^{(s)}(\xi)\sin(k\omega t). \tag{3.8}$$

with K the number of tidal components. If $K = 1$ only a semi diurnal M_2-component would be included, when $K = 2$ the M_4-component is also included and so on. In this report $K = 2$. For K infinitely large the exact solution is obtained. To limit the number of weight functions that have to be solved, K is chosen equal to two. Therefore, the time-dependent variables in this report are a sum of M_0, M_2 and M_4 contributions.

Similar to the weight functions for the flow and concentration, all other time-dependent variables are also expanded as sum of tidal components:

$$\frac{\partial\zeta}{\partial r} = E^{(o)} + \sum_{k=1}^{K} E_k^{(c)}\cos(k\omega t) + E_k^{(s)}\sin(k\omega t), \qquad \frac{1}{r}\frac{\partial\zeta}{\partial\theta} = H^{(o)} + \sum_{k=1}^{K} H_k^{(c)}\cos(k\omega t) + H_k^{(s)}\sin(k\omega t),$$

$$\frac{\partial\rho}{\partial r} = P^{(o)} + \sum_{k=1}^{K} P_k^{(c)}\cos(k\omega t) + P_k^{(s)}\sin(k\omega t), \qquad \frac{1}{r}\frac{\partial\rho}{\partial\theta} = Y^{(o)} + \sum_{k=1}^{K} Y_k^{(c)}\cos(k\omega t) + Y_k^{(s)}\sin(k\omega t),$$

$$A_v = A^{(o)} + \sum_{k=1}^{K} A_k^{(c)}\cos(k\omega t) + A_k^{(s)}\sin(k\omega t), \qquad D_v = D^{(o)} + \sum_{k=1}^{K} D_k^{(c)}\cos(k\omega t) + D_k^{(s)}\sin(k\omega t),$$

$$q = Q^{(o)} + \sum_{k=1}^{K} Q_k^{(c)}\cos(k\omega t) + Q_k^{(s)}\sin(k\omega t), \qquad \chi = X^{(o)} + \sum_{k=1}^{K} X_k^{(c)}\cos(k\omega t) + X_k^{(s)}\sin(k\omega t).$$

The variable χ was not introduced yet but is used for the bottom boundary condition of the equation governing the suspended sediment concentration. The variable is defined as the bed shear stress divided by the reference density,

$$\chi(r,t) = A_v\phi(-H)\sqrt{\left(\frac{\partial u_r}{\partial z}\right)^2 + \left(\frac{\partial u_\theta}{\partial z}\right)^2} = \frac{|\tau_b|}{\rho_0}. \tag{3.9}$$

The cross-channel surface slope $\frac{\partial\zeta}{\partial r}$ is computed simultaneously with the horizontal velocities. To compute the cross-channel surface slope, condition (2.5) is included in the model equations. The along-channel surface slope $\frac{1}{r}\frac{\partial\zeta}{\partial\theta}$ is computed in the outer loop of the model, this is further explained in Section 3.6

After substituting the series expansions in both the vertical and frequency domain, the unknown physical variables are expressed as,

$$u_r(\xi,\sigma,t) = \sum_{m=1}^{M+N}\left(U_m^{(o)}(\xi) + \sum_{k=1}^{K} U_{m,k}^{(c)}(\xi)\cos(k\omega t) + U_{m,k}^{(s)}(\xi)\sin(k\omega t)\right) f_m(\xi,\sigma), \tag{3.10}$$

$$u_\theta(\xi,\sigma,t) = \sum_{m=1}^{M+N}\left(V_m^{(o)}(\xi) + \sum_{k=1}^{K} V_{m,k}^{(c)}(\xi)\cos(k\omega t) + V_{m,k}^{(s)}(\xi)\sin(k\omega t)\right) f_m(\xi,\sigma). \tag{3.11}$$

$$\frac{\partial\zeta}{\partial r} = E^{(o)} + \sum_{k=1}^{K} E_k^{(c)}\cos(k\omega t) + E_k^{(s)}\sin(k\omega t), \tag{3.12}$$

$$c(\xi,\sigma,t) = \sum_{m=1}^{M+N}\left(C_m^{(o)}(\xi) + \sum_{k=1}^{K} C_{m,k}^{(c)}(\xi)\cos(k\omega t) + C_{m,k}^{(s)}(\xi)\sin(k\omega t)\right) d_m(\xi,\sigma). \tag{3.13}$$

Consequently, there is a large number of unknown weight functions that have to be computed to solve u_r, u_θ, $\frac{\partial\zeta}{\partial r}$ and c. The weight functions are $U_m^{(o)}$, $U_{m,k}^{(c)}$, $U_{m,k}^{(s)}$, $V_m^{(o)}$, $V_{m,k}^{(c)}$, $V_{m,k}^{(s)}$, $E^{(o)}$, $E_k^{(c)}$, $E_k^{(s)}$, $C_m^{(o)}$, $C_{m,k}^{(c)}$ and $C_{m,k}^{(s)}$, for $m = 1 \ldots (M+N)$ and $k = 1 \ldots K$. The weight functions, but also the eigenfunctions, are discretized in the horizontal direction. The derivatives in the horizontal direction are expressed with a central finite difference scheme. As a consequence of this discretization, the value for the weight functions must be computed for every location ξ_i. This is done by using the Galerkin method, which is explained in the next section.

3.4. Galerkin method

The Galerkin method is used to find the value of the unknown weight functions at every location along the transect. By applying the Galerkin technique on the model equations, a system with the same number of equations as unknown variables is obtained, which is solved to find the unknown variables. The Galerkin method involves multiplying the model equations with a set of basis functions and integrating over the corresponding domain. The basis functions must be linearly independent. For a more extended explanation of the Galerkin method, see [28].

It was already mentioned that the eigenfunctions of the Sturm-Liouville eigenvalue problem are orthogonal. Since none of the eigenfunctions is constant zero, they are also linearly independent and can be used as basis functions for the Galerkin method. The functions 1, $\cos(k\omega t)$ and $\sin(k\omega t)$ are also linearly independent and can also be used as basis functions.

The momentum and concentration equations are first multiplied with the eigenfunctions f_p or d_p for $p = 1 \ldots M$ and then integrated over the vertical domain [0,1]. Next, all equations are multiplied with test functions 1, $\cos(k\omega t)$ and $\sin(k\omega t)$ and integrated over time from $-\pi/\omega$ to π/ω. This results, at every location along the transect, in a total of $(2K+1)\cdot(2\cdot(M+N)+1)$ equations for the flow and $(2K+1)\cdot(M+N)$ equations for the concentration. This is equal to the number of unknown weight functions. The equations can be found in Appendix F. For clarity the resulting equations are subdivided into equations for test function 1, $\cos(k\omega t)$ and $\sin(k\omega t)$.

3.5. Root finding method

After applying the Galerkin technique, a non-linear system of equations is obtained for the flow,

$$\mathbf{L}\mathbf{x} + \mathbf{m}(\mathbf{x}) = \mathbf{0}. \tag{3.14}$$

here **L** is a matrix for the linear part of the system of equations, **m** is a function for the non-linear part of the system. The vector **x** contains the values of the weight functions for every location ξ_i. To find the correct vector **x**, the Newton-Raphson method is used. For a more extensive description of this method, see [31].

The Newton-Raphson method is an iterative method in which consecutive estimates of the root are obtained from a first order Taylor approximation of the system at the previous estimate. For the first

order Taylor approximation, the Jacobi matrix has to be computed. The Jacobi matrix consists of the derivatives of each of the equations in system (3.14) to every unknown variable. The system that is solved in a Newton-Raphson iteration reads,

$$\mathbf{J_f}(\mathbf{x}_i)\Delta_i = -\mathbf{f_f}(\mathbf{x}_i). \tag{3.15}$$

Here $\mathbf{x}_i$ indicates the ith guess for the vector $\mathbf{x}$, $\mathbf{J_f}(\mathbf{x}_i)$ is the Jacobi matrix of system (3.14) for the vector $\mathbf{x}_i$, $\mathbf{f_f}(\mathbf{x}_i)$ is a vector containing the the non-linear equations evaluated for the vector $\mathbf{x_i}$. The ith correction vector denoted by Δ_i, is defined as, $\Delta_i = \mathbf{x}_{i+1} - \mathbf{x}_i$. The correction vector is used to compute the next vector $\mathbf{x}_{i+1}$ by $\mathbf{x}_{i+1} = \mathbf{x_i} + \Delta_i$. When the elements of the correction vector become smaller than a chosen accuracy, the iterations stop and the approximate solution is found.

In every iteration, the system in equation (3.15) is solved using an LU-decomposition. This means the Jacobi matrix is decomposed in a lower ($\mathbf{L}$) and upper ($\mathbf{U}$) triangular matrix, $\mathbf{J_f} = \mathbf{LU}$. By first solving $\mathbf{L}(\mathbf{U}\Delta) = -\mathbf{f}$ for $\mathbf{U}\Delta$ and then solving Δ from this, the solution for equation (3.15) is obtained.

Note that the Jacobi matrix is very sparse because for every location ξ_i, the model equations only contain variables for locations ξ_{i-1}, ξ_i and ξ_{i+1}. As a result, the Jacobi matrix is a block-tridiagonal matrix. More information about the structure of the Jacobi matrix $\mathbf{J_f}$ and the vector with unknown variables $\mathbf{x}$ can be found in Appendix G.

For the concentration, a linear system of equations is obtained after applying the Galerkin method. This is an important difference in comparison with the system of equations for the flow. Due to this linearity, the concentration equations are easier to solve. The system that needs to be solved reads,

$$\mathbf{J_c c} = \mathbf{f_c}, \tag{3.16}$$

with $\mathbf{J_c}$ the Jacobi matrix for the concentration equations. This matrix does not depend on the unknown weight functions for the concentration. The vector $\mathbf{c}$ is the vector of unknown variables which consists of $C_m^{(o)}$, $C_{m,k}^{(c)}$ and $C_{m,k}^{(s)}$ and $\mathbf{f_c}$ is the vector for the right hand side of the system of equations. The elements of $\mathbf{f_c}$ should be equal to zero except for the elements that are corresponding to the bottom boundary condition. Those elements are equal to the right hand side of the equations for the bottom boundary in Appendix F, equations (F.24), (F.27) and (F.30). This system is again solved using an LU-decomposition. Similar to the Jacobi matrix for the flow, this Jacobi matrix is also very sparse. The structure of this matrix $\mathbf{J_c}$ and this vector of unknowns $\mathbf{c}$ is also discussed in Appendix G.

3.6. Discharge

As mentioned at the start of this chapter, this section covers the methodology to find the along-channel surface slope corresponding to the prescribed discharge. Again Newton-Raphson iterations are used. This process starts with an initial guess for the surface slope. The model equations are solved with this guess and the flow and corresponding discharge are obtained. Next the deviation from the prescribed discharge is computed. As long as the deviation is too large, an adjustment for the surface slope is determined. The process is terminated when the deviation is within the tolerance bounds.

To find a suitable adjustment for the surface slope, the flow and discharge are not only computed for a guess for the surface slope H but also for a slightly different surface slope $H + \Delta H$. Now the derivative of the discharge Q with respect to the surface slope can be computed numerically. For the M_0 components this can be expressed as,

$$\frac{\partial Q^{(o)}}{\partial H^{(o)}} = \frac{Q^{(o)}\left(H^{(o)} + \Delta H\right) - Q^{(o)}\left(H^{(o)}\right)}{\Delta H}. \tag{3.17}$$

This is done similarly for the other tidal components. These derivatives can be used to construct a Jacobi Matrix $\mathbf{J}$. Now a vector $\mathbf{h}$ with adjustments for each of the tidal components of the surface slope can be computed as,

$$\mathbf{h} = \mathbf{J}\backslash\Delta\mathbf{q}, \tag{3.18}$$

with $\Delta\mathbf{q}$ the difference between the prescribed discharge and the discharge computed with the current guess for the surface slope. After the adjustment is added to the latest guess for the surface slope, a new flow and discharge can be computed. This process is repeated until the required accuracy is obtained.

3.7. Erosion coefficient in morphodynamic equilibrium

In a morphodynamic equilibrium, equation (2.22) should hold. During this project, several approaches were tried to find a suitable method to obtain an erosion coefficient $a(r)$ for which the morphodynamic equilibrium condition holds. Of them, using a time integrator was the only method that resulted in a correct output for $a(r)$. This method is described in this section, the other methods are briefly discussed in Appendix H.

The time integration method starts with an initial estimate for the erosion coefficient, a_1. The concentration c is computed as described in the previous sections with this erosion coefficient. Next, the time evolution of the erosion coefficient $\frac{da_1}{dt}$ is computed, which is used to find the next guess, a_2. With this new guess, the concentration and time evolution of the erosion coefficient are computed, etcetera. This process is continued until the desired convergence for $a(r)$ is obtained. The subsequent a_{i+1} is determined with a_i and $\frac{da_i}{dt}$ as follows,

$$a_{i+1} = a_i + \Delta t \frac{da_i}{dt}. \tag{3.19}$$

The convergence of this process is affected by the choice of Δt.

As mentioned in Section 2.3.3, the time evolution of the erosion coefficient does not depict the derivative of $a(r)$ with respect to the physical time but to a pseudo time. This allows to find the erosion coefficient in morphodynamic equilibrium with a time integration method even though the erosion coefficient is not a time dependent variable.

The time evolution of the erosion coefficient, $\frac{da}{dt}$, depends on the divergence of the tidally averaged lateral transport (see equation (2.27)). The total tidally averaged depth integrated lateral transport is given in equation (2.23). Because along-channel uniformity is assumed, the divergence only consists of the derivative with respect to r. This means the time evolution of the erosion coefficient can be expressed as,

$$\frac{da}{dt} = -\frac{1}{r}\frac{\partial}{\partial r}(rT_{tot}) = -\frac{\partial T_{tot}}{\partial r} - \frac{T_{tot}}{r}. \tag{3.20}$$

For the derivative with respect to r, a finite difference method is used. The transport T_{tot} is approximated as the sum of T_{M_0}, T_{M_2} and T_{dif}, defined in equations (2.24)-(2.26). The integrals that need to be evaluated to compute the transport are approximated with the composite trapezoidal rule.

The morphodynamic equilibrium condition holds if there is no total tidally averaged lateral transport. In that case the time evolution of the erosion coefficient is zero over the whole transect and thus the expression for a does not change anymore once the morphodynamic equilibrium is reached. To check if the iteration process for a is converging, the relative difference between the new and the previous a is computed, this is called δ_i,

$$\delta_i = \frac{\|a_{i+1} - a_i\|_2}{\|a_{i+1}\|_2}. \tag{3.21}$$

When δ_i is below a chosen value, the process is converged sufficiently and the iteration process is terminated.

4

Results

In this chapter the results of several simulations obtained with the model described in Chapter 2 and 3 are shown and discussed. In Section 4.1, results for the flow only are shown, with the aim to obtain a more thorough understanding of the behaviour of the advective contribution to the lateral flow in estuaries, providing an answer to the first four research questions posed in Section 1.3. The results of the simulations including sediment are discussed in Section 4.2 providing an answer to research questions five and six.

4.1. Results for the flow

In this section the flow for a tide dominated estuary is investigated. The default parameters are characteristic for a tide dominated estuary and are discussed in Section 4.1.1. In this section the flow characteristics for this reference situation are discussed as well. In subsequent sections, one or more of the parameters are varied, such that the sensitivity of these parameters can be systematically identified by comparing the resulting flow with the flow in the reference situation. The last part of this section contains an idealised simulation of a cross-section in the Ems, for which the results are compared with measured data.

4.1.1. Reference situation

The reference parameter values are based on the values used in [11] for a tide dominated estuary. The bottom profile is Gaussian with a width of 3.75 kilometres, and a depth between 5 and 15 metres. To approximate a straight channel, the radius of curvature is taken very large (10^8 m) and curvature terms are not included in the model equations. Moreover, it is assumed the estuary is located in the Northern Hemisphere, so the Coriolis parameter is positive. The prescribed discharge consists of an M_0 and M_2 component and the density gradients are assumed to be zero in the reference situation. In Table 4.1 the values for the parameters in the reference situation are tabulated. The results obtained with these parameter values are shown in Figure 4.1 for the cross-channel flow and in Figure 4.2 for the along-channel flow.

In Figure 4.1a the residual cross-channel velocity is shown with a positive value indicating that the water is directed towards the right and a negative velocity means the flow is directed to the left. In the upper part of the channel the flow is directed towards the right, whereas in the lower part the flow is directed towards the left. This results in a clock-wise circulation of water. This circulation can be explained by the Coriolis deflection. The Coriolis effect is caused by the rotation of the earth. It causes moving objects on earth to be deflected to the right in the Northern hemisphere and to the left in the Southern hemisphere. Since the water in the upper half of the estuary is moving faster, the water is deflected more to the right near the surface than near the bottom. Because the depth integrated cross-channel velocity must be zero at every point along the transect (see equation (2.5)), this results in a velocity directed to the right at the top of the estuary and a velocity to the left at the bottom of the estuary.

In Figure 4.1b the amplitude of the M_2 velocity is shown, whereas the corresponding phase is shown in Figure 4.1c. The phase indicates the phase difference with respect to the tidal discharge, which is

Table 4.1: The parameters values used for the reference situation.

Parameter	Symbol	Value	Unit
River discharge	$Q^{(0)}$	3000	m^3/s
Amplitude of tidal discharge (M_2)	$Q^{(c)}$	30000	m^3/s
Phase of tidal discharge (M_2)	φ_Q	0	rad
Horizontal diffusion coefficient	A_h	1	m^2/s
Vertical diffusion coefficient	A_v	0.006	m^2/s
Channel width	W	3750	m
Maximal water depth	H_{max}	15	m
Minimal water depth	H_{min}	5	m
Radius of curvature	R	10^8	m
Gravitational acceleration	g	9.81	N/kg
Coriolis parameter	f	10^{-4}	s^{-1}
Reference water density	ρ_0	1000	kg/m^3
Base tidal frequency	ω	$2\pi/44714$	s^{-1}

defined to have phase 0. This figure shows that the upper half of the cross-section has a different direction than the lower half of the estuary with the highest amplitudes in the middle of the channel. This can also be explained by the Coriolis deflection of the M_2 component of the along-channel flow. During low tide, when the M_2 along-channel velocity is downstream, the M_2 cross-channel velocity has a clockwise circulation. During high tide, when the M_2 along-channel velocity is directed upstream, the M_2 cross-channel velocity is reversed and has a counter-clockwise circulation.

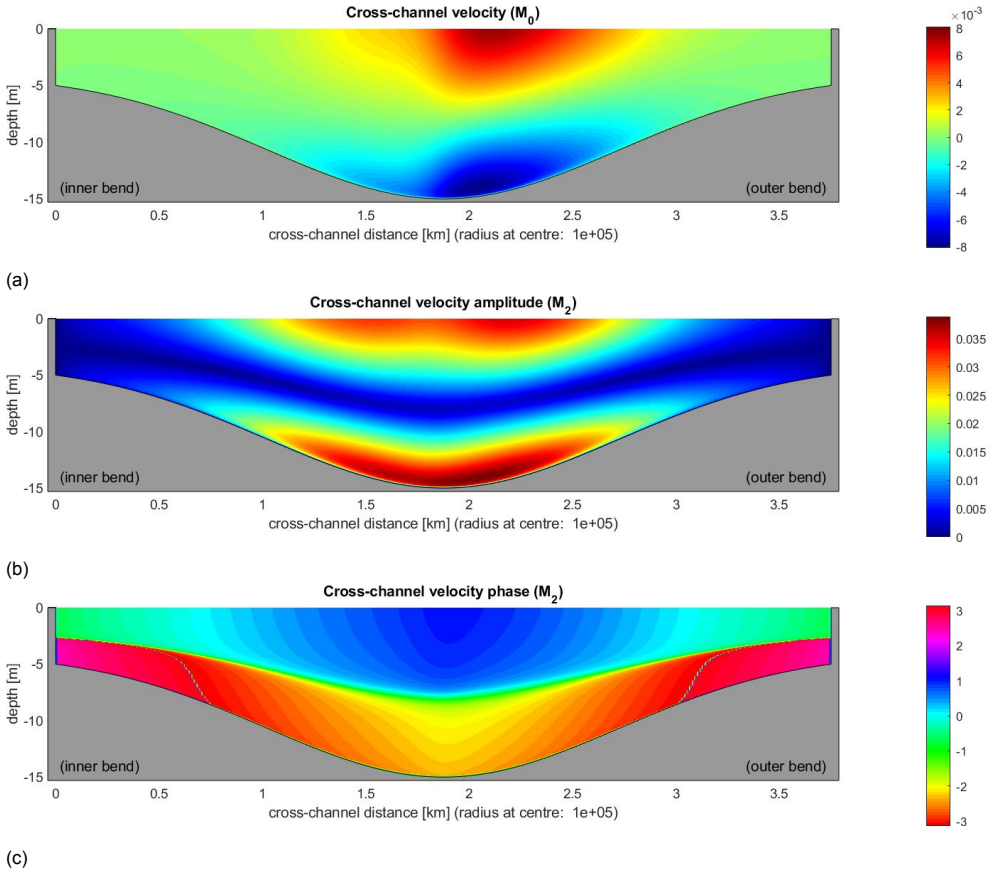

Figure 4.1: The cross-channel velocity profiles in m/s for the reference situation. Figure (a) shows the cross-channel M_0 velocity, in Figure (b) and (c) the amplitude and phase for the cross-channel M_2 velocity are displayed.

In Figure 4.2a the residual along-channel velocity is shown. For the along-channel results a positive M_0 velocity indicates flow towards the sea and a negative velocity means the water is flowing upstream. In Figure 4.2a a a clear maximum is visible in the upper middle of the estuary and the amplitude is decreasing towards the sides. This can be explained by the no-slip boundary conditions on the bottom and side walls which force the flow to be zero there. The amplitude for the M_2 velocity, depicted in Figure 4.2b, is also highest in the upper middle and decreasing towards the sides. From Figure 4.2c it follows that the along-channel M_2 velocity has a phase close to zero over the whole cross-section.

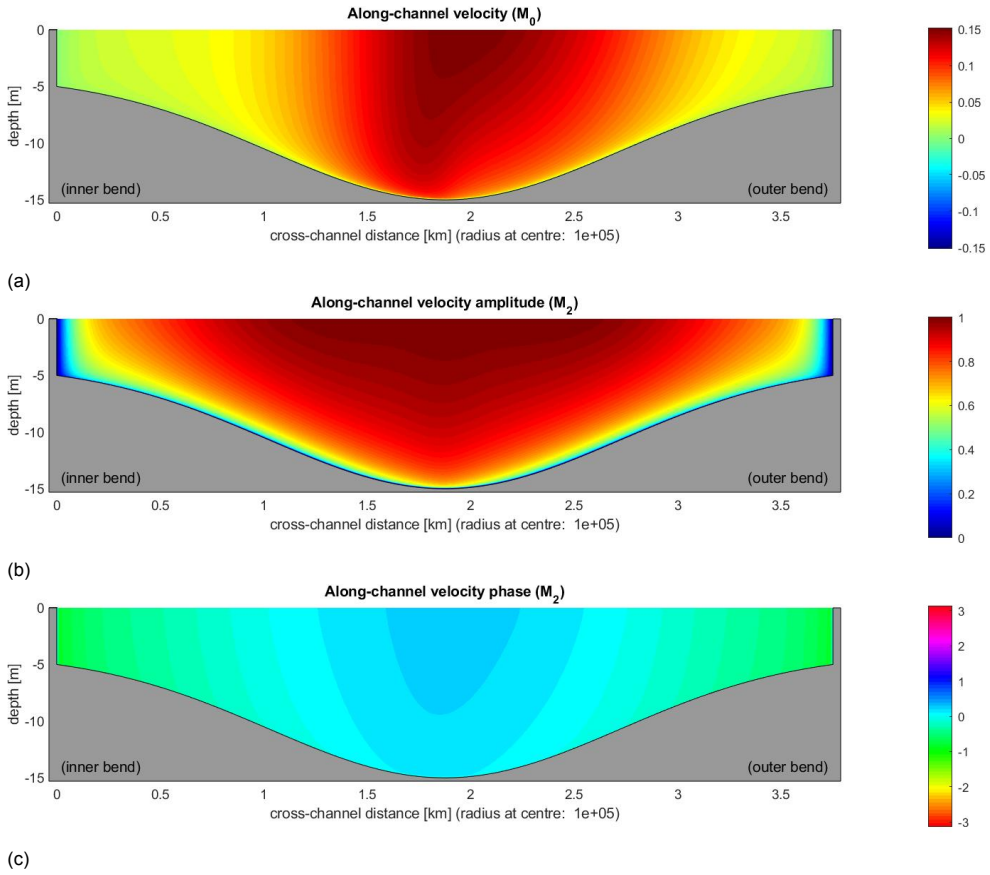

Figure 4.2: The along-channel velocity profiles in m/s for the reference situation. Figure (a) depicts the along-channel M_0 velocity, in Figure (c) and (d) the amplitude and phase for the cross-channel M_2 velocity are shown.

The profiles in Figures 4.1 and 4.2 are not symmetric. To link this to the various mechanisms, Figure 4.3 shows the decomposition of the cross-channel M_0 flow into flows caused by individual forcings (see Section 2.2.3), only non-zero contributions are shown. The decomposition confirms that the M_0 cross-channel velocity (Figure 4.1a), is mainly determined by the flow caused by Coriolis deflection (Figure 4.3a), which has an asymmetric pattern with larger velocities right to the middle axis. The advective contribution (Figure 4.3b), is a factor 20 smaller than the contribution caused by Coriolis deflection and shows a rather complex spatial pattern. The pattern can be characterised as four circulation cells of different sizes. The maximal magnitude of the contribution caused by horizontal diffusion (Figure 4.3c) lies between the magnitude of Coriolis deflection and advection. However, this contribution is small in a large part of the cross-section, only near the surface and bottom boundary are areas with a non-zero velocity visible.

It is not easy to understand the profile for the contribution of advection shown in Figure 4.3b. The forcing for advection consists of the sum of two multiplications of a velocity with the derivative of a velocity. Due to the multiplication of two time dependent variables, not only the M_0 components but also the M_2 components of the flow affect the advection profile because a tidally averaged product of M_2-M_2 signals is not zero.

In the upcoming sections, the sensitivity to different parameter values on the full flow and the flow caused by advection are discussed in detail. Because the research questions of this thesis concern

the residual flow, in the upcoming sections only the M_0 results of the experiments are shown.

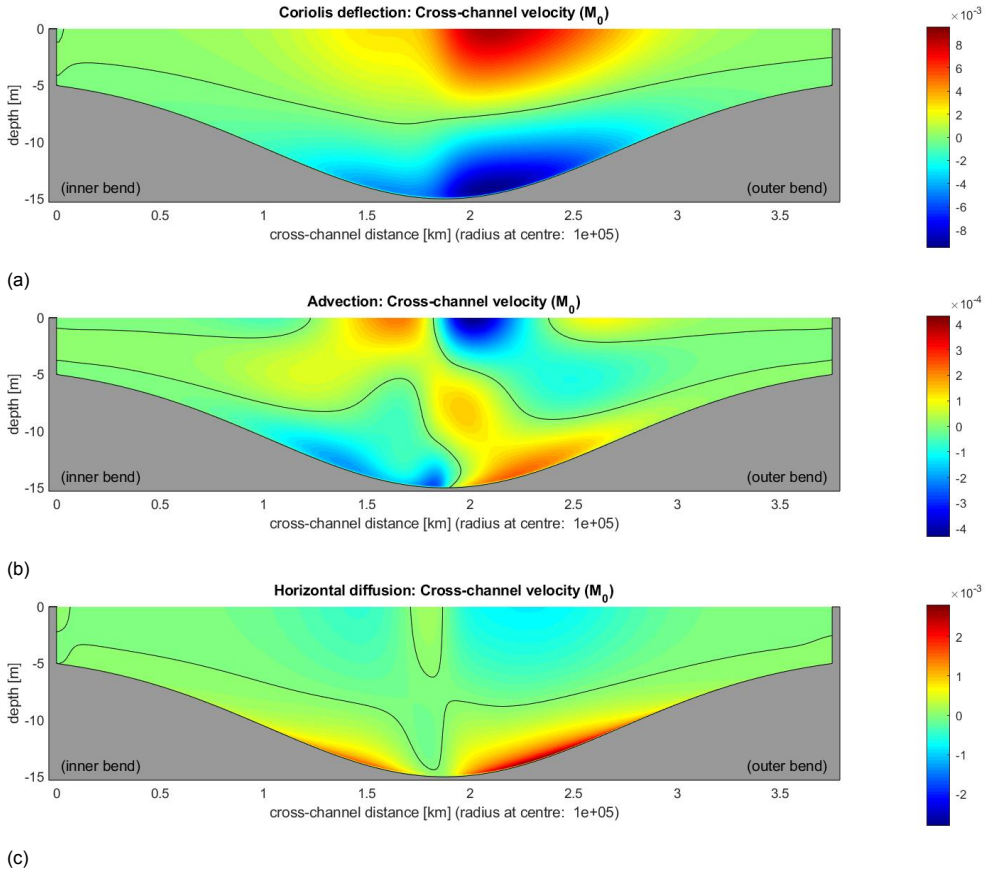

Figure 4.3: The decomposition of total residual cross-channel flow in m/s for the reference situation. The non-zero contributions are resulting from Coriolis deflection (a), advection (b) and horizontal diffusion (c).

4.1.2. Varying channel width

The bathymetry strongly affects the cross-sectional flow profiles. Regarding the influence of bathymetry on the along-channel velocity profiles, [34] concluded that the magnitude of the along-channel advective forcing scales with the local bottom slope and water depth. A flatter bottom results in a smaller contribution of advection whereas for steeper bottom profiles advection has a large contribution to the total flow. To investigate the influence of bathymetry on the cross-channel advective contribution to the cross-channel flow, experiments are done with different channel widths and therefore different lateral bottom slopes.

The choice of profiles is inspired by [23], who made a division in narrow, medium and wide channels, by introducing dimensionless number α defined as the ration between the maximum depth and the width of the estuary. When α is less than 0.002 the estuary is classified as wide/shallow. When α is more than 0.015 the estuary is classified as narrow/deep. In between these two values for α, the estuary is defined as medium. The value for α is 0.004 in the reference situation, which means this is a medium channel. To compare this with a small and wide channel, experiments are done for a channel width of 375 and 37500 metres. This leads to 0.04 and 0.0004 as values for α. The same values for α are used in [23] to compare the flows in a small, medium and narrow estuary.

To see the effect of advection more clearly, the model is run in two different ways for each channel width. Once the model is run without including the contribution of advection in the model equations and once the model is run with advection included in the model equations. In both simulations the contributions caused by discharge, Coriolis deflection and horizontal diffusion are included in the computations. Afterwards the contribution of advection is computed for both results. The method where advection is not incorporated in the model equations but still computed afterwards, is similar to the method used in [12]. Including the contribution of advection in the model equations and computing the magnitude of

this contribution afterwards is similar to the approach in [34].

In Figure 4.4 the profiles for the cross-channel M_0 velocity are shown when advection is not included in the model equations. The cross-channel velocity profiles resulting from excluding advection from the model equations are symmetric. This is remarkable because Coriolis deflection, which is included in these computations, generally breaks the symmetry of the cross-channel flow. An explanation for the symmetry of the flow profiles in this simulation is that the along-channel flow is symmetric for a symmetric bottom profile when only the contributions of discharge and diffusion are included. Consequently, when Coriolis deflection is included this also leads to a symmetric contribution because the deflection of a symmetric flow is symmetric. As a result, both the along-channel and cross-channel flows are symmetric.

The width of the channel does not affect the characteristics of the flow in these simulations, each of the profiles shows one clockwise circulation cell. The magnitude differs for the varying channel widths because the same discharge is used for each of the channels. As a result the velocity is high in the narrow channel and lowers as the channel gets wider.

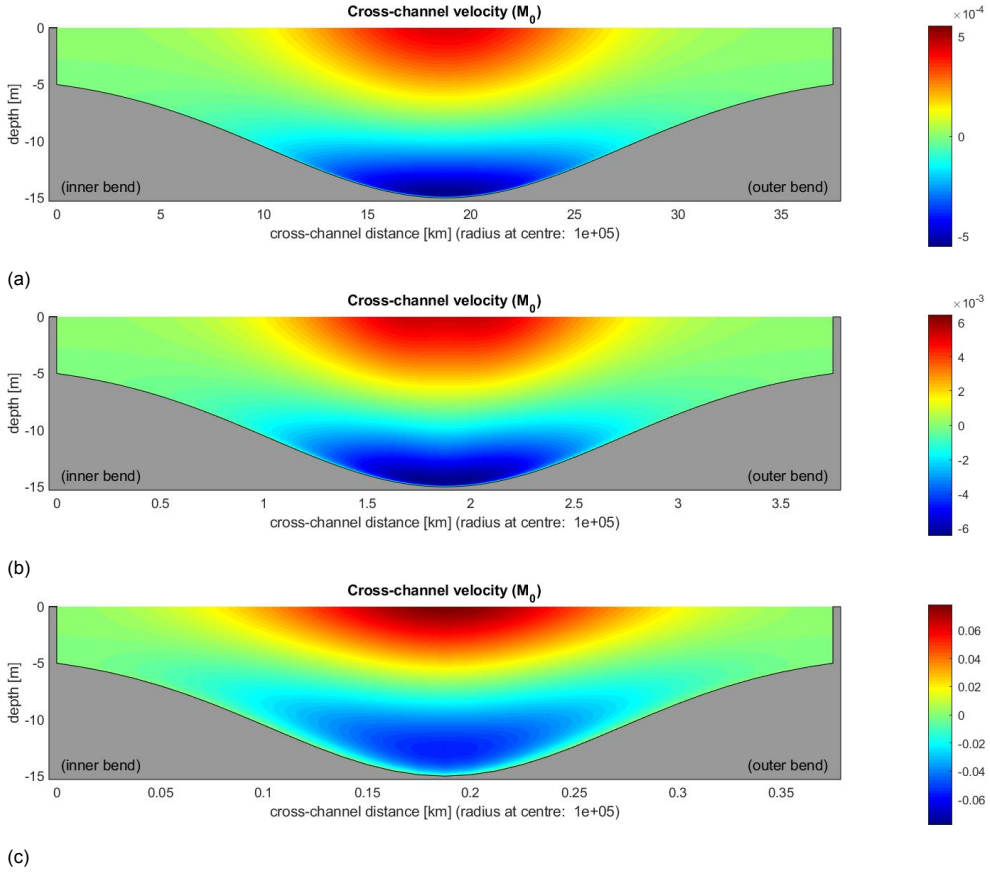

Figure 4.4: The results for the cross-channel flow in m/s when advection is not included in the model equations for a wide (a), medium (b) and narrow (c) estuary.

Figure 4.5 shows the cross-channel velocity when advection is included in the model equations. The flow for a wide channel (Figure 4.5a) is similar to the flow in a wide channel computed without including advection (Figure 4.4a). The velocity profile is symmetric and has one clockwise circulation cell, the magnitude of the flow is also similar for both results. In the medium channel (Figure 4.5b), the velocity is slightly asymmetric, the velocity is higher on the right of the middle axis. The flow profile can still be characterised as one clockwise circulation cell but differs from the profile computed without advection (Figure 4.4b) which was symmetric. The flow in the narrow channel (Figure 4.5c) is clearly different than the profile in the previous simulation (Figure 4.4c). The profile now consists of two circulation cells instead of one. There is a large clockwise circulation cell and a small counter-clockwise circulation cell on the left of the channel.

When comparing Figure 4.4 and Figure 4.5, there is hardly any difference visible between the ve-

locity profiles for the wide channel (Figures 4.4a and 4.5a). For the narrow channel (Figures 4.4c and 4.5c), the profiles have not much in common anymore. This means the advective contribution hardly affects the flow in the wide channel whereas it has a large effect on the flow in the narrow channel.

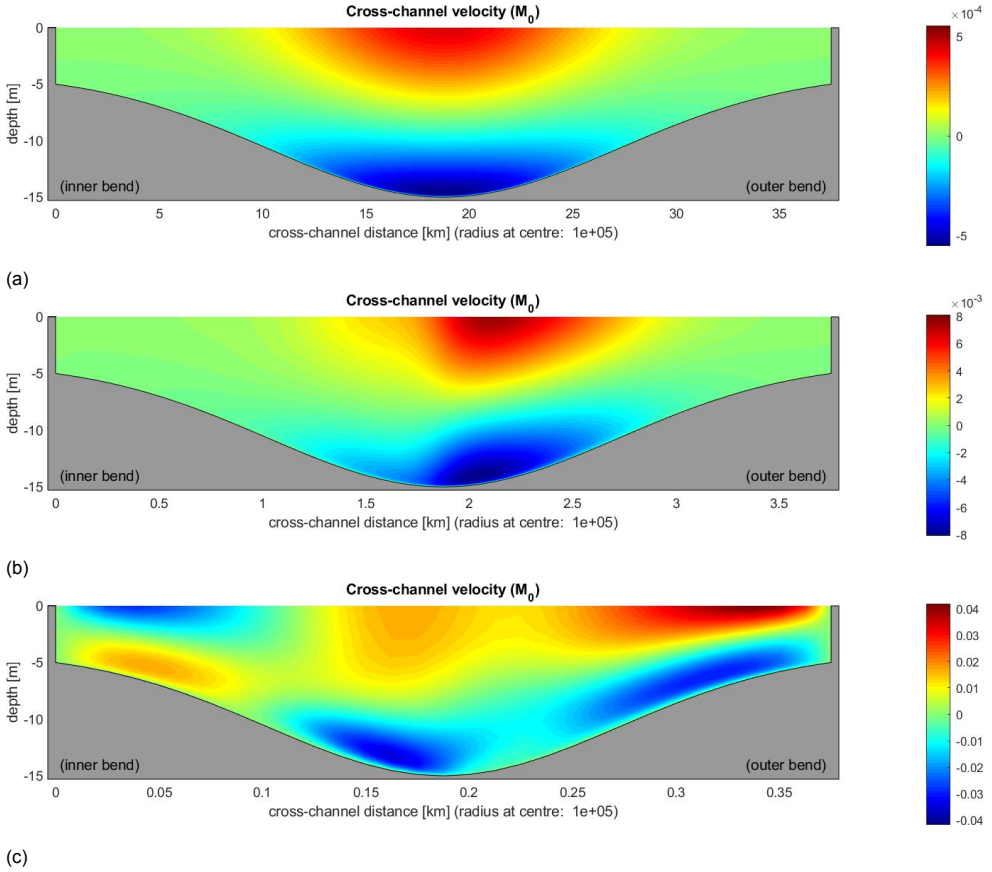

Figure 4.5: The results for the cross-channel flow in m/s when advection is included in the model equations for a wide (a), medium (b) and narrow (c) estuary.

Figure 4.6 shows the computed advective contribution to the flow when advection was not included in the model equations. Figure 4.7 shows the advective contribution to the flow when advection was included in the model equations. Based on the previous results, the profiles for the wide channel should be almost equivalent for both methods and the profiles for the narrow channel should show a lot of difference.

Exactly the expected behaviour can be observed in the figures. For the wide channel (Figures 4.6a and 4.7a) a strong resemblance is visible between the two results. For the narrow channel (Figures 4.6c and 4.7c), the difference between the two patterns is very large. Both figures for the narrow estuary show two circulation cells but the direction of the circulations is exactly opposite. Moreover, the magnitude of the velocity is a factor ten larger in Figure 4.6c than in Figure 4.7c. As a consequence, the magnitude for the advective contribution in Figure 4.6c is also larger than the magnitude of the total cross-channel flow. For the medium channel (Figures 4.6b and 4.7b) the difference between the two profiles is smaller than for the narrow channel. The magnitude of the contributions is similar but in Figure 4.6b two small circulation cells are present near the bottom whereas these are absent in Figure 4.7c.

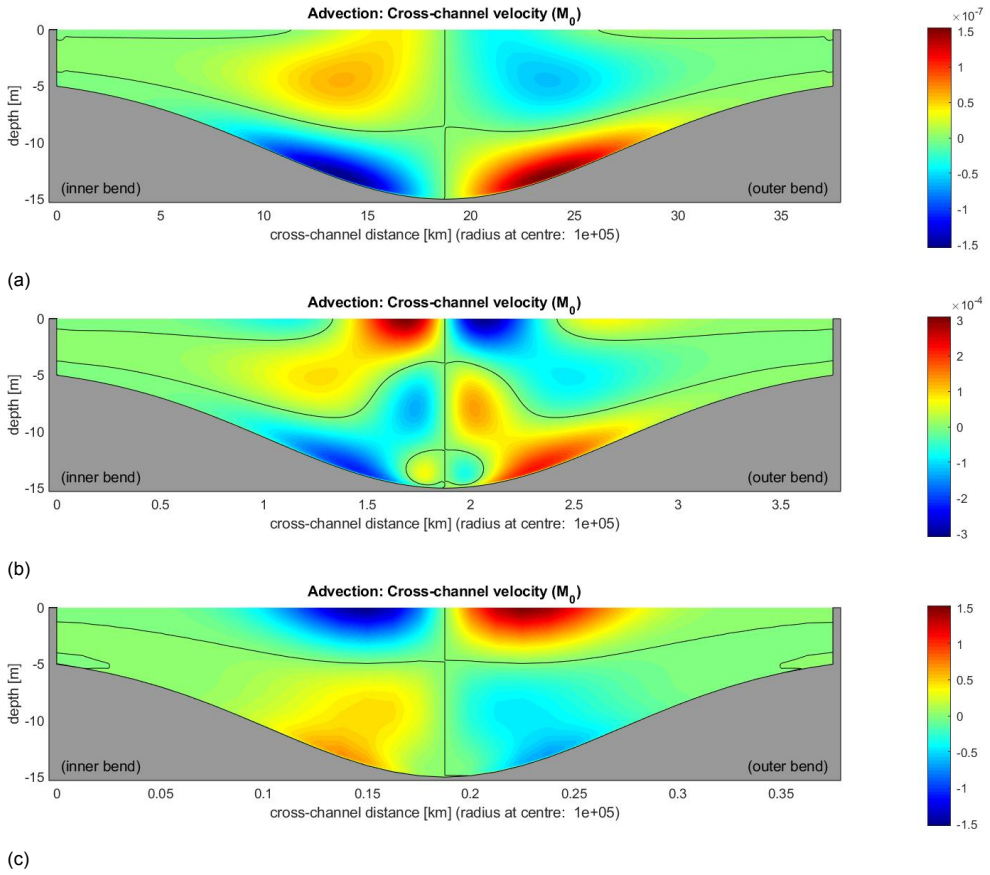

Figure 4.6: The results for the computed contribution of advection to the cross-channel flow in m/s when advection is not included in the model equations for a wide (a), medium (b) and narrow (c) estuary.

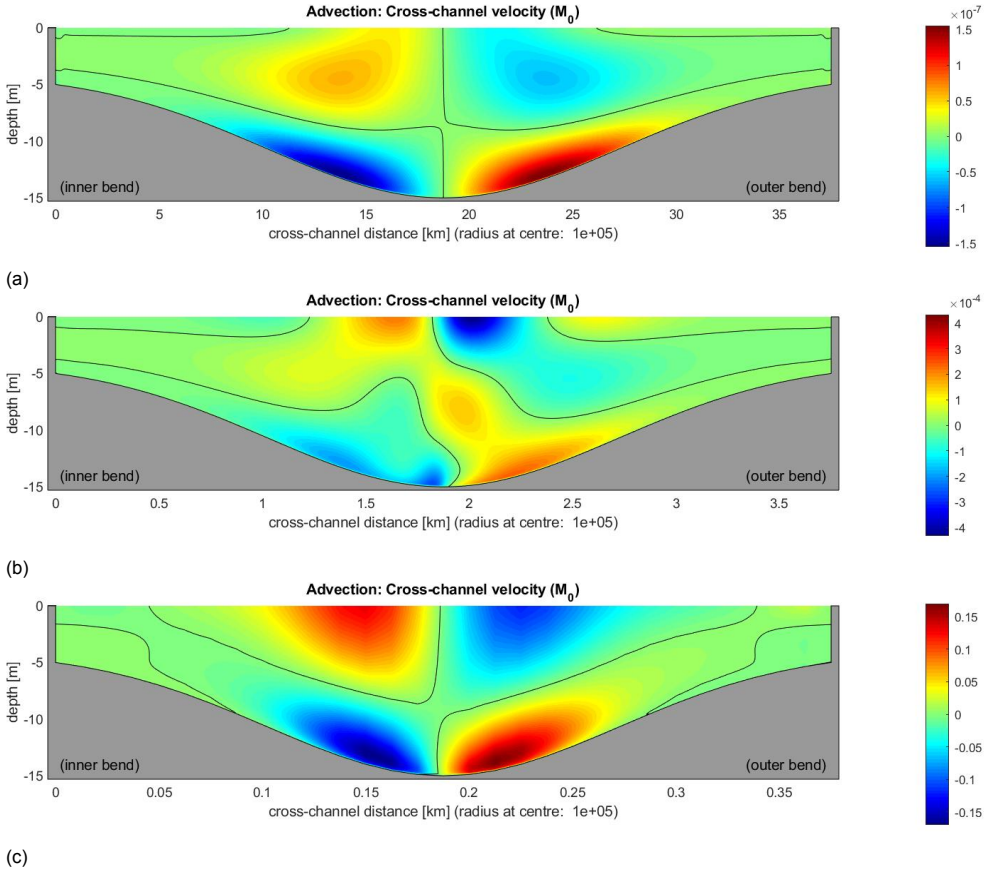

Figure 4.7: The results for the contribution of advection to the cross-channel flow in m/s when advection is included in the model equations for a wide (a), medium (b) and narrow (c) estuary.

The advection profiles for the wide and narrow channel, Figures 4.7a and 4.7c look much alike, even though the significance for the flow profile is very different. Both consist of two circulations with the water flowing downward in the middle and upward on the sides. To see if these contributions are build up in the same way, the advection profile is decomposed into two flow profiles related to different components of the forcing. The cross-channel advection is caused by two forcing terms, $-u_r \frac{\partial u_r}{\partial r}$ and $-u_z \frac{\partial u_r}{\partial z}$. Figure 4.8 shows the decomposition into the flow caused by each of these forcings for a wide channel, the forcings itself are also visualised in this figure. Figure 4.9 shows these results for a narrow channel.

When comparing Figures 4.8 and 4.9, one can see that the pattern of the forcings is similar for the wide and narrow channel. For both cases, the profiles for the forcing $-u_r \frac{\partial u_r}{\partial r}$ (Figures 4.9b and 4.8b) consist of four circulation cells and the profiles for the forcing $-u_z \frac{\partial u_r}{\partial z}$ (Figures 4.9d and 4.8d) consist of two circulation cells. However, the patterns are not exactly equivalent because the distribution of the areas with a similar directions varies for the different channels. For the wide channel the two bottom areas are very thin. For the narrow channel these areas are also thinner compared to others but much thicker than those for the wide channel. The magnitudes of the different components is also distributed differently.

As a consequence of the different forcings, the corresponding flows are also different. For the wide channel four circulation cells are clearly visible for the flow (Figures 4.8a and 4.8c), for the narrow channel the flow profile consists of two cells (Figures 4.9a and 4.9c). Remarkably, in both channels the total contribution of advection results in two circulation cells (Figures 4.7a and 4.7c). It appears that the patterns containing four circulation cells merge and partly cancel such that a profile with two circulation cells is obtained.

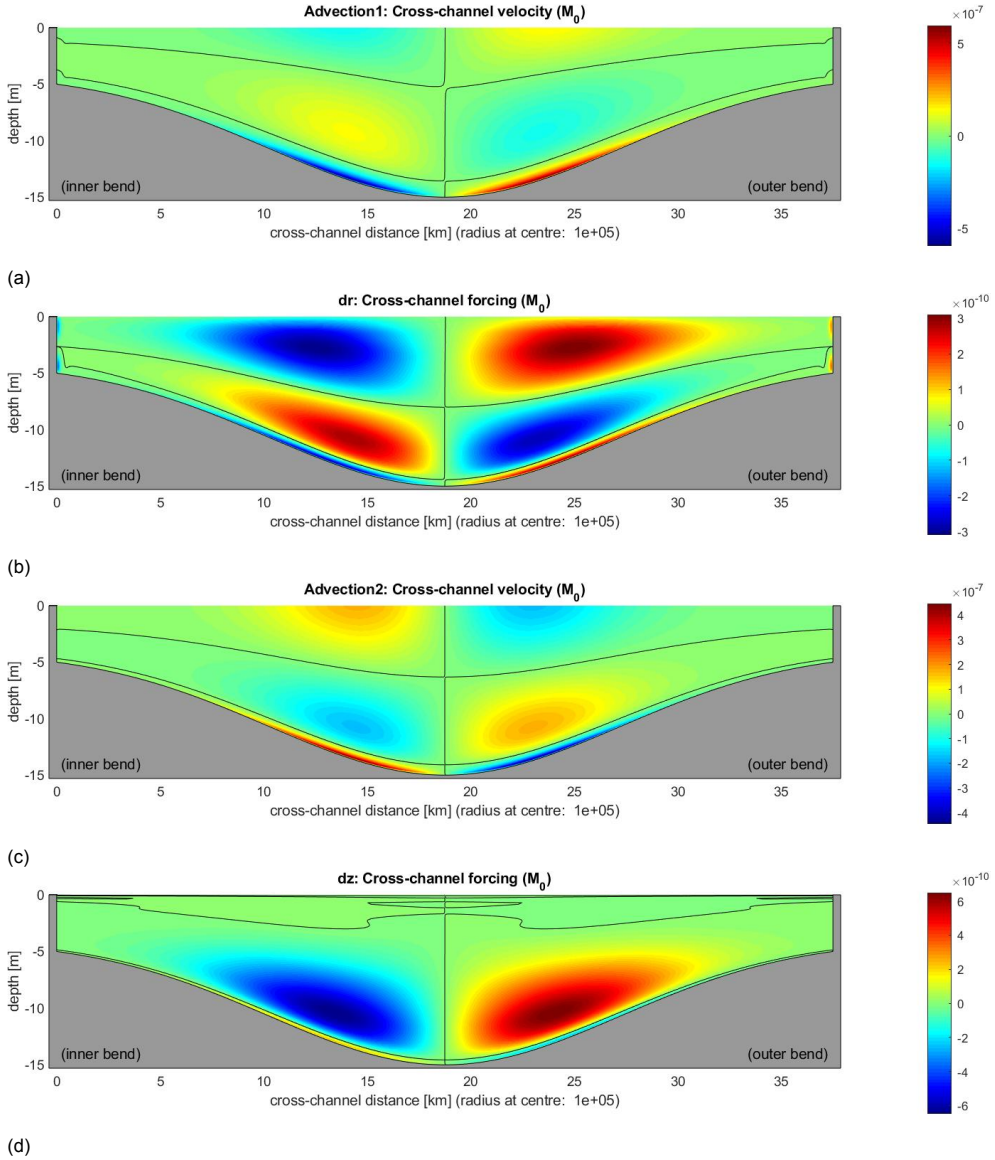

Figure 4.8: The results for a wide channel when advection is included in the model equations. The cross-channel advective flow is decomposed into a flow caused by $-u_r \frac{\partial u_r}{\partial r}$ (a) and a flow caused by $-u_z \frac{\partial u_r}{\partial z}$ (c). The forces causing these flows are shown underneath the corresponding flow ((b) and (d)). The unit of the flow is m/s, the unit for the forces is m/s^2.

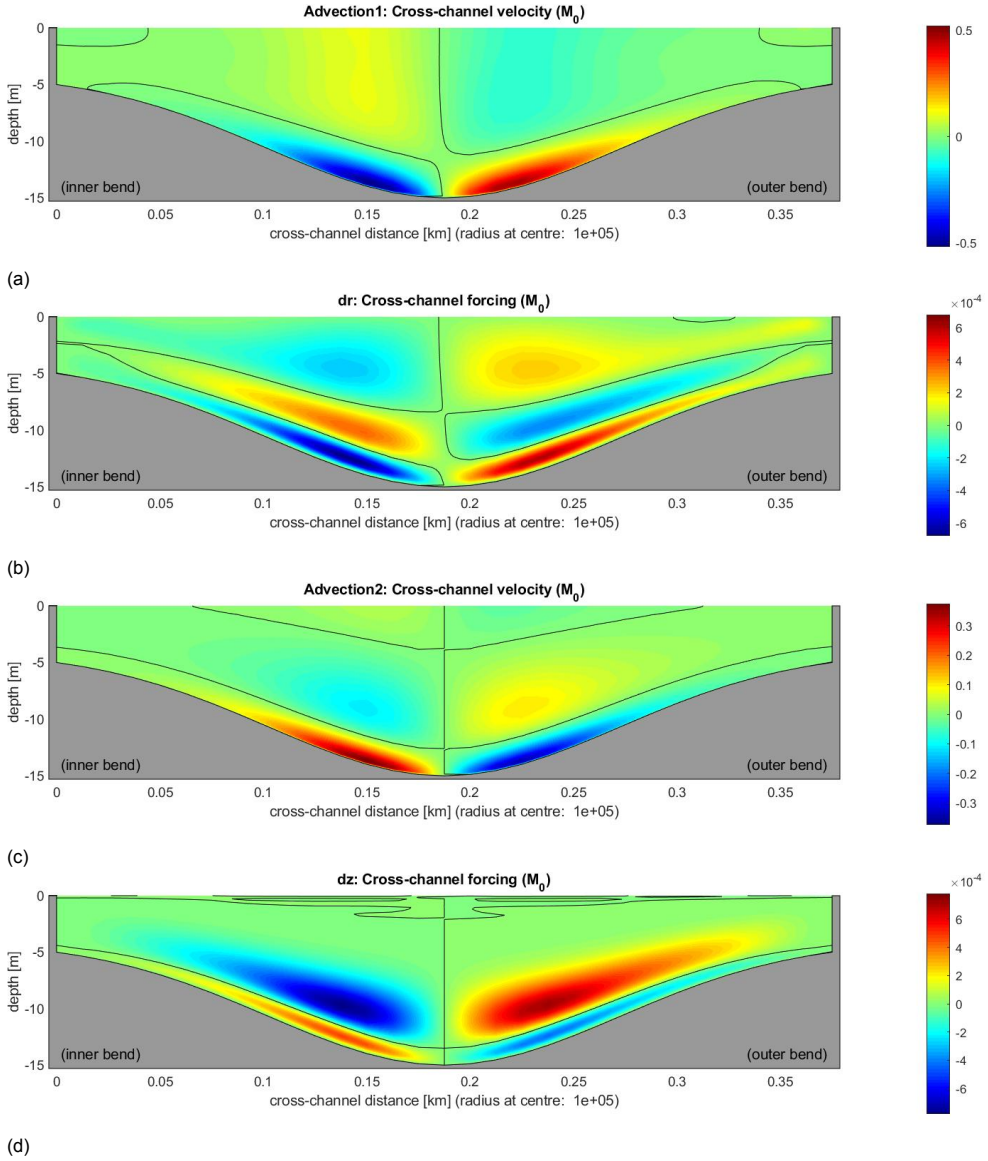

Figure 4.9: The results for a narrow channel when advection is included in the model equations. The cross-channel advective flow is decomposed into a flow caused by $-u_r \frac{\partial u_r}{\partial r}$ (a) and a flow caused by $-u_z \frac{\partial u_r}{\partial z}$ (c). The forces causing these flows are shown underneath the corresponding flow ((b) and (d)). The unit of the flow is m/s, the unit for the forces is m/s^2.

The difference between the contribution of advection for the cross-channel flow in a wide, medium and narrow channel showed that advection can often not be assumed negligible. The channel width, and thus also the bottom slope, is a parameter affecting the magnitude of the advective forcing. This is consistent with the findings in [34] for along-channel flow. More research with for example more complicated bottom profiles should be conducted to investigate if other aspects of the bathymetry are also affecting the significance of advection for the total flow dynamics.

Based on these results it is recommended to only neglect advection when dealing with a gradual bottom profile. Moreover, when the contribution of advection is not included in the model equations, it is advisable to compute the contribution of advection afterwards to check if this simplification was indeed allowed. If the advective contribution computed afterwards is small compared to the other contributions, it was valid to neglect advection. However, if the contribution of advection computed afterwards is not small compared to the other contributions, the results might be inaccurate. In that case it is recommended to include advection in the computations.

4.1.3. Varying channel curvature

In the reference situation presented in Section 4.1.1, a straight channel is simulated. To investigate the influence of curvature on the flow profile the radius of curvature is decreased, leading to a more acutely curved estuary. Simulations are performed for various radii of curvature. Apart from the radius of curvature R, all other parameters are equivalent to the reference situation (see Table 4.1). The radii of curvature that are chosen here are, 100 km, 10 km, 1 km and -10 km. When the radius of curvature is positive, the inner bend is on the left when looking in the direction of the sea. To find the inner bend on the right when looking seaward, the the radius of curvature should be chosen negative.

The results for the different radii can be found in figures 4.10 - 4.13. In each figure the total cross-channel flow is depicted in panel (a) at the top and the profiles associated with the flows caused by different contributions are shown in panels (b)-(e) below. The panels show the the flow caused by Coriolis deflection, advection, horizontal diffusion and curvature.

For a radius of 100 km the cross-channel flow profile (Figure 4.10a) mainly results from the Coriolis deflection (Figure 4.10b). Comparing the flow pattern to the reference situation (Figure 4.1a), not much difference is visible, only the area where the velocity is nonzero, is spread out slightly more to the left of the channel. This can be explained by the contribution of curvature. The flow caused by curvature (Figure 4.10e) consists of one clockwise circulation cell similar to the Coriolis deflection but the area with a non-zero velocity is spread out more evenly compared to the flow caused by Coriolis deflection which is mostly located right to the middle axis. The contributions caused by advection and horizontal diffusion (Figures 4.10c and 4.10d) are similar to the reference situation. The flow caused by advection is approximately a factor 10 smaller than the other contributions and the non-zero flow caused by horizontal diffusion is only located near the bottom and surface boundary. Therefore, advection and horizontal diffusion do not have a large effect on the cross-channel flow.

When considering a radius of 10 km (Figure 4.11), the contribution due to the curvature is the largest contribution to the cross-channel flow. Compared to the simulations for a radius of 100 km, the contribution caused by curvature is increased by approximately a factor 10 whereas the contribution caused by Coriolis deflection has almost the same magnitude. Consequently, the flow profile is mainly determined by the curvature (Figure 4.11e) but Coriolis deflection (Figure 4.11b) also significantly affects the flow profile (Figure 4.11a). Note that for the Coriolis deflection another circulation cell has appeared left to the middle axis. The magnitude of the velocity there is much smaller, so this does not affect the total flow significantly. Since the contributions for Coriolis deflection and curvature both mainly result in a clockwise circulation, the two processes amplify each other. As a consequence the characteristics of the flow profiles for $R = 100$ km (Figure 4.10a) and $R = 10$ km (Figure 4.11a) are very similar. However, the magnitude of the velocity has increased approximately a factor three for the smaller radius of curvature, this is due to the increased magnitude of the contribution caused by curvature. Similarly, the profiles for advection and horizontal diffusion for a radius of 10 km (Figures 4.11c and 4.11d) also have the same characteristics as these contributions had for a radius of curvature of 100 km but their magnitude is increased approximately a factor three.

As expected, the contribution of curvature for a radius of 1 km is larger than for the previous radii of curvature. The contribution caused by curvature (Figure 4.12e), is approximately a factor five larger than for the radius of 10 km. As a consequence the total flow (Figure 4.12a) is mainly determined by curvature. For the radii of 10 km and 100 km the profiles for the contribution of curvature are almost symmetric but for the radius of 1 km the circulation is clearly located more on the left side of the estuary. This also affects the other contributions which all have an altered profile. The contribution caused by Coriolis deflection (Figure 4.12b) now clearly consists of two circulation cells with a counter-clockwise circulation on the left and a clockwise circulation on the right side of the channel. The magnitude of the velocity is approximately halved for this contribution whereas the other contributions have all increased in magnitude. The magnitude of the advective contribution (Figure 4.12c) is increased by approximately factor ten and the profile is also changed. For a radius of 100 and 10 km the profile consisted of four circulation cells, for a radius of 1 km there are again four circulation cells but the rotation of the cells on the left is reversed. The contribution caused by horizontal diffusion (Figure 4.12d) is now higher on the left side of the channel, previously the contribution on the left and right side were of equal magnitude. The maximum velocity is increased by approximately a factor six.

For the radius of -10 km the circulation cell in the contribution caused by curvature (Figure 4.13e) is reversed, now the curvature causes a counter-clockwise circulation with approximately the same magnitude as the contribution of curvature for the radius of 10 km. Since the Coriolis deflection (Figure

4.13b) is characterised as one clockwise circulation cell, the contributions of curvature and Coriolis deflection now counteract each other. The magnitude of the contribution caused by the Coriolis deflection is much smaller than the contribution caused by curvature, therefore the total flow (Figure 4.13a) is characterised by a counter clockwise circulation. Due to the opposite circulation of the flow, the horizontal diffusion (see Figure 4.13d) is also opposite compared to the contribution for a positive radius of curvature. The contribution caused by advection (Figure 4.13c) consists of five circulation cells, one small cell near the bottom and four large cells which have the same direction and approximately the same distribution as the advective contribution for a radius 100 and 10 km. The the advective contribution is also of the same order of magnitude as the contribution for a radius of 10 km.

These experiments show that curvature strongly affects the total cross-channel flow. If the channel is bending to the left, when looking seaward, the Coriolis deflection and curvature both contribute to a clockwise circulation, consistent with the results in [12] and [34]. If the channel is bending to the right, the curvature yields a counter-clockwise circulation and hence the Coriolis deflection and curvature counteract. It depends on the radius of curvature which process is dominant.

The contribution of advection is only slightly affected by the channel curvature in these simulations. The magnitude increased as the radius of curvature decreased but this did not result in a significant contribution of advection to the flow. In case of a very small radius of curvature some circulation cells reversed in the contribution caused by advection.

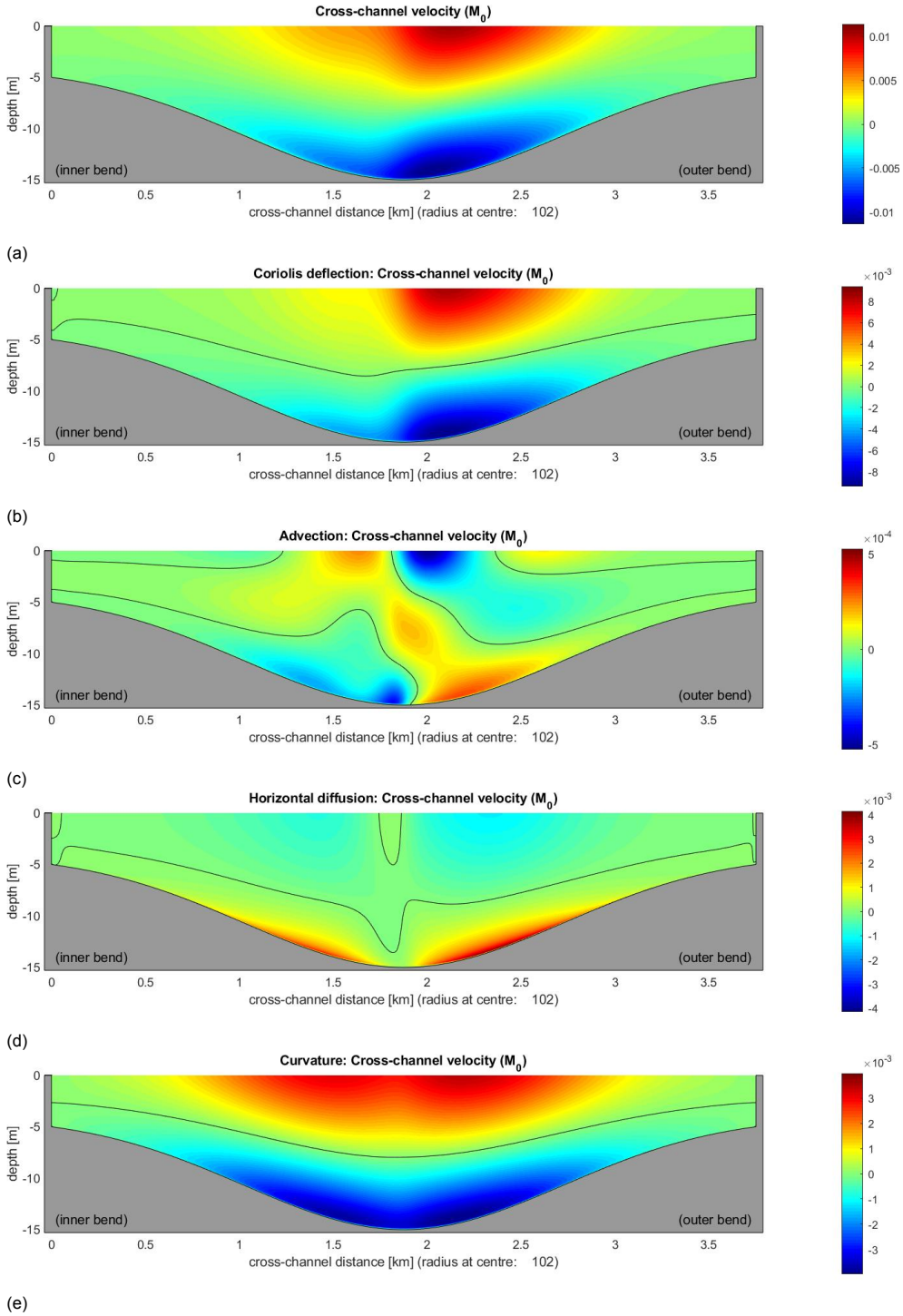

Figure 4.10: Results for the cross-channel flow in m/s for a radius of curvature of 100 km showing the total residual flow (a) and the decomposition of the flow into the contributions for Coriolis deflection (b), advection (c), horizontal diffusion (d) and curvature (e).

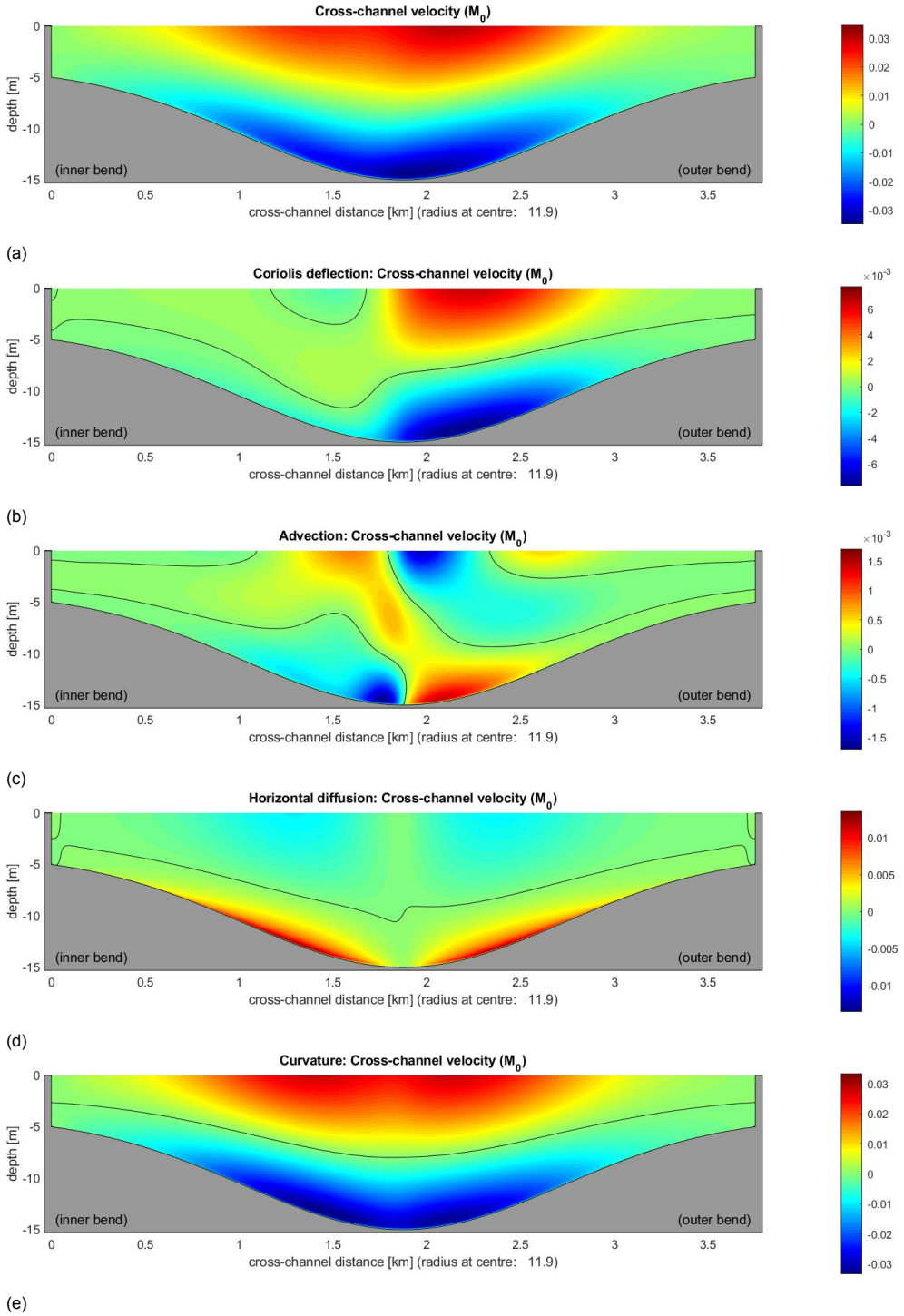

Figure 4.11: Results for the cross-channel flow in m/s for a radius of curvature of 10 km showing the total residual flow (a) and the decomposition of the flow into the contributions for Coriolis deflection (b), advection (c), horizontal diffusion (d) and curvature (e).

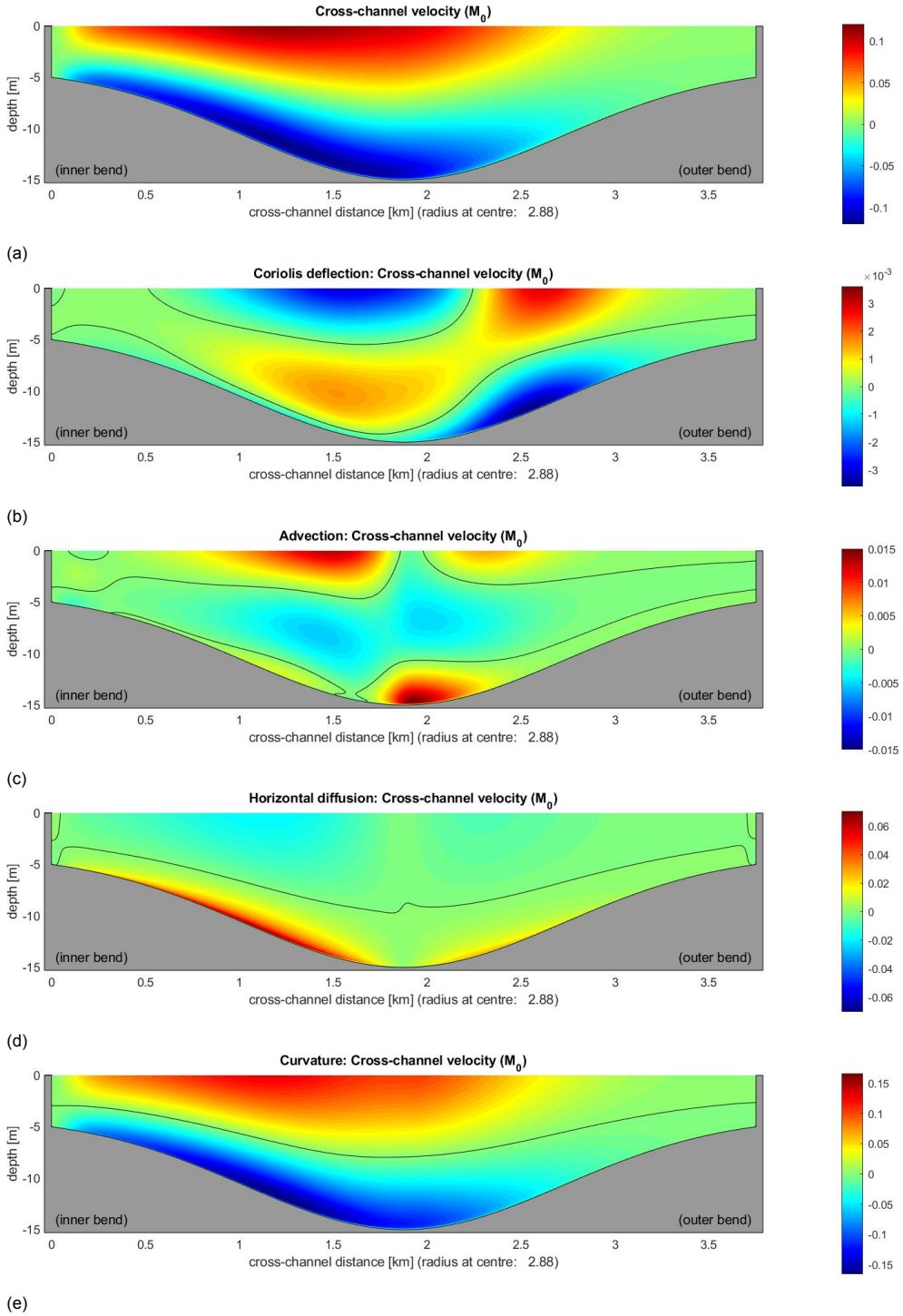

Figure 4.12: Results for the cross-channel flow in m/s for a radius of curvature of 1 km showing the total residual flow (a) and the decomposition of the flow into the contributions for Coriolis deflection (b), advection (c), horizontal diffusion (d) and curvature (e).

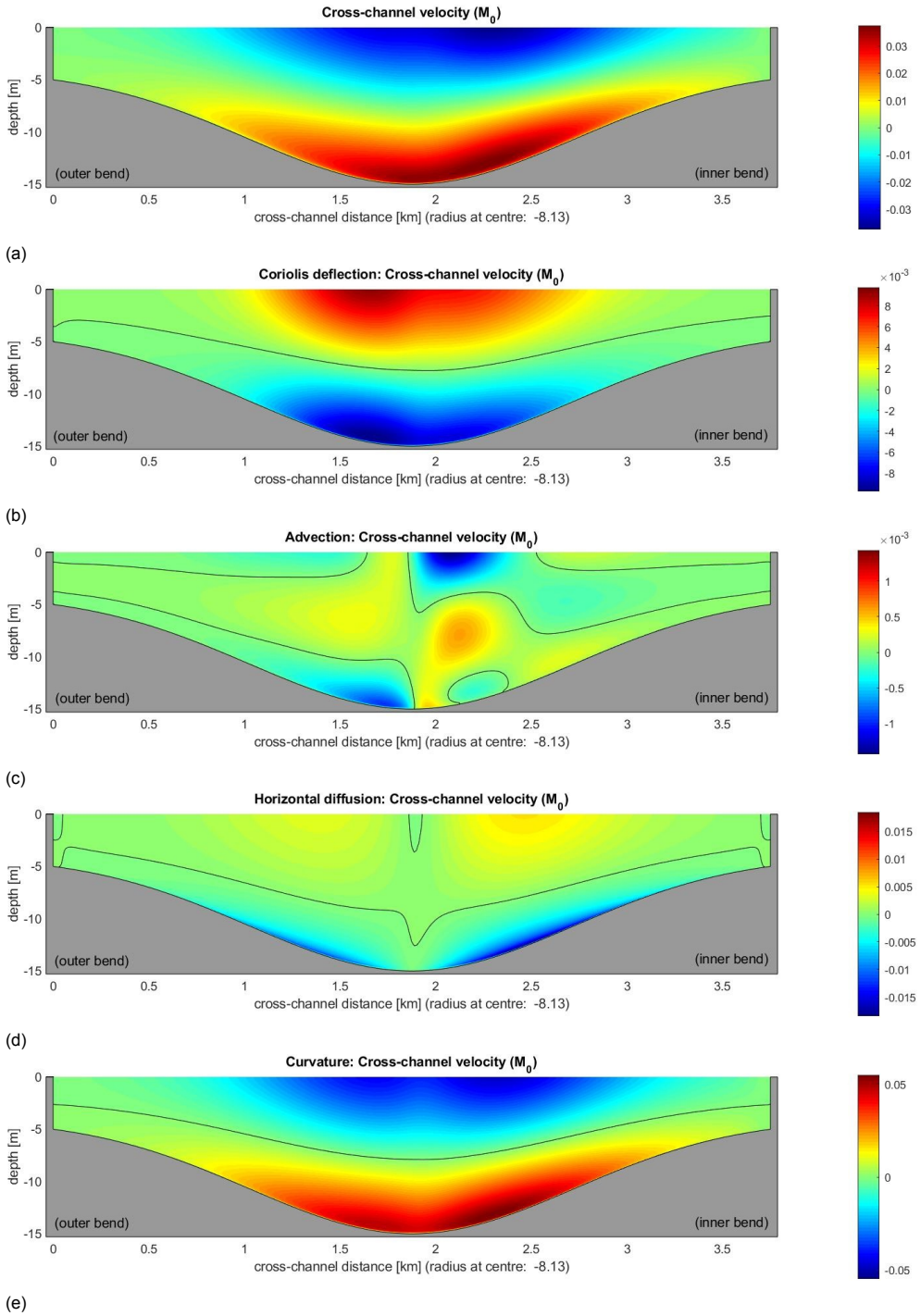

Figure 4.13: Results for the cross-channel flow in m/s for a radius of curvature of -10 km showing the total residual flow (a) and the decomposition of the flow into the contributions for Coriolis deflection (b), advection (c), horizontal diffusion (d) and curvature (e).

4.1.4. Varying cross-channel density gradient

In the reference situation, density gradients are neglected. It is well known that density gradients can result in intricate flow patterns consisting of one or multiple circulations depending on the distribution of the density gradient [12], [15]. To systematically study the effect of a cross-channel density gradient on the cross-channel advective contribution of the flow, simulations with various density gradients are performed. Keeping all other parameters as in the reference situation (see Table 4.1).

The cross-channel density gradient consists of different tidal components. For this experiment only the M_0 and M_2 components of the density gradient are considered by choosing one amplitude for the M_0 contribution and varying the amplitude of the M_2 contribution and the phase of the M_2 contribution. In each of the following simulations the density gradient is spatially uniform. For the first experiments, the M_0 component of the lateral density gradient is chosen to be -10^{-4} kg/m^4, the phase of the M_2 component is set to π and the M_2 amplitude is varied between 10^{-2}, 10^{-3} and 10^{-4} kg/m^4. In the second set of experiments, the M_0 component is again -10^{-4} kg/m^4, the amplitude of the M_2 component equals 10^{-2} kg/m^4, and the phase is given by $-1/2\pi$, 0 or $1/2\pi$. The results of the first three simulations, where the amplitude of the M_2 component is varied, are shown in Figures 4.14-4.16. The results for the other three experiments, with a varying M_2 phase, are shown in Appendix I.

When comparing the flow shown in Figure 4.14a with the reference situation (Figure 4.1a) it is immediately clear that due to the presence of a lateral density gradient the circulation of the cross-channel flow changed from a clockwise to a counter-clockwise rotation. The contribution caused by the density gradient (Figure 4.14e) also shows a counter-clockwise circulation and it has the highest magnitude of all contributions. This is as expected because for a negative density gradient the water on the left of the estuary has a higher density than on the right of the channel. Heavy water flows underneath lighter water and thus there is a counter-clockwise circulation.

The contribution caused by the Coriolis deflection was the dominant contribution for the reference situation. In this simulation the contribution caused by Coriolis deflection (Figure 4.14b) still contains one clockwise circulation cell with a similar magnitude as the reference situation but its magnitude is smaller than the contribution caused by the density gradient. The advective contribution (Figure 4.14c) can be characterised as five circulation cells with a magnitude slightly smaller than the magnitude of the advective contribution in the reference situation. Due to the reversed direction of the flow, the contribution caused by diffusion (Figure 4.14d) is also reversed compared to the reference situation but the magnitude is similar. The contribution of diffusion on the left side of the channel is slightly larger than on the right side.

For the M_2 amplitude equal to 10^{-3}, the flow is still counter-clockwise (Figure 4.15a) due to the contribution of the density gradient (Figure 4.15e) which has not changed. The tidally averaged flow caused by the density gradient has not changed compared to the previous simulation because only the amplitude of the M_2 component of the density gradient has changed. However, the other contributions have changed in characteristics and magnitude due to the higher M_2 amplitude of the density gradient. The contribution caused by to Coriolis deflection (Figure 4.15b) is now largest on the left of the estuary whereas this was largest on the right in the reference situation (Figure 4.3a). The magnitude of this contribution has slightly increased compared to the previous simulation. The advective contribution (Figure 4.15c) can now be characterised as four circulation cells and the magnitude of this contribution has almost doubled compared to the result for the M_2 amplitude equal to 10^{-4}. The contribution caused by horizontal diffusion (Figure 4.15d) has a similar magnitude as for the previous simulation but is now slightly larger on the right of the channel.

The flow for the highest M_2 density gradient (Figure 4.16a) consists of four circulation cells because the advective contribution (Figure 4.16c) is now dominant. The characteristics for the advective contribution are similar as for the previous simulation but the magnitude has increased by more than a factor 20, whereas the magnitude for the contribution caused by the density gradient (Figure 4.16e) has not changed. The contribution caused by Coriolis deflection (Figure 4.16b) now consists of two circulation cells and has a similar magnitude as the result for the M_2 amplitude equal to 10^{-3}. The contribution caused by horizontal diffusion (Figure 4.16d) has largely changed compared to the previous simulation. The magnitude of the contribution is increased almost a factor 10 and the profile can now be characterised as six circulation cells next to each other.

Changing the phase of the M_2 density gradient does not seem to affect the flow profile a lot. Figure 4.16 and the figures in Appendix I all have a similar total flow consisting of 4 circulations. Only the contribution caused by Coriolis deflection is affected by the phase difference. When comparing the

contribution of Coriolis deflection for phase 0 and π (Figures 4.16b and I.2b), both have two circulation cells but their direction is reversed. For phase -0.5π (Figure I.1b) there is only one clockwise circulation cell and for phase 0.5π (Figure I.3b) the contribution caused by Coriolis deflection is similar to the contribution for phase π (Figure 4.16b) but the left circulation is larger in size. The magnitude for phase -0.5π and 0.5π is also approximately halved compared to the contributions for phase 0 and π.

From these experiments it can be concluded that the density gradient can have a large effect on the residual flow profile, depending on the magnitude. Not only the M_0 component of the density gradient affects the advective contribution and the residual flow, also the amplitude of the M_2 component of the density gradient can affect flow caused by advection and the residual flow. The phase of the M_2 component seems to have little effect on the advective contribution to the flow and the total residual flow but only affects the contribution caused by the Coriolis deflection.

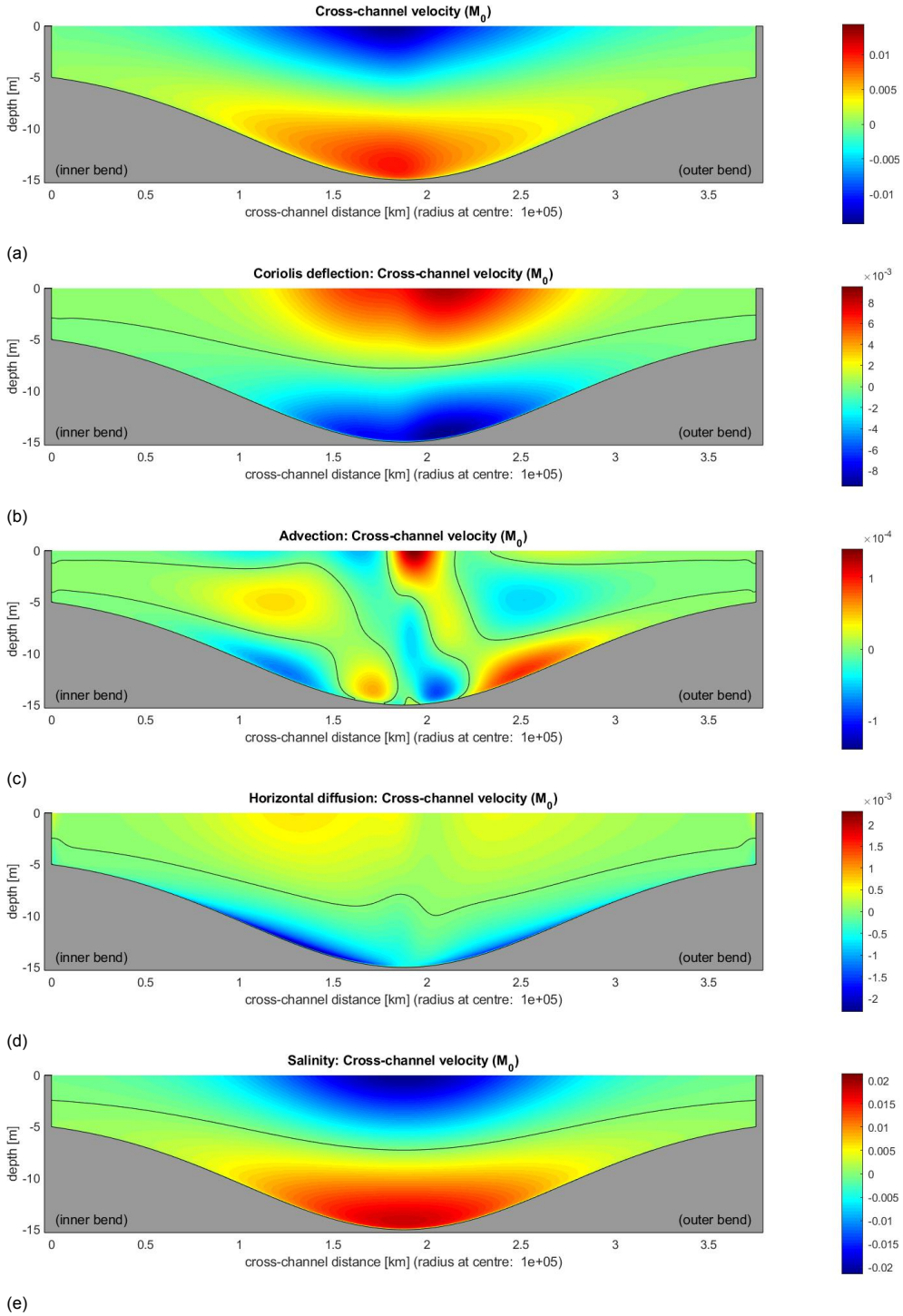

Figure 4.14: The results for the cross-channel flow in m/s for an M_0 density gradient of 10^{-4} and an M_2 density gradient with amplitude 10^{-4} and phase π. The panels show the total residual flow (a) and the decomposition of the flow into the contributions for Coriolis deflection (b), advection (c), horizontal diffusion (d) and the density gradient (e).

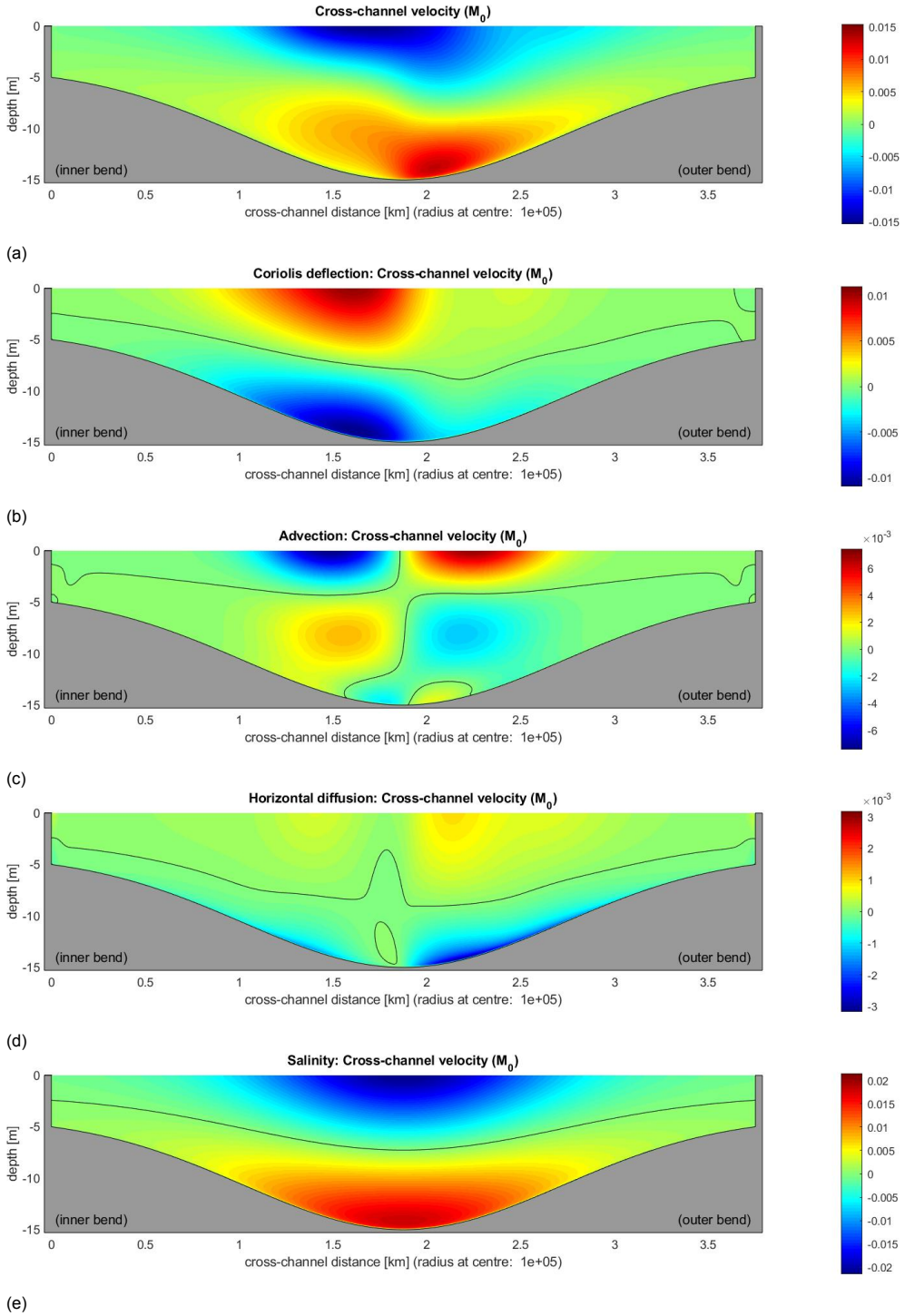

Figure 4.15: The results for the cross-channel flow in m/s for an M_0 density gradient of 10^{-4} and an M_2 density gradient with amplitude 10^{-3} and phase π. The panels show the total residual flow (a) and the decomposition of the flow into the contributions for Coriolis deflection (b), advection (c), horizontal diffusion (d) and the density gradient (e).

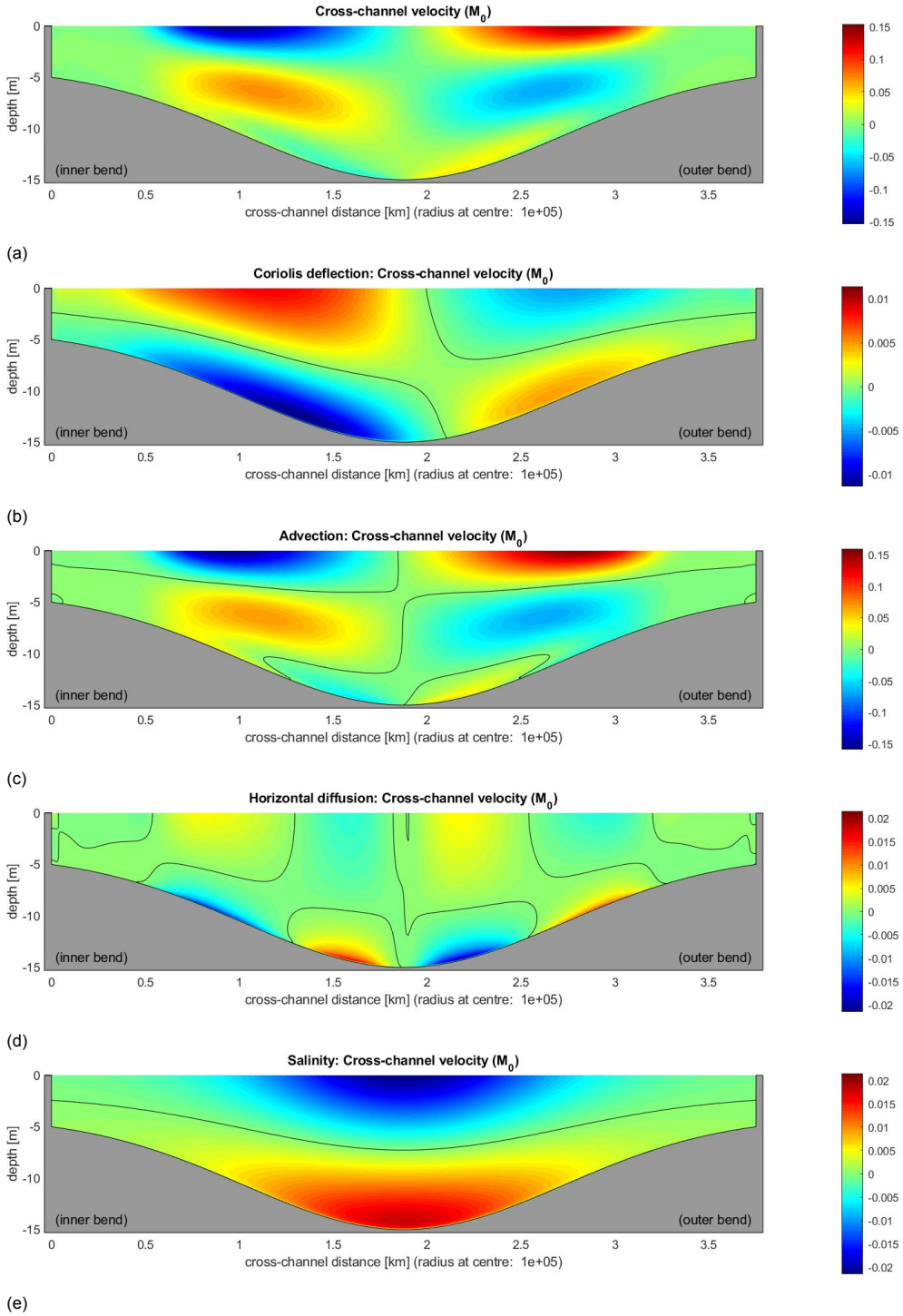

Figure 4.16: The results for the cross-channel flow in m/s for an M_0 density gradient of 10^{-4} and an M_2 density gradient with amplitude 10^{-2} and phase π. The panels show the total residual flow (a) and the decomposition of the flow into the contributions for Coriolis deflection (b), advection (c), horizontal diffusion (d) and the density gradient (e).

4.1.5. Simulation Ems

In the previous sections the flow is simulated for a theoretical estuary and some of the parameter values were varied to systematically investigate the effects of those parameters. In this section the measurements for the residual cross-channel velocity in [24] are compared to model results. The measurements were performed in the Ems estuary approximately at the mouth of the Knockster Tief on August 28 in 2018. By simulating the situation at that moment and location, the results of the model can be compared with the measurements in [24]

It is important to choose the correct parameter values to obtain model results similar to the measured results. Most of these values are found in [24]. The amplitude for the tidal discharge is computed from the measurements in [6]. The parameters used for these simulations are given in Table 4.2.

Table 4.2: The parameters values used for the simulation of the Ems.

Parameter	Symbol	Value	Unit
River discharge	$Q^{(0)}$	22	m^3/s
Amplitude of tidal discharge (M_2)	$Q^{(c)}$	18000	m^3/s
Phase of tidal discharge (M_2)	φ_Q	0	rad
Channel width	W	3000	m
Maximal water depth	H_{max}	11	m
Minimal water depth	H_{min}	1	m
Radius of curvature	R	-6000	m

The bottom profile of the actual estuary is quite complicated and only a smoothed bathymetry based on the observations is used in the simulations. A remarkable characteristic of the bathymetry is that the deepest point of the estuary is not situated in the middle of the estuary but on the left side when looking seaward. As a consequence, the bottom is very steep at the left side of the channel and more flat on the other side. To simulate this characteristic of the bathymetry, the deepest point of the Gaussian bottom profile is moved to 0.5km. To check if this affects the results, the simulations are also performed for a symmetric Gaussian bottom profile.

The simulations are performed without a density gradient, as the observed density gradient was close to zero most of the time and not identified as a large cause for the lateral circulations [24]. Wind is not included in the model, since the measurements were performed at a day with low wind speeds this should not affect the results a lot. The same eddy viscosity coefficients and shape function ϕ are used as in the reference situation.

The results for the simulations for the symmetric and asymmetric bottom profile, are shown in Figures 4.18 and 4.19, respectively. Note that the outer bend is on the left and the inner bend on the right corresponding to the negative radius of curvature. From these figures it follows that the cross-channel flow is mainly determined by the contribution caused by curvature. This was also identified as the main cause of lateral circulations in [24].

The profiles for the curvature (Figures 4.18e and 4.19e) do not vary much between the two different bottom profiles, in both simulations the curvature causes a counter-clockwise rotation. For the symmetric bottom profile (Figure 4.18e), the circulation cell is located in the middle of the channel and for the asymmetric bottom profile (Figure 4.19e), the circulation is located more to the left. Because the contribution caused by curvature is dominant, the total flow (Figures 4.18a and 4.19a) is also similar for the two bathymetries and consists of one counter-clockwise rotation.

When comparing the contributions caused by other mechanisms, it is visible that the bottom profile strongly influences those. The contribution caused by Coriolis deflection for the symmetric bottom (Figure 4.18b) can be characterised as three circulation cells. There is one clockwise circulation cell which is large in size and magnitude in the middle of the channel, a smaller counter-clockwise cell on the left and a very small cell on the right. The contribution caused by Coriolis deflection for the asymmetric bottom profile (Figure 4.19b) is similar except that between the cell in the centre and on the left two extra circulation cells have arisen.

The contribution due to advection for the symmetric bottom profile (Figure 4.18c) consists of five circulation cells and takes its maximum values in the centre of the estuary. For the asymmetric bottom profile (Figure 4.19c), still five circulation cells are present but they are shifted towards the left of the channel. The magnitude of the advective contribution to the cross-channel velocity is approximately doubled for the asymmetric bottom profile compared to the symmetric bottom profile. This confirms

the theory that a steeper bottom slope results in a higher magnitude for the cross-channel advective contribution.

The contribution caused by horizontal diffusion is symmetric for the symmetric bottom profile (Figure 4.18d). For the asymmetric bottom profile (Figure 4.19d) the contribution on the left is larger than on the right of the channel.

In [24] there were three measurement locations along the transect where the cross-channel velocity was measured. These locations would lie between 0.4 and 0.6 km in the simulated estuary. At the measurement locations an up-slope velocity was measured near the bottom and a down-slope velocity was measured higher in the water column. Only one of the measurement locations could measure until the water surface, the others did not provide measurement data for the upper part of the water column. At the location where the the whole water column was measured, the direction of the velocity was down-slope again near the surface. The magnitude of the cross-channel velocity was mostly between -0.03 and 0.03 m/s. The results for the measurements are depicted in Figure 4.17, which is reprinted from [24]. The right panel indicated as B shows the cross-channel velocity and is used to compare the model results with.

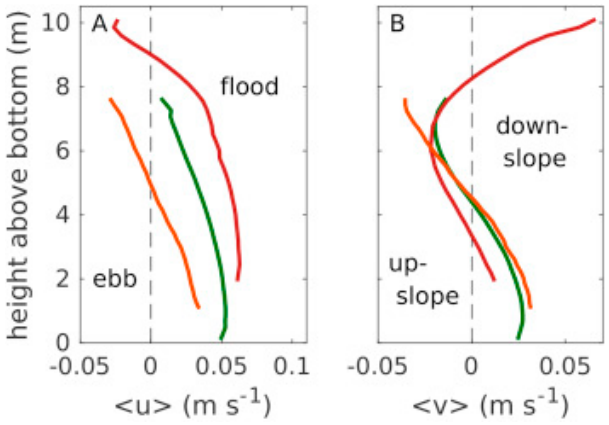

Figure 4.17: The results of the three measurement locations along the transect. It shows the along-channel residual velocity (panel A) and the cross-channel residual velocity (panel B). Reprinted from [24].

The measurements thus suggest there is a velocity to the right at the bottom of the water column, to the left in the middle of the water column and to the right again at the top, assuming the data from the single measurement location also holds for the other locations. When looking at Figure 4.19a, the magnitude of the velocity corresponds to the measurements. Moreover, a velocity to the right is visible at the bottom and higher in the water column a velocity to the left is observed. However, close to the surface, the velocity is still directed towards the right and a velocity to the left is not present near the surface in the simulations.

A possible explanation for the difference between the measurements and the simulations is the different description of the free surface. In the measurement data the velocities were computed using the method of [16]. This takes into account the variations in thickness of the water column over time. The column is thus divided into a number of sigma layers whose thickness increases or decreases depending on the surface variations. In the model the rigid lid approximation is used, which means the surface level is assumed constant and the layers do not have a varying thickness. The results in [16] show that a time dependent water depth can lead to differences in the velocity when averaged over time.

Of course there many more differences between the simulation and the actual situation such as the bottom profile, density gradient and wind. These differences could also cause a deviation between the measurements and the simulations. To be certain that the difference between the measured and computed velocities is caused by the rigid lid assumption, more research is required.

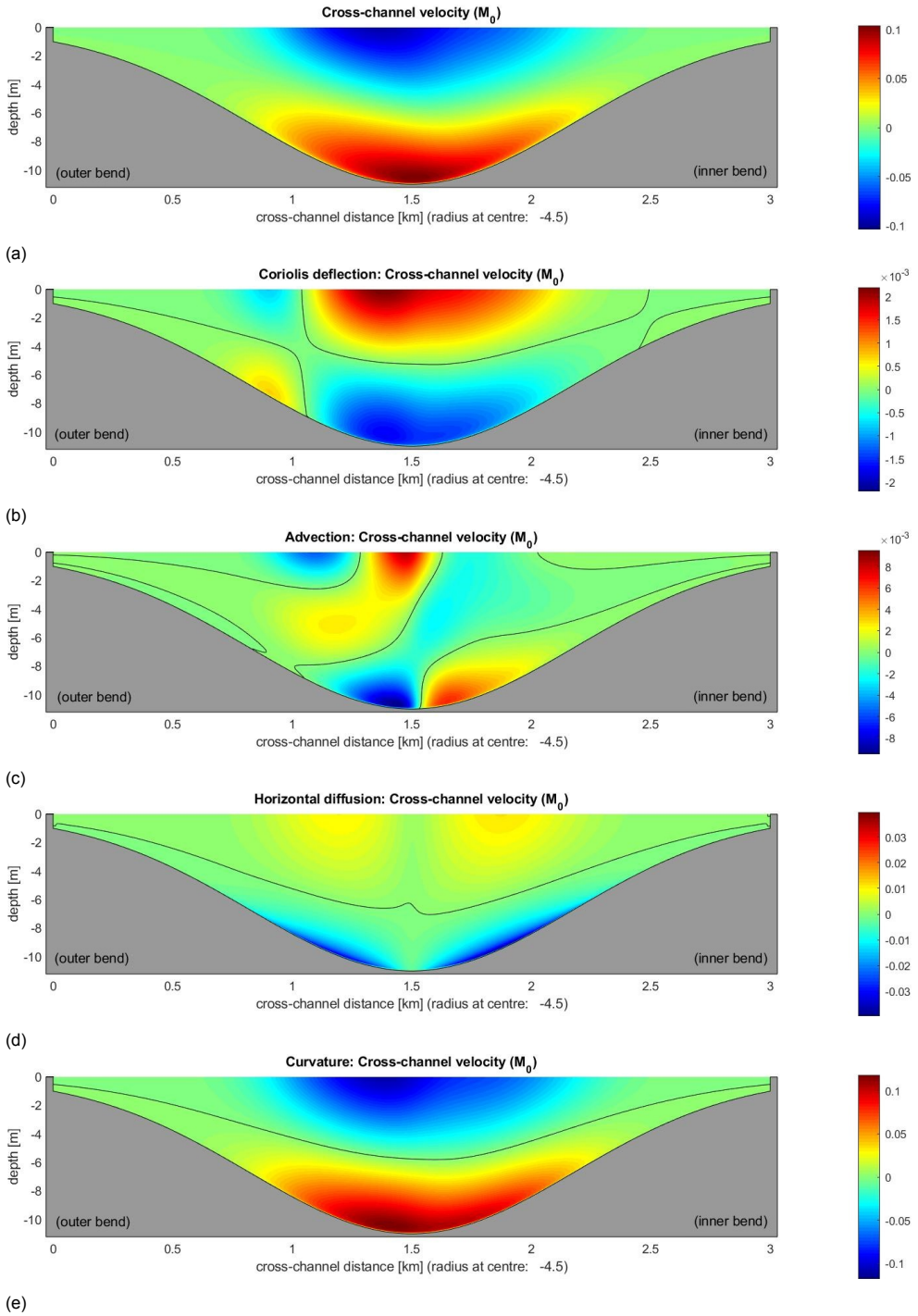

Figure 4.18: The results for the cross-channel flow in m/s for the simulation of the Ems with a bottom profile with its deepest point in the middle, at 1.5 km. The panels show the total residual flow (a) and the decomposition of the flow into the contributions for Coriolis deflection (b), advection (c), horizontal diffusion (d) and curvature (e).

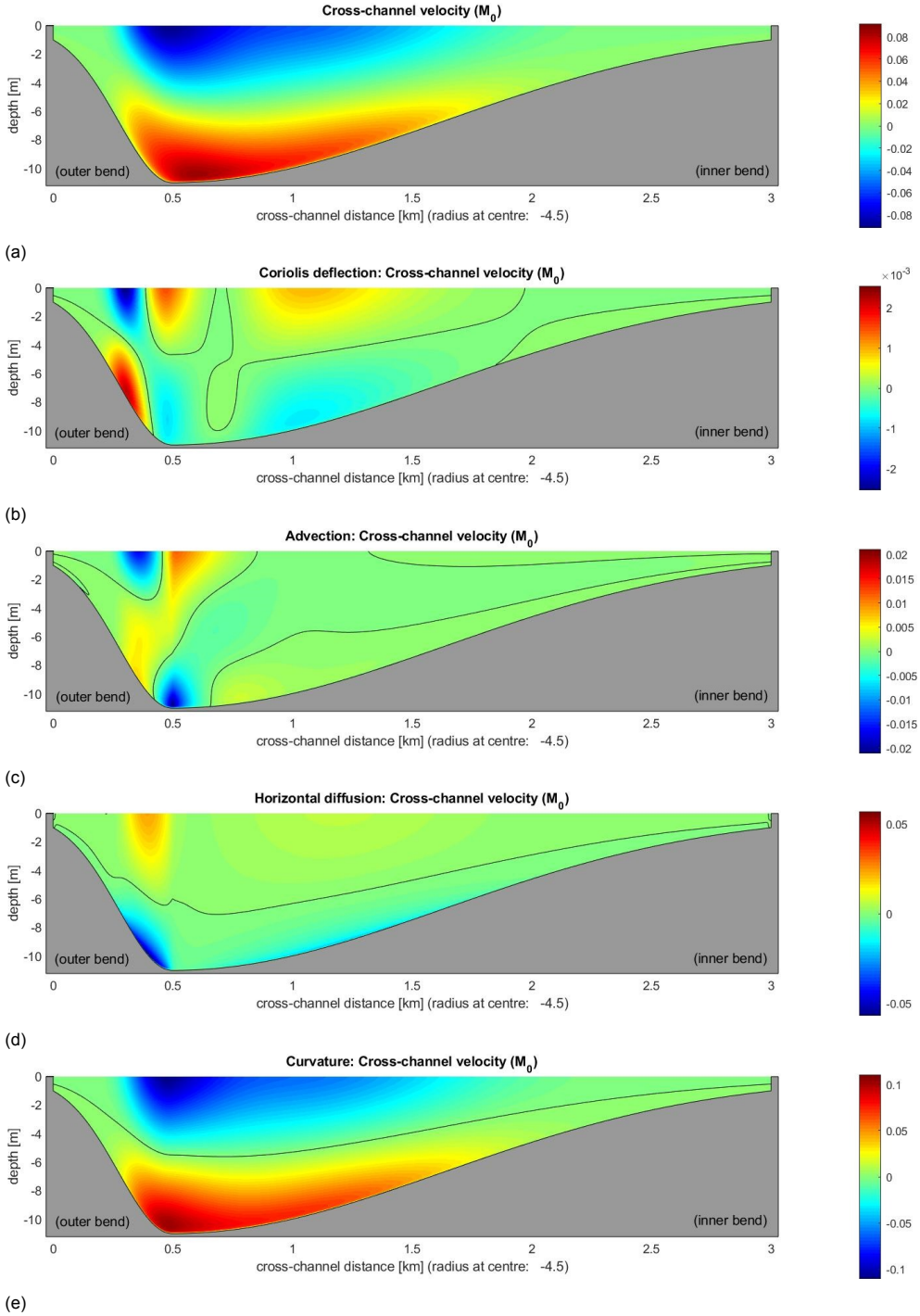

Figure 4.19: The results for the cross-channel flow in m/s for the simulation of the Ems with a bottom profile with its deepest point towards the left, at 0.5 km. The panels show the total residual flow (a) and the decomposition of the flow into the contributions for Coriolis deflection (b), advection (c), horizontal diffusion (d) and curvature (e).

4.2. Results for the suspended sediment

The main goal of this thesis is to implement a sediment extension to the model. In Chapter 2 and 3 the equations used to model the sediment dynamics and the solution methods were discussed. In this section the results obtained with the implemented sediment module are discussed. First, the results are given using a prescribed erosion coefficient. Next, the results are discussed with the erosion coefficient obtained in morphodynamic equilibrium.

For the computation of sediment it is required to assign values to some sediment specific parameters. For the simulations in this section, the values in Table 4.3 are used, unless stated otherwise. For the situations that are simulated, most parameters for the flow are chosen equal to those in the reference situation (see Table 4.1). Regardless the bottom profile, all channels have a width of 3.75 km and are assumed to be straight. The magnitude of the diffusivity and viscosity constants is equal to the those in the reference situation, but the shape function ϕ is now chosen to be constant over depth.

Parameter	Symbol	Value	Unit
Horizontal diffusivity coefficient	D_h	1	m^2/s
Vertical diffusivity coefficient	D_v	0.006	m^2/s
Sediment fall velocity	w_s	3×10^{-4}	m/s
Density of sediment	ρ_s	2650	kg/m^3
Grain diameter	D_s	2×10^{-5}	m
Reference value for $a(r)$	a_*	4×10^{-6}	-

Table 4.3: The values for the parameters for sediment.

In this chapter only the results for the tidally averaged suspended sediment concentration are provided because these are the most intuitive to understand. However, the model also produces the M_2 and M_4 tidal components of the suspended sediment concentration.

4.2.1. Prescribed erosion coefficient

To check if the model behaves as expected, first a situation with a known solution is simulated. The most simple situation to simulate is that of a cross-section with a flat bottom profile and no cross-channel flow. This requires the flow to be computed without the effect of Coriolis deflection, curvature, advection and a density gradient. Hence only diffusion and discharge affect the flow. As a consequence, the flow in the cross-channel direction is zero and in the along-channel direction the flow profile of Figure 4.20 is obtained. This result is used in the model to compute the suspended sediment distribution. In this case there is no advection of sediment and diffusion is assumed negligible, then the concentration equation (2.12), can be solved analytically and the solution reads,

$$c = \frac{f(r)}{w_s} \exp\left(-\frac{w_s}{D_v}(z+H)\right), \tag{4.1}$$

for every r, with

$$f(r) = \frac{w_s \rho_s}{\rho_0 g' D_s} |\tau_b| a(r). \tag{4.2}$$

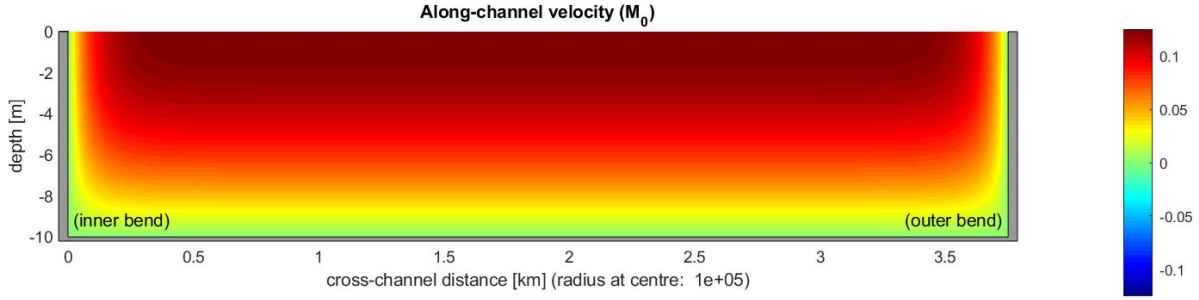

Figure 4.20: The result for the along-channel flow in m/s for a rectangular bottom profile when only discharge is included.

The flow profile creates a bed shear stress which is constant in the middle of the channel and quickly goes to zero near the boundaries. With a constant erosion coefficient equal to a_*, the function describing the bottom boundary condition, $f(r)$ in equation (4.1), will have the same shape as $|\tau_b|$. In Figure 4.21 the value of $f(r)$ is plotted against the channel width. Since the computed suspended sediment concentration approximates the analytical solution, this shape should also be visible in the suspended sediment distribution.

Figure 4.22, shows the M_0 component of the suspended sediment concentration. One can recognise the dependency of f on r in the sediment profile. Moreover, at different points along the transect the value for c over the depth was compared with the analytical solution and these were approximately equivalent.

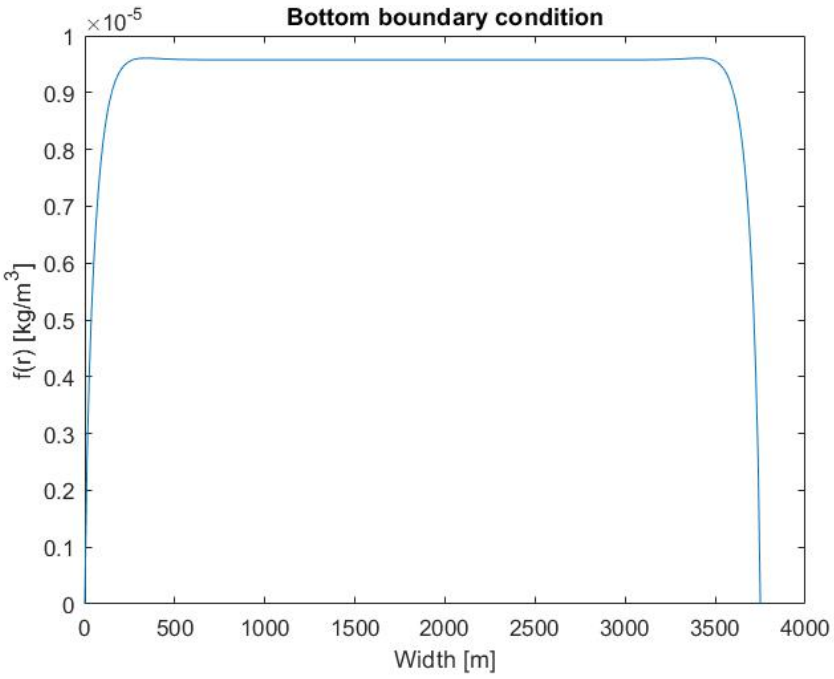

Figure 4.21: The function $f(r)$ plotted against the channel width for the rectangular bottom profile and constant erosion coefficient.

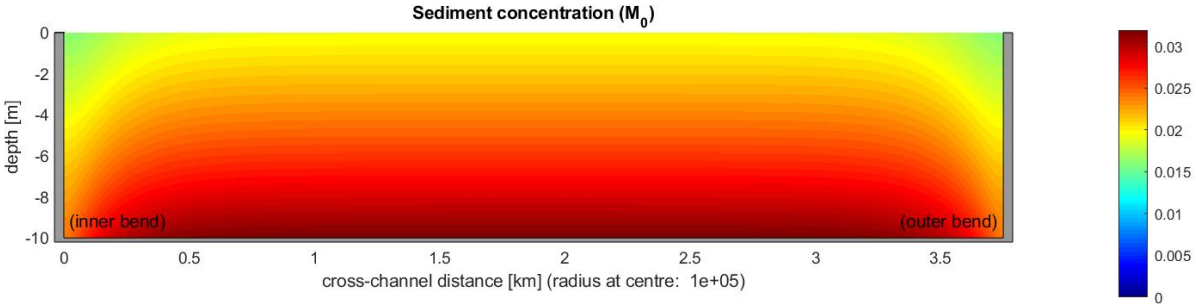

Figure 4.22: The result for the M_0 component of the suspended sediment concentration in kg/m^3 for the rectangular bottom profile and constant erosion coefficient.

To test a slightly more complicated situation, in the next experiments $a(r)$ is defined to linearly increase from $0.5a_*$ to $1.5a_*$, with a_* the reference value for the erosion coefficient. With the same flow, this results in a different dependency of f on the radial coordinate, see Figure 4.23. The function $f(r)$ is now linearly increasing in most part of the channel. As a consequence, the concentration also increases over the width of the channel. In Figure 4.24 the M_0 component of the suspended sediment concentration is depicted. Indeed the concentration is low on the left side of the channel and gets higher when looking more to the right side of the channel.

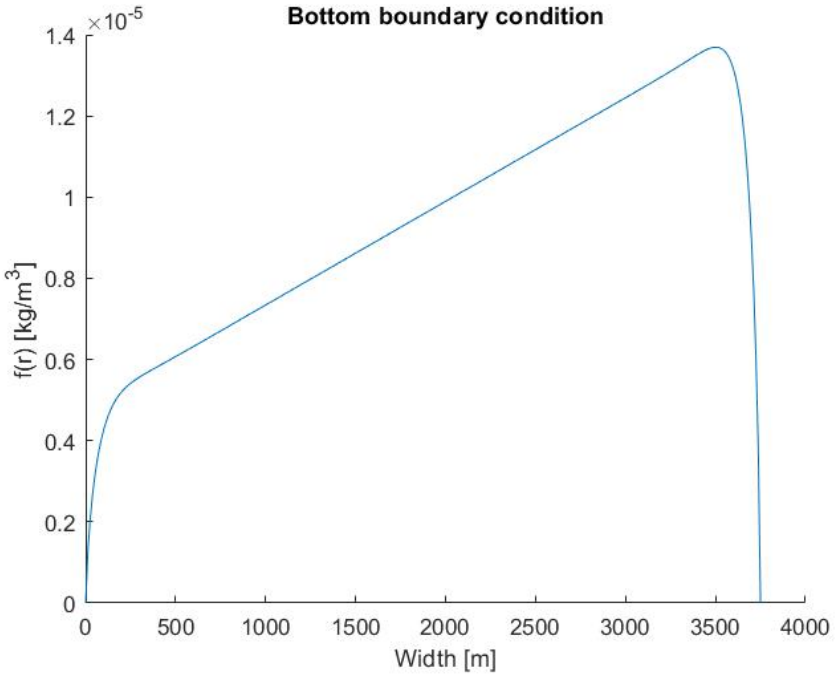

Figure 4.23: The function $f(r)$ plotted against the channel width for the rectangular bottom profile and linearly increasing erosion coefficient.

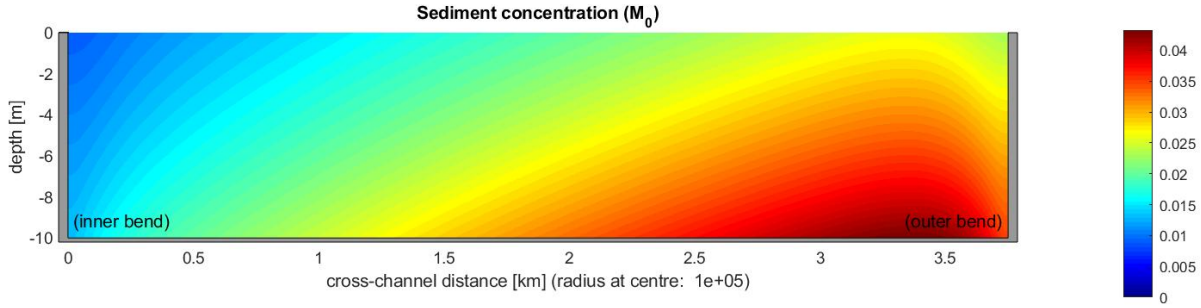

Figure 4.24: The result for the M_0 component of the suspended sediment concentration in kg/m^3 for the rectangular bottom profile and linearly increasing erosion coefficient.

To further test the sediment module, other bottom profiles are used. A different bottom profile causes a different along-channel flow and therefore a different shape of $f(r)$. For a varying bottom profile, the analytical solution given in equation (4.1), is not a good approximation anymore because H is now also a function of r.

The model is tested for both a linearly shaped bottom profile and a Gaussian profile. The same linearly increasing erosion coefficient is used as in the previous experiment. Since the bottom boundary condition strongly affects the suspended sediment distribution, the function $f(r)$ dictates the suspended sediment concentration to a large extend. The shape of $f(r)$ is depicted in Figure 4.25 for the linear bottom profile and in Figure 4.27 for the Gaussian bottom profile. The M_0 component of the suspended sediment concentration is shown in Figure 4.26 for the linear bottom profile and in Figure 4.28 for the Gaussian bottom profile.

For the linearly increasing bottom profile, the function $f(r)$ (Figure 4.25) has a similar shape as for the flat bottom profile (Figure 4.23) but with a steeper slope. This is visible in the profile for c (Figure 4.26) as well because the maximum magnitude of the suspended sediment concentration is almost doubled compared with the simulation for the flat bottom (Figure 4.24). For the Gaussian bottom profile, $f(r)$ is not constantly sloping anymore in most of the cross-section (Figure 4.27) but has a more complex dependency on the radial coordinate. This behaviour is also visible in the profile for the concentration (Figure 4.28).

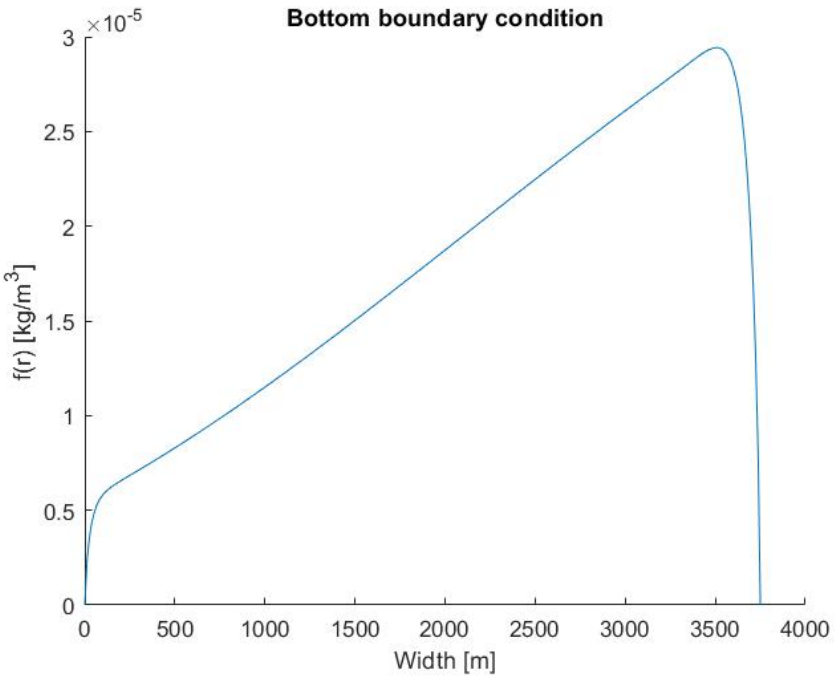

Figure 4.25: The function $f(r)$ plotted against the channel width for the linearly decreasing bottom profile and the linearly increasing erosion coefficient.

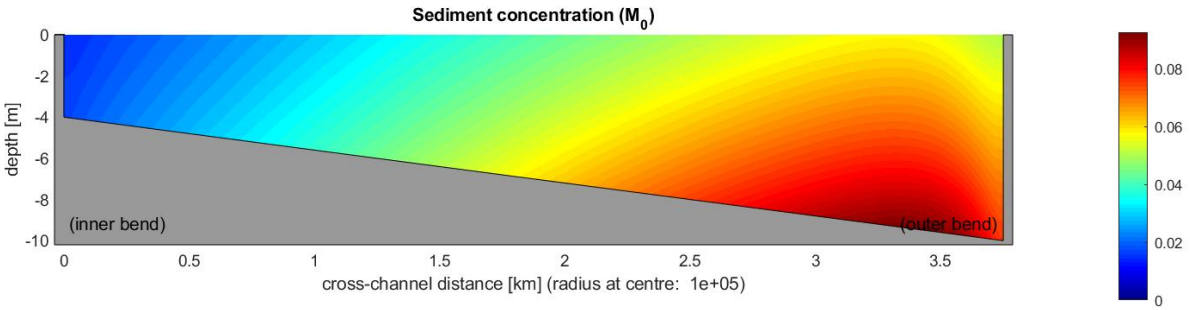

Figure 4.26: The result for the M_0 component of the suspended sediment concentration in kg/m^3 for the linearly decreasing bottom profile and linearly increasing erosion coefficient.

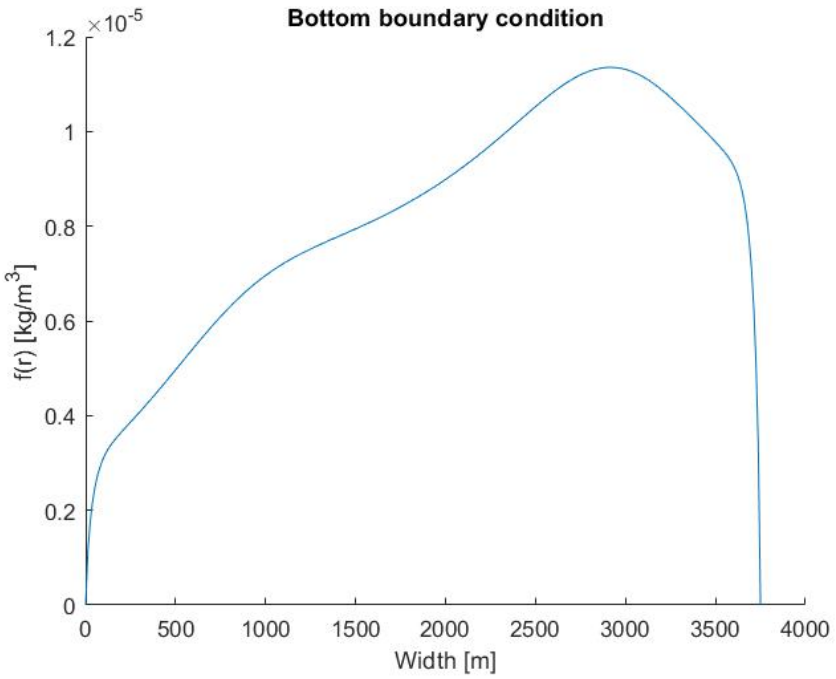

Figure 4.27: The function $f(r)$ plotted against the channel width for the Gaussian decreasing bottom profile and the linearly increasing erosion coefficient.

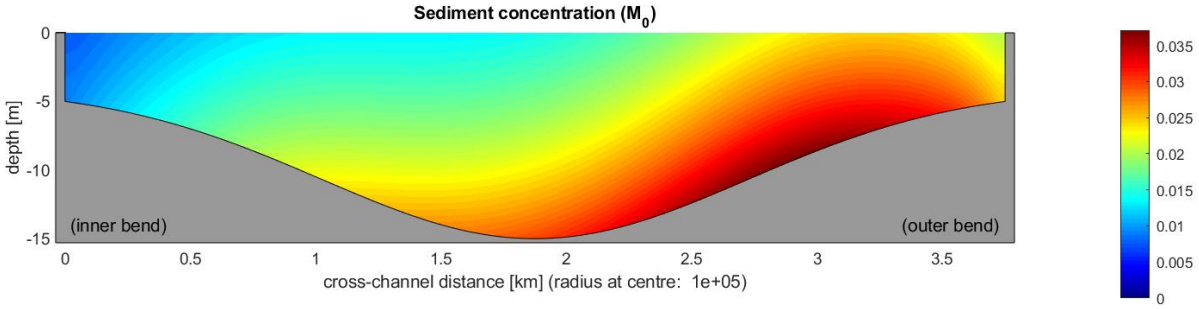

Figure 4.28: The result for the M_0 component of the suspended sediment concentration in kg/m^3 for the Gaussian bottom profile and linearly increasing erosion coefficient.

Last, the sediment module was tried for a Gaussian bottom profile including a cross-channel flow. In the previous simulations the suspended sediment concentration was only affected by diffusive transport, now advective transport also contributes to the distribution of sediment. The flow for this simulation is determined by Coriolis deflection, diffusion and discharge, the other mechanisms are not included in the computation of the flow. As a result the cross-channel flow has a clockwise circulation. The expectation is that the cross-channel flow affects the distribution of sediment. The different flow profile also affects the bed shear stress and this results in a different shape for $f(r)$. A constant erosion coefficient is used, to clearly see the effect of the cross-channel flow on the suspended sediment concentration.

Figure 4.29 shows the function $f(r)$ plotted against the channel width for this situation and Figure 4.30 shows the corresponding suspended sediment distribution. Even though the function $f(r)$ is symmetric, the suspended sediment concentration is not symmetrically distributed. On the left of the channel the concentration is higher than on the right of the channel. This difference is caused by the cross-channel flow which moved the water close to the bed with a high suspended sediment concentration to the left and the water near the surface, which has a a lower suspended sediment concentration, towards the right of the channel.

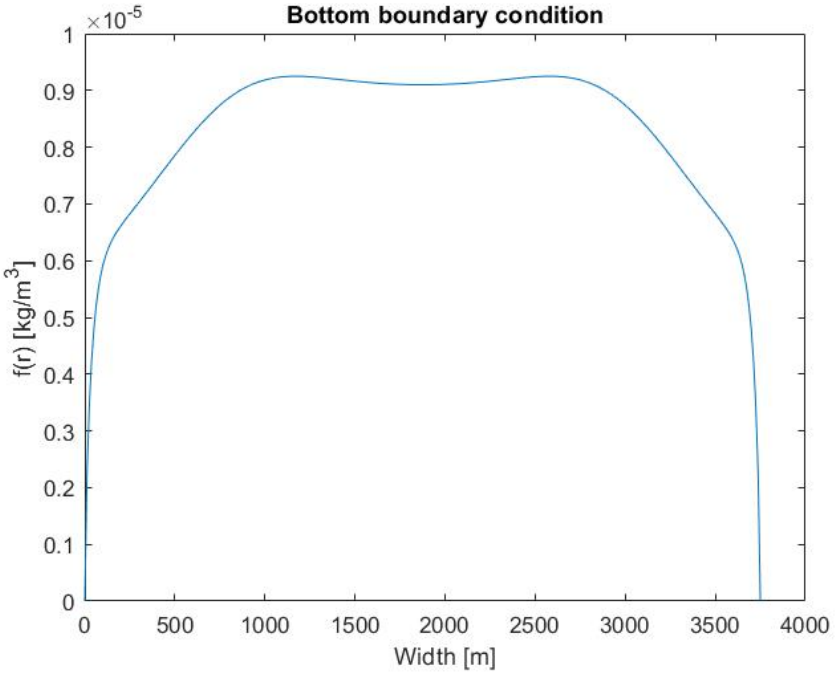

Figure 4.29: The result for the M_0 component of the suspended sediment concentration in kg/m^3 for the rectangular bottom profile, constant erosion coefficient and a flow affected by Coriolis deflection.

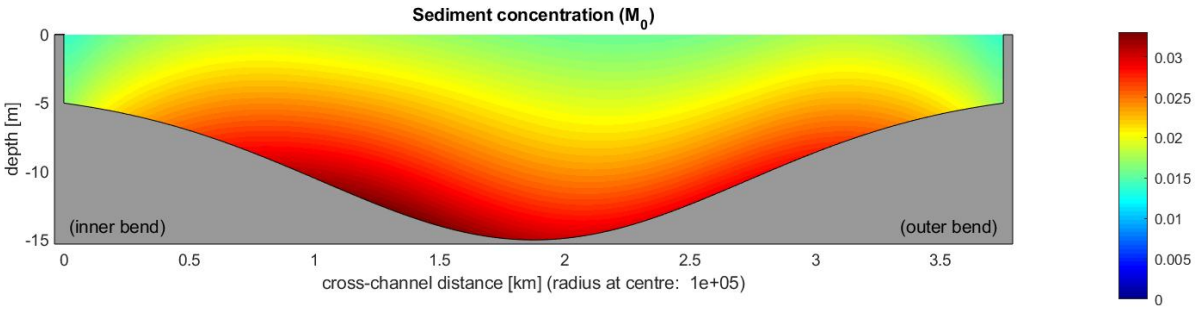

Figure 4.30: The function $f(r)$ plotted against the channel width for the Gaussian decreasing bottom profile, the constant erosion coefficient and a flow affected by Coriolis deflection.

4.2.2. Computed erosion coefficient

In morphodynamic equilibrium the spatial distribution of the erosion coefficient cannot be chosen freely but a specific distribution is required (see Section 3.7). In this section these distributions in morphodynamic equilibrium are shown for situations with diffusive transport only. Again the model was first applied to a simple situation with a known solution. For a cross-section with a flat bottom and only an along-channel flow (i.e. no cross-channel flow), the lateral sediment transport only has a diffusive contribution. The analytical solution for c (see equation (4.1)), can then be used to obtain

$$T_{tot} = -\frac{D_h}{w_s}\frac{\partial f(r)}{\partial r}\int_{-H}^{0}\exp\left(-\frac{w_s}{D_v}(z+H)\right)\mathrm{d}z = \frac{\partial f(r)}{\partial r}\left[\frac{D_h}{w_s^2}\left(\exp\left(-\frac{w_s}{D_v}H\right)-1\right)\right]. \tag{4.3}$$

The total transport must be zero in morphodynamic equilibrium. Since the term in the square brackets is not equal to zero, it can be concluded that the derivative of $f(r)$ with respect to r must be zero. Consequently the expression for $f(r)$ must be constant and $a(r)$ can be solved up to a multiplication constant $C1$, as

$$a(r) = C_1\frac{\rho_0 g' D_s}{w_s \rho_s |\tau_b|}. \tag{4.4}$$

The value of $C1$ depends on the reference value for the erosion coefficient a_*.

To run the model, an initial solution for $a(r)$ must be assigned. Here a constant value equal to the reference value a_* is chosen as initial guess. The other parameters are again equal to the values in Table 4.3. In Figure 4.32, the erosion coefficient obtained after 500 iterations with time step $\Delta t = 10$ s is plotted. In the same figure the analytical solution is also indicated. To investigate the convergence of the computation, δ_i is plotted on a semi-log scale in Figure 4.33. The suspended sediment concentration corresponding to the computed value for $a(r)$ is shown in Figure 4.31.

In Figure 4.32, the markers for the analytical solution of the erosion coefficient are located on the curve for the computed solution. This shows the model is able to accurately approximate the erosion coefficient in morphodynamic equilibrium.

Because the transport is only determined by diffusion, the depth integrated derivative of c with respect to r must be zero. As a consequence the derivative of c with respect to r must be constant. At the boundaries this derivative must be zero, therefore the derivative of c with respect to r must be zero over the whole transect. This is visible in Figure 4.31: in the lateral direction the concentration at any height is constant.

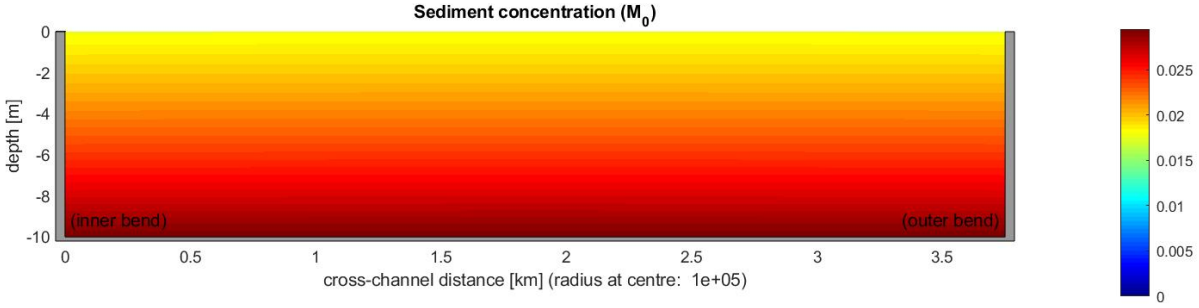

Figure 4.31: The result for the M_0 component of the suspended sediment concentration in kg/m^3 in morphodynamic equilibrium for a rectangular bottom profile.

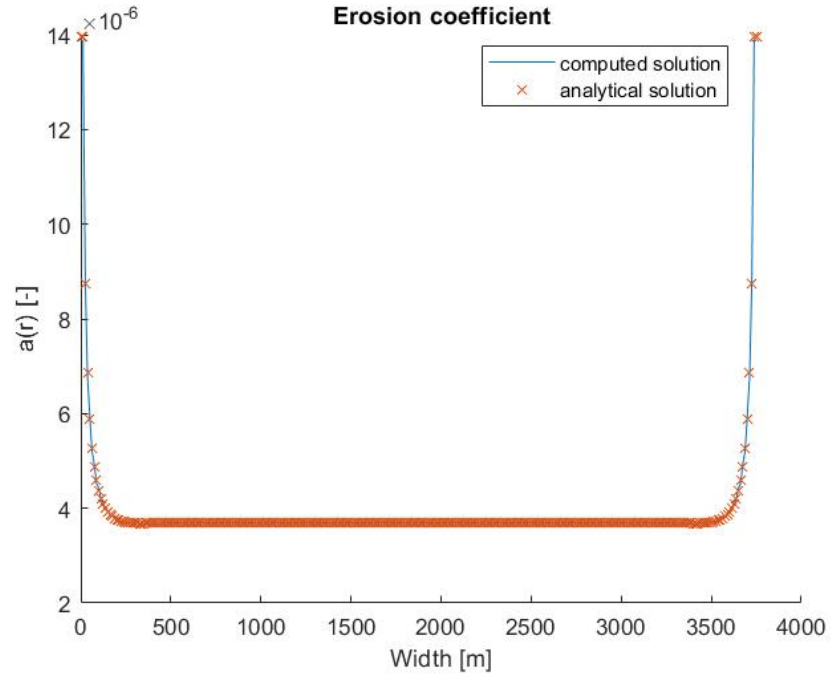

Figure 4.32: The erosion coefficient in morphodynamic equilibrium for a rectangular bottom profile plotted against the channel width.

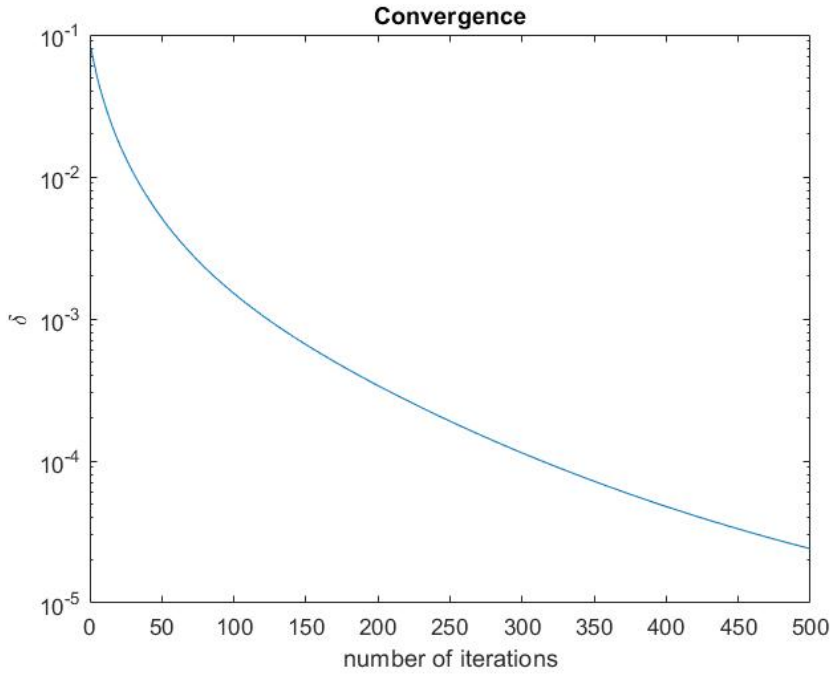

Figure 4.33: The convergence of the computation of the erosion coefficient for a rectangular bottom profile, showing δ_i plotted against the number of iterations.

Next, the erosion coefficients in morphodynamic equilibrium for slightly more complicated bottom profiles are computed. The linearly decreasing bottom profile and the Gaussian bottom profile, described in Section 4.2.1, are used again. For these bathymetries a different erosion coefficient is expected but the corresponding concentration should still be constant in the horizontal direction.

Again 500 iterations are performed with a step size $\Delta t = 10$ s and a constant erosion coefficient as initial guess. Figures 4.34 - 4.39 show the M_0 component of the suspended sediment concentration,

the computed erosion coefficient and the convergence for the two bathymetries.

For the linearly decreasing bottom, the erosion coefficient in Figure 4.35 differs slightly from the coefficient for the flat bottom in Figure 4.32. For the flat bottom profile $a(r)$ is symmetric and straight in the middle of the channel, for the linear bottom profile $a(r)$ is not symmetric. On the left of the channel $a(r)$ is higher than on the right but the maximum value at the boundary is lower than the maximum value at the right boundary. Figure 4.34 shows that this erosion coefficient indeed results in a constant concentration over a line of constant depth.

Figure 4.38 shows the erosion coefficient in morphodynamic equilibrium when considering a Gaussian bottom profile. The erosion coefficient is symmetric with a local maximum in the middle of the estuary and minima approximately 750 metres from both of the side walls. Figure 4.37 shows the corresponding suspended sediment concentration, again the concentration is constant in the horizontal direction.

Figures 4.36 and 4.39 show the convergence for the linear and Gaussian bottom profile, respectively. It is remarkable that for these bottom profiles the convergence is slightly faster than the convergence for the rectangular bottom profile. A possible explanation for this is that the diffusive transport is larger for a more varying bottom profile and this leads to faster convergence.

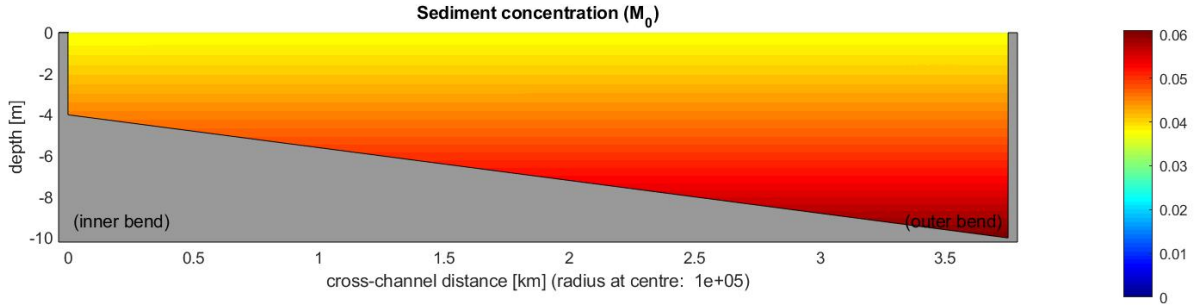

Figure 4.34: The result for the M_0 component of the suspended sediment concentration in kg/m^3 in morphodynamic equilibrium for a linearly decreasing bottom profile.

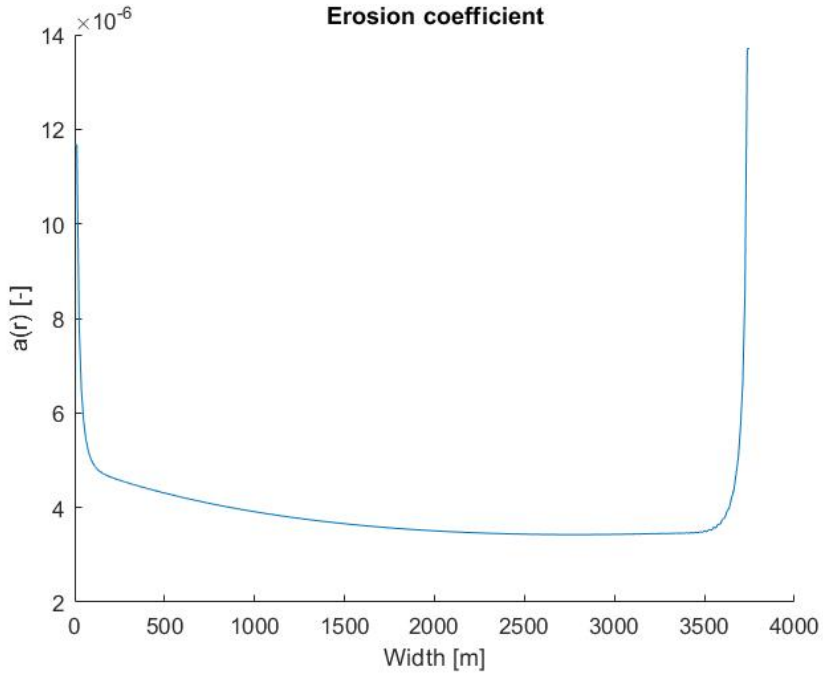

Figure 4.35: The erosion coefficient in morphodynamic equilibrium for a linearly decreasing bottom profile plotted against the channel width.

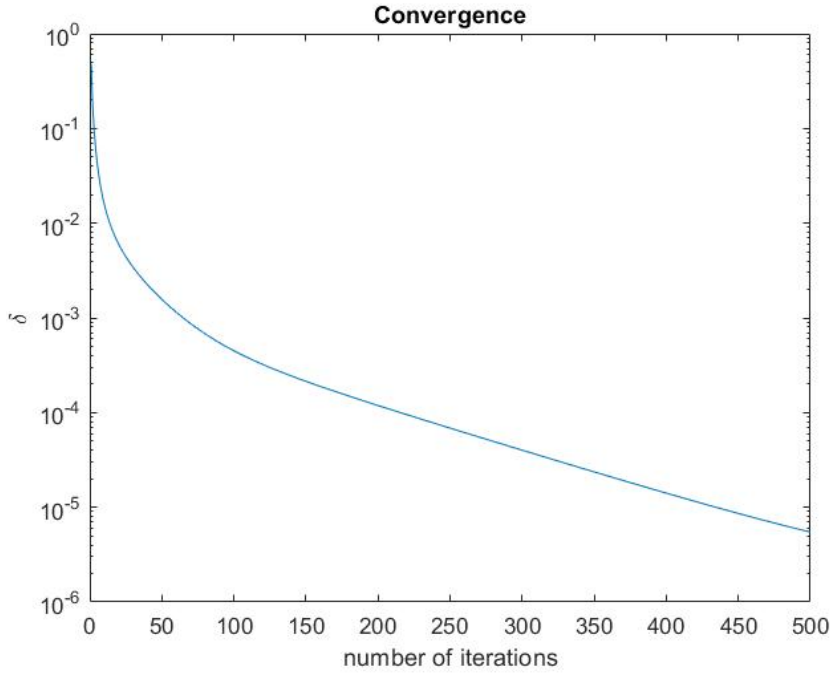

Figure 4.36: The convergence of the computation of the erosion coefficient for a linearly decreasing bottom profile, showing δ_i plotted against the number of iterations.

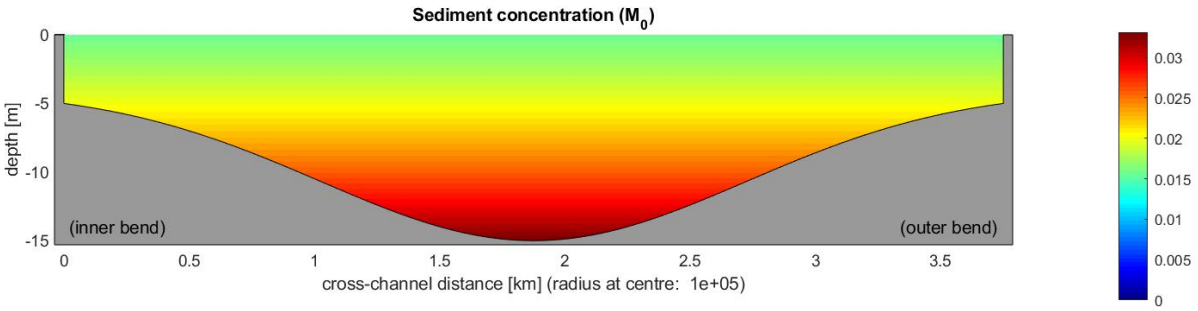

Figure 4.37: The result for the M_0 component of the suspended sediment concentration in kg/m^3 in morphodynamic equilibrium for a Gaussian bottom profile.

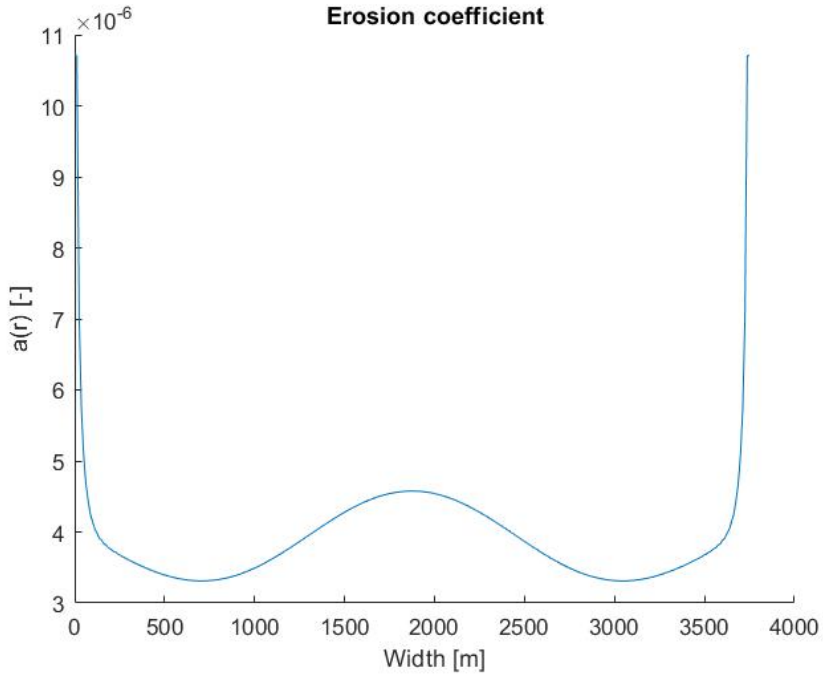

Figure 4.38: The erosion coefficient in morphodynamic equilibrium for a Gaussian bottom profile plotted against the channel width.

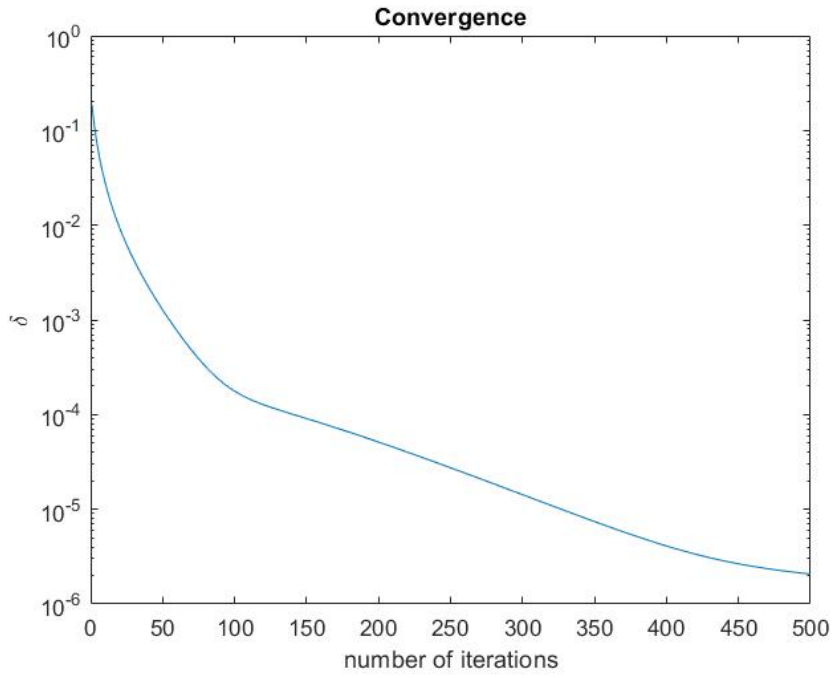

Figure 4.39: The convergence of the computation of the erosion coefficient for a Gaussian bottom profile, showing δ_i plotted against the number of iterations.

5

Conclusions and recommendations

This chapter consists of two parts. In Section 5.1 the conclusions of this project are summarised by systematically answering the research questions posed in Section 1.3. In Section 5.2 some suggestions for further research are provided.

5.1. Conclusions

The first research question concerns the effect of the bottom slope on the advective contribution to the residual cross-channel flow. The results in Section 4.1.2 show that the channel width, and thus the bottom slope, strongly affects the magnitude of the advective forcing. For a steep bottom slope, in this case the slope corresponding to a narrow channel with a Gaussian bottom profile, the contribution caused by advection is large. For a gradual bottom profile, in this case corresponding to a wide channel with a Gaussian bottom profile, advection can be assumed negligible. The characteristic flow patterns resulting from the advective contribution are not significantly affected by the bottom slope. This is also observed in the results in Section 4.1.5 where a specific cross-section of the Ems is simulated. In the cross-section with an asymmetric bottom profile, the contribution caused by advection is large above the steep part of the bottom and small above the area where the bottom changes are gradual. The number of circulation cells did not change between simulations with the symmetric and asymmetric bottom profile.

To answer the second research question, the effect of curvature on the advective contribution to the flow is studied. The results for these simulations are presented in Section 4.1.3. The results show that curvature strongly affects the total cross-channel flow, depending on the magnitude of the radius of curvature. A smaller radius of curvature results in a stronger contribution caused by curvature. When looking seaward, a positive radius of curvature results in a clockwise circulation and a negative radius of curvature leads to a counter-clockwise circulation. The contribution of advection is only slightly affected by the channel curvature in these simulations with the magnitude increasing as the radius of curvature decreased. However, the contribution due to advection did not become the dominant process because the contribution resulting from curvature increased as well, such that the latter contribution dominated the former one. For a very small radius of 1 km, some circulation cells in the contribution caused by advection are reversed compared to the results for larger radii of curvature.

Section 4.1.4 contains the results to answer the third question regarding the effect of a lateral density gradient on the cross-channel flow caused by advection. The results show that the density gradient can have a large effect on the residual flow profile, depending on the magnitude of this gradient. Especially the amplitude of the M_2 tidal component of the density gradient affects the flow caused by advection. For an increasing amplitude of the M_2 component of the density gradient the contribution caused by advection increased in magnitude and the characteristics of the profile changed. For a large enough amplitude the advective contribution becomes the dominant process and determines the lateral tidally averaged flow. Once the advective contribution has a significant effect on the lateral flow, this also affects the other contributions to the flow. The phase of the M_2 component has little effect on the residual flow and the advective contribution to the flow in the experiments performed. The phase seems to mainly affect the contribution caused by the Coriolis deflection.

The fourth question that was raised concerned the ability of the model to reproduce measurement data of a cross-section of the Ems. In Section 4.1.5 the results for the simulation of a cross-section of the Ems are presented. The cross-channel flow computed by the model had the same magnitude as the measured flow. Moreover, the direction of the flow near the bottom and in the middle of the water column are similar. However, the direction in the upper part of the water column is to the right in the measurements but to the left in the simulations. A possible explanation for the difference between the measurements and simulation is the different description of the free surface. In the measurements the time-varying thickness of the water column is taken into account whereas the model uses the rigid lid assumption, this could lead to a discrepancy between the measurements and model results. There are also other differences between the simulation and the actual situation, such as bathymetric details, presence of density gradients and effect of the wind. Potentially, these differences contribute as well to the deviation between the measurements and model results.

The last two research questions cover the developed sediment module. The functioning for a prescribed density gradient is investigated in Section 4.2.1. Based on these results the sediment module seems to works as expected for a prescribed erosion coefficient. For the simplest situation the analytical solution is approximated. For more complicated situations, such as a varying bottom profile and a non-zero cross-channel velocity, the results agree with physical intuition.

The ability of the sediment module to compute the erosion coefficient in morphodynamic equilibrium for only diffusive sediment transport is investigated in Section 4.2.2. Those results show that the model seems to work properly. The analytical solution is approximated for the simplest situation and for more complicated bathymetries the results also match the expectations.

5.2. Recommendations

The effect of several parameters on the cross-channel residual flow and advective contribution to the flow is investigated. Recommended further research on this topic would be to study the effect of other parameters and to include other processes in the model. Interesting extensions could be for example to include wind shear stress or to investigate the effect of a time-dependent vertical viscosity coefficient.

The results for the simulation of a cross-section in the Ems showed that the model is not able to exactly reproduce measurements. It is recommended to investigate what the cause of the difference between measurement data and model results is. Moreover, it would be interesting to examine if measurements in other estuaries can be reproduced by the model.

It is concluded that the module for sediment works as expected for a prescribed erosion coefficient and for computing the erosion coefficient in morphodynamic equilibrium for diffusive transport only. A comment on this conclusion is that only a limited number of simulations is executed for the sediment module during this project. To support the conclusions more strongly, it is recommended to perform more experiments with the sediment module to see if it also works for different situations that were not simulated yet. The model is for example not yet tested with spatially varying vertical viscosity and diffusivity coefficients or for more complicated bottom profiles.

The current model can compute the erosion coefficient in morphodynamic equilibrium for situations with diffusive sediment transport only. The next step would be to develop a model that is also able to handle situations with both advective and diffusive transport of sediment. Experiments were performed with the current model for situations including advective transport of sediment, so including a flow with a non-zero cross-channel velocity. Unfortunately, the model did not converge for the cases that were tested up to now. Further research is necessary to find out why the model did not converge for these situations and how the model can be altered to obtain a solution for situations with advective transport. A model which also works for advective sediment transport could be obtained by extending the current model and thus by using the time integration method. However, it is also possible to further investigate the other methods that were tested for the sediment model, described in Appendix H. Possibly, once the methods described in Section H.1 and H.3 work, they can also handle advective transport.

Another reason to develop the methods described in Appendix H is because the current sediment module is computationally expensive. The computation time depends on the desired convergence and thus the number of iterations but is much larger than the time required for a more direct solution method with the same accuracy. The methods in Appendix H are expected to be faster than the current method, therefore it is recommended to investigate these methods further to find out if those can be changed such that they compute the correct erosion coefficient. Those improvements could lead to a faster

model without reducing the accuracy.

Once the model is able to compute the erosion coefficient in morphodynamic equilibrium for a situation with both advective and diffusive transport of suspended sediment, it would be interesting to investigate if the model can reproduce measurement data of suspended sediment concentrations in actual estuaries. This way it can be verified if the model only works for theoretical situations due to simplifications or if the model can be used to simulate the sediment distribution of actual estuaries. With the current sediment module, this verification is not possible because the model cannot compute the erosion coefficient in morphodynamic equilibrium when there is advective transport of sediment. In real life it is unlikely to have an estuary without a cross-channel flow and thus without advective transport.

A

Derivation of the shallow water equations

In this appendix the shallow water equations are derived from the Navier-Stokes equations and the continuity equation. The content of this chapter is largely following the approach taken in Chapter 2 of [30].

A.1. Continuity and Navier-Stokes equations

The continuity equation describes the conservation of mass and is expressed as

$$\frac{\partial \rho}{\partial t} + \frac{\partial \rho u}{\partial x} + \frac{\partial \rho v}{\partial y} + \frac{\partial \rho w}{\partial z} = 0. \tag{A.1}$$

When a fluid is incompressible, this means the density does not change due to variations in the pressure [1]. This is not equivalent to having a constant density, the density can still vary due to changes in salinity or temperature. Assuming water to be an incompressible fluid, the density can be assumed to depend only on the temperature T and salinity S,

$$\frac{d\rho}{dt} = \frac{\partial \rho}{\partial T}\frac{dT}{dt} + \frac{\partial \rho}{\partial S}\frac{dS}{dt}. \tag{A.2}$$

Heat and salinity each have their own balances, more information about the equations for heat and salinity can be found in sections 4.3 and 4.4 in [9]. Typically, the diffusion can be assumed negligible compared to advection, as explained in [1]. When disregarding diffusion and assuming there are no sources or sinks, the rate of change of the density can be expressed as

$$\frac{d\rho}{dt} = \frac{\partial \rho}{\partial t} + u\frac{\partial \rho}{\partial x} + v\frac{\partial \rho}{\partial y} + w\frac{\partial \rho}{\partial z} = \frac{\partial \rho}{\partial T}\frac{dT}{dt} + \frac{\partial \rho}{\partial S}\frac{dS}{dt} = 0. \tag{A.3}$$

Using this equation, the conservation of mass, equation (A.1), can be expressed as

$$\frac{\partial u}{\partial x} + \frac{\partial v}{\partial y} + \frac{\partial w}{\partial z} = 0. \tag{A.4}$$

The Navier-Stokes equations describe the conservation of momentum. The conservation of momentum in Cartesian coordinates can be stated as,

$$\frac{\partial \rho u}{\partial t} + \frac{\partial \rho u^2}{\partial x} + \frac{\partial \rho uv}{\partial y} + \frac{\partial \rho uw}{\partial z} - \rho\gamma v + \frac{\partial p}{\partial x} - \frac{\partial \tau_{xx}}{\partial x} - \frac{\partial \tau_{xy}}{\partial y} - \frac{\partial \tau_{xz}}{\partial z} = 0, \tag{A.5}$$

$$\frac{\partial \rho v}{\partial t} + \frac{\partial \rho uv}{\partial x} + \frac{\partial \rho v^2}{\partial y} + \frac{\partial \rho vw}{\partial z} + \rho\gamma u + \frac{\partial p}{\partial y} - \frac{\partial \tau_{xy}}{\partial x} - \frac{\partial \tau_{yy}}{\partial y} - \frac{\partial \tau_{yz}}{\partial z} = 0, \tag{A.6}$$

$$\frac{\partial \rho w}{\partial t} + \frac{\partial \rho uw}{\partial x} + \frac{\partial \rho vw}{\partial y} + \frac{\partial \rho w^2}{\partial z} + \frac{\partial p}{\partial z} + \rho g - \frac{\partial \tau_{xz}}{\partial x} - \frac{\partial \tau_{yz}}{\partial y} - \frac{\partial \tau_{zz}}{\partial z} = 0. \tag{A.7}$$

Here u, v and w are the velocities in the x, y and z direction, z is positive upward, t is the time, p is the pressure, ρ is the density, g is the gravitation constant and γ the Coriolis parameter. The viscous stresses are defined by τ_{ij} and are defined as

$$\frac{\tau_{ij}}{\rho} = \frac{\partial u_i}{\partial x_j} + \frac{\partial u_j}{\partial x_i}. \tag{A.8}$$

The Navier-Stokes equations can be simplified by observing that realistic temperature and salinity variations lead only to small variations in the density. These small variations have little effect on most terms in the Navier-Stokes equations, their effect is only of importance in the gravitational term. Therefore, the density is assumed to be constant in all terms except the gravitational term, this is called the Boussinesq approximation. In [25] the conditions for this approximation are examined. As a consequence of the Boussinesq approximation, equations (A.5)-(A.7) read,

$$\frac{\partial u}{\partial t} + \frac{\partial u^2}{\partial x} + \frac{\partial uv}{\partial y} + \frac{\rho uw}{\partial z} - \gamma v + \frac{1}{\rho_0}\frac{\partial p}{\partial x} - \frac{1}{\rho_0}\left(\frac{\partial \tau_{xx}}{\partial x} + \frac{\partial \tau_{xy}}{\partial y} + \frac{\partial \tau_{xz}}{\partial z}\right) = 0, \tag{A.9}$$

$$\frac{\partial v}{\partial t} + \frac{\partial uv}{\partial x} + \frac{\partial v^2}{\partial y} + \frac{\partial vw}{\partial z} + \gamma u + \frac{1}{\rho_0}\frac{\partial p}{\partial y} - \frac{1}{\rho_0}\left(\frac{\partial \tau_{xy}}{\partial x} + \frac{\partial \tau_{yy}}{\partial y} + \frac{\partial \tau_{yz}}{\partial z}\right) = 0, \tag{A.10}$$

$$\frac{\partial w}{\partial t} + \frac{\partial uw}{\partial x} + \frac{\rho vw}{\partial y} + \frac{\partial w^2}{\partial z} + \frac{1}{\rho_0}\frac{\partial p}{\partial z} + \frac{\rho g}{\rho_0} - \frac{1}{\rho_0}\left(\frac{\partial \tau_{xz}}{\partial x} + \frac{\partial \tau_{yz}}{\partial y} + \frac{\partial \tau_{zz}}{\partial z}\right) = 0. \tag{A.11}$$

A.2. Reynolds averaging

Flow in an estuary is turbulent, this means it consists of stochastic motions. Usually, one is having interest in large scale flow and not the turbulent fluctuations. To isolate the large scale features, each variable can be decomposed into a turbulence averaged contribution (indicated by an overbar) and a fluctuating part (indicated by an inverted comma), here illustrated for the velocity component u,

$$u = \overline{u} + u'. \tag{A.12}$$

It is important to realise the average of the fluctuating part is 0 and therefore the mean of a product is not the product of the means,

$$\overline{uv} = \overline{\overline{u}\,\overline{v}} + \overline{\overline{u}v'} + \overline{\overline{v}u'} + \overline{u'v'} = \overline{u}\,\overline{v} + \overline{u'v'}. \tag{A.13}$$

Substituting the decomposition in the Navier-Stokes equations results in,

$$\begin{aligned}\frac{\partial \overline{u}+u'}{\partial t} + \frac{\partial(\overline{u}+u')^2}{\partial x} + \frac{\partial(\overline{u}+u')(\overline{v}+v')}{\partial y} + \frac{\partial(\overline{u}+u')(\overline{w}+w')}{\partial z} - \gamma\left(\overline{v}+v'\right) \\ + \frac{1}{\rho_0}\frac{\partial \overline{p}+p'}{\partial x} - \frac{1}{\rho_0}\left(\frac{\partial \overline{\tau_{xx}}+\tau'_{xx}}{\partial x} + \frac{\partial \overline{\tau_{xy}}+\tau'_{xy}}{\partial y} + \frac{\partial \overline{\tau_{xz}}+\tau'_{xz}}{\partial z}\right) = 0,\end{aligned} \tag{A.14}$$

$$\begin{aligned}\frac{\partial \overline{v}+v'}{\partial t} + \frac{\partial(\overline{u}+u')(\overline{v}+v')}{\partial x} + \frac{\partial(\overline{v}+v')^2}{\partial y} + \frac{\partial(\overline{v}+v')(\overline{w}+w')}{\partial z} + \gamma\left(\overline{u}+u'\right) \\ + \frac{1}{\rho_0}\frac{\partial \overline{p}+p'}{\partial y} - \frac{1}{\rho_0}\left(\frac{\partial \overline{\tau_{xy}}+\tau'_{xy}}{\partial x} + \frac{\partial \overline{\tau_{yy}}+\tau'_{yy}}{\partial y} + \frac{\partial \overline{\tau_{yz}}+\tau'_{yz}}{\partial z}\right) = 0,\end{aligned} \tag{A.15}$$

$$\begin{aligned}\frac{\partial \overline{w}+w'}{\partial t} + \frac{\partial(\overline{u}+u')(\overline{w}+w')}{\partial x} + \frac{\partial(\overline{v}+v')(\overline{w}+w')}{\partial y} + \frac{\partial(\overline{w}+w')^2}{\partial z} + \frac{\rho g}{\rho_0} \\ + \frac{1}{\rho_0}\frac{\partial \overline{p}+p'}{\partial z} - \frac{1}{\rho_0}\left(\frac{\partial \overline{\tau_{xz}}+\tau'_{xz}}{\partial x} + \frac{\partial \overline{\tau_{yz}}+\tau'_{yz}}{\partial y} + \frac{\partial \overline{\tau_{zz}}+\tau'_{zz}}{\partial z}\right) = 0,\end{aligned} \tag{A.16}$$

and, similarly for the continuity equation,

$$\frac{\partial \overline{u}+u'}{\partial x} + \frac{\partial \overline{v}+v'}{\partial y} + \frac{\partial \overline{w}+w'}{\partial z} = 0. \tag{A.17}$$

Next, these equations are averaged over the turbulent time scale. Using that the average of the fluctuating part is 0 and the result of equation (A.13), one finds

$$\frac{\partial \overline{u}}{\partial t}+\frac{\partial \overline{uu}}{\partial x}+\frac{\partial \overline{u'u'}}{\partial x}+\frac{\partial \overline{uv}}{\partial y}+\frac{\partial \overline{u'v'}}{\partial y}+\frac{\partial \overline{uw}}{\partial z}+\frac{\partial \overline{u'w'}}{\partial z}-\gamma\overline{v}+\frac{1}{\rho_0}\frac{\partial \overline{p}}{\partial x}-\frac{1}{\rho_0}\left(\frac{\partial \overline{\tau_{xx}}}{\partial x}+\frac{\partial \overline{\tau_{xy}}}{\partial y}+\frac{\partial \overline{\tau_{xz}}}{\partial z}\right)=0, \quad \text{(A.18)}$$

$$\frac{\partial \overline{v}}{\partial t}+\frac{\partial \overline{uv}}{\partial x}+\frac{\partial \overline{u'v'}}{\partial x}+\frac{\partial \overline{vv}}{\partial y}+\frac{\partial \overline{v'v'}}{\partial y}+\frac{\partial \overline{vw}}{\partial z}+\frac{\partial \overline{v'w'}}{\partial z}+\gamma\overline{u}+\frac{1}{\rho_0}\frac{\partial \overline{p}}{\partial y}-\frac{1}{\rho_0}\left(\frac{\partial \overline{\tau_{xy}}}{\partial x}+\frac{\partial \overline{\tau_{yy}}}{\partial y}+\frac{\partial \overline{\tau_{yz}}}{\partial z}\right)=0, \quad \text{(A.19)}$$

$$\frac{\partial \overline{w}}{\partial t}+\frac{\partial \overline{uw}}{\partial x}+\frac{\partial \overline{u'w'}}{\partial x}+\frac{\partial \overline{vw}}{\partial y}+\frac{\partial \overline{v'w'}}{\partial y}+\frac{\partial \overline{ww}}{\partial z}+\frac{\partial \overline{w'w'}}{\partial z}+\frac{\rho g}{\rho_0}+\frac{1}{\rho_0}\frac{\partial \overline{p}}{\partial z}-\frac{1}{\rho_0}\left(\frac{\partial \overline{\tau_{xz}}}{\partial x}+\frac{\partial \overline{\tau_{yz}}}{\partial y}+\frac{\partial \overline{\tau_{zz}}}{\partial z}\right)=0, \quad \text{(A.20)}$$

$$\frac{\partial \overline{u}}{\partial x}+\frac{\partial \overline{v}}{\partial y}+\frac{\partial \overline{w}}{\partial z}=0. \quad \text{(A.21)}$$

These equations have the same form as the Navier-Stokes equations except that there are some extra terms of the form $\partial \overline{u_i' u_j'}/\partial x_k$. When multiplied with the density, these terms are called Reynold stresses and represent the exchange of momentum between fluid elements in a turbulent motion. Combining them with the viscous stresses, results in

$$\mathrm{T}_{ij}=\rho_0\left[\nu\left(\frac{\overline{u_i}}{\partial x_j}+\frac{\overline{u_j}}{\partial x_i}\right)-\overline{u_i' u_j'}\right]. \quad \text{(A.22)}$$

From now on the overbar will be discarded. However, it is important to realise the variables still represent the turbulence averaged quantities. At this moment the following equations have been obtained

$$\frac{\partial u}{\partial t}+\frac{\partial u^2}{\partial x}+\frac{\partial uv}{\partial y}+\frac{\partial uw}{\partial z}-\gamma v+\frac{1}{\rho_0}\frac{\partial p}{\partial x}-\frac{1}{\rho_0}\left(\frac{\partial \mathrm{T}_{xx}}{\partial x}+\frac{\partial \mathrm{T}_{xy}}{\partial y}+\frac{\partial \mathrm{T}_{xz}}{\partial z}\right)=0, \quad \text{(A.23)}$$

$$\frac{\partial v}{\partial t}+\frac{\partial uv}{\partial x}+\frac{\partial v^2}{\partial y}+\frac{\partial vw}{\partial z}+\gamma u+\frac{1}{\rho_0}\frac{\partial p}{\partial y}-\frac{1}{\rho_0}\left(\frac{\partial \mathrm{T}_{xy}}{\partial x}+\frac{\partial \mathrm{T}_{yy}}{\partial y}+\frac{\partial \mathrm{T}_{yz}}{\partial z}\right)=0, \quad \text{(A.24)}$$

$$\frac{\partial w}{\partial t}+\frac{\partial uw}{\partial x}+\frac{\partial vw}{\partial y}+\frac{\partial w^2}{\partial z}+\frac{\rho g}{\rho_0}+\frac{1}{\rho_0}\frac{\partial p}{\partial z}-\frac{1}{\rho_0}\left(\frac{\partial \mathrm{T}_{xz}}{\partial x}+\frac{\partial \mathrm{T}_{yz}}{\partial y}+\frac{\partial \mathrm{T}_{zz}}{\partial z}\right)=0, \quad \text{(A.25)}$$

$$\frac{\partial u}{\partial x}+\frac{\partial v}{\partial y}+\frac{\partial w}{\partial z}=0. \quad \text{(A.26)}$$

A.3. Shallow water assumption

Now the shallow water assumption is used. This means the vertical scales are assumed to be much smaller than the horizontal scales. For example the water depth must be much smaller than the characteristic width of the river or estuary, but also the amplitude of waves must be much smaller than their wavelength.

For x and y, the typical length scale is L, for z the typical length scale is H and due to the shallow water approximation $L \gg H$. Moreover, for the horizontal velocities, the typical scale is U and for the vertical velocity the scale is W. Considering the continuity equation (A.4), the derivatives with respect to x and y scale as U/L whereas the derivative with respect to z as W/H. The two U/L terms will usually not cancel each other, which means the last term must also be of the order U/L. As a consequence, the vertical velocity w must be of the order UH/L and thus the vertical velocity is smaller than the horizontal velocity by the same factor as the ratio of the length scales.

Now consider the vertical momentum equation (A.25). All terms in this equation can be estimated except the pressure gradient, the advective terms can be scaled as U^2H/L^2, the stress terms are of a scale U/L^2 or U/H^2. This means all terms are small compared to the gravitational acceleration and thus only the pressure gradient can balance the gravitational acceleration. Equation (A.25) can then be simplified to the hydrostatic pressure distribution,

$$\frac{\partial p}{\partial z}=-\rho g. \quad \text{(A.27)}$$

Note that ρ is here the actual density that depends on the salinity and temperature. To find p, equation (A.27) is integrated from the free surface. The z-coordinate is defined as pointing upward, with $z = 0$ at the average free surface and $z = -H$ at the bottom. The deviation from the free surface is indicated by ζ. Integrating from the free surface then gives,

$$p = g \int_z^\zeta \rho \, \mathrm{d}z + p_a, \tag{A.28}$$

with p_a the atmospheric pressure. The derivative of the pressure with respect to x is,

$$\frac{\partial p}{\partial x} = g \frac{\partial}{\partial x} \int_z^\zeta \rho \, \mathrm{d}z + \frac{\partial p_a}{\partial x} = g\rho \frac{\partial \zeta}{\partial x} + g \int_z^\zeta \frac{\partial \rho}{\partial x} \, \mathrm{d}z + \frac{\partial p_a}{\partial x}, \tag{A.29}$$

in the second equality Leibniz rule is used. The derivative with respect to y is similar.

Often the rigid lid approximation is used, this means variations in the surface level are assumed to be small. Therefore, surface displacements are ignored but the pressure gradient due to the variations is not neglected. For the derivative of the pressure, this results in,

$$\frac{\partial p}{\partial x} = g\rho \frac{\partial \zeta}{\partial x} + g \int_z^0 \frac{\partial \rho}{\partial x} \, \mathrm{d}z + \frac{\partial p_a}{\partial x}. \tag{A.30}$$

A.4. Parametrization of the turbulent terms

Last, the terms containing the stresses τ_{ij} have to be rewritten since these expressions still contain turbulent fluctuations. Parametrizations of these turbulent terms result in

$$\frac{1}{\rho_0} \left(\frac{\partial \mathrm{T}_{xx}}{\partial x} + \frac{\partial \mathrm{T}_{xy}}{\partial y} + \frac{\partial \mathrm{T}_{xz}}{\partial z} \right) = \frac{\partial}{\partial x} \left(A_h \frac{\partial u}{\partial x} \right) + \frac{\partial}{\partial y} \left(A_h \frac{\partial u}{\partial y} \right) + \frac{\partial}{\partial z} \left(A_v \frac{\partial u}{\partial z} \right), \tag{A.31}$$

for the u-momentum equation. Here A_h is the horizontal eddy viscosity coefficient and A_v the vertical eddy viscosity coefficient. A similar expression is found for the v-momentum equation. There are several turbulence models available to derive A_h and A_v. In [3] more information about different turbulence models can be found. Generally, more complicated turbulence models result in more sophisticated expressions for the turbulence but also make it harder to solve the equations.

A.5. Shallow water equations

Collecting all terms, the three dimensional shallow water equations are obtained

$$\begin{aligned} \frac{\partial u}{\partial t} + \frac{\partial u^2}{\partial x} + \frac{\partial uv}{\partial y} + \frac{\partial uw}{\partial z} - \gamma v + g \frac{\partial \zeta}{\partial x} + \frac{g}{\rho_0} \int_z^0 \frac{\partial \rho}{\partial x} \, \mathrm{d}z + \frac{1}{\rho_0} \frac{\partial p_a}{\partial x} \\ - \frac{\partial}{\partial x} \left(A_h \frac{\partial u}{\partial x} \right) - \frac{\partial}{\partial y} \left(A_h \frac{\partial u}{\partial y} \right) - \frac{\partial}{\partial z} \left(A_v \frac{\partial u}{\partial z} \right) = 0, \end{aligned} \tag{A.32}$$

$$\begin{aligned} \frac{\partial v}{\partial t} + \frac{\partial uv}{\partial x} + \frac{\partial v^2}{\partial y} + \frac{\partial vw}{\partial z} + \gamma u + g \frac{\partial \zeta}{\partial y} + \frac{g}{\rho_0} \int_z^0 \frac{\partial \rho}{\partial y} \, \mathrm{d}z + \frac{1}{\rho_0} \frac{\partial p_a}{\partial y} \\ - \frac{\partial}{\partial x} \left(A_h \frac{\partial u}{\partial x} \right) - \frac{\partial}{\partial y} \left(A_h \frac{\partial u}{\partial y} \right) - \frac{\partial}{\partial z} \left(A_v \frac{\partial u}{\partial z} \right) = 0, \end{aligned} \tag{A.33}$$

$$\frac{\partial u}{\partial x} + \frac{\partial v}{\partial y} + \frac{\partial w}{\partial z} = 0. \tag{A.34}$$

It is important to realise multiple assumptions have been made in the derivation of these equations and not every assumption holds at all times. For example close to the boundaries, the relevant horizontal length scale is no longer L but the distance to the boundary. This means the shallow water assumption will not hold close to the boundaries and these equations are not valid there.

B

Derivation of a condition for the lateral water flux

In Section 2.2.2, equation (2.5) is introduced. This is the condition that requires the cross-channel transport of water to be zero at every point along the transect. In this appendix the derivation of this condition is discussed.

First, the continuity equation (2.3) is integrated over depth,

$$\int_{-H}^{0} \left(\frac{u_r}{r} + \frac{\partial u_r}{\partial r} + \frac{\partial u_z}{\partial z} \right) \mathrm{d}z = 0. \tag{B.1}$$

Using Leibniz integral rule, this integral is equal to

$$\frac{1}{r} \int_{-h}^{0} u_r \, \mathrm{d}z + \frac{\partial}{\partial r} \int_{h}^{0} u_r \, \mathrm{d}z - u_r(-h) \frac{\partial h}{\partial r} + u_z(0) - u_z(-h) = 0. \tag{B.2}$$

According to the boundary conditions, $u_z(0)$, $u_z(-h)$ and $u_r(-h)$ must be 0, this gives

$$\frac{1}{r} \int_{-h}^{0} u_r \, \mathrm{d}z + \frac{\partial}{\partial r} \int_{h}^{0} u_r \, \mathrm{d}z = 0, \tag{B.3}$$

and thus

$$\int_{-h}^{0} u_r \, \mathrm{d}z = \frac{I}{r}, \tag{B.4}$$

with I a constant. Because this should also hold at the side walls, where u_r equals zero, I must be zero and equation (2.5) is obtained.

C

Derivation of the morphodynamic equilibrium condition

In this appendix the step by step derivation of the morphodynamic equilibrium condition is given. The derivation is largely following the same approach as used in [11].

First the sediment mass balance equation (2.12) is rearranged into,

$$\frac{\partial c}{\partial t}+\frac{1}{r}\frac{\partial r u_r c}{\partial r}+\frac{\partial\left(u_z-w_s\right)c}{\partial z}-D_v\frac{\partial}{\partial z}\left(\phi\frac{\partial c}{\partial z}\right)-D_h\frac{1}{r}\frac{\partial}{\partial r}\left(r\frac{\partial c}{\partial r}\right)=0. \tag{C.1}$$

Next, this equation is averaged over a tidal period,

$$\frac{1}{r}\frac{\partial\langle r u_r c\rangle}{\partial r}+\frac{\partial\langle\left(u_z-w_s\right)c\rangle}{\partial z}-D_v\frac{\partial}{\partial z}\left(\phi\frac{\partial\langle c\rangle}{\partial z}\right)-D_h\frac{1}{r}\frac{\partial}{\partial r}\left(r\frac{\partial\langle c\rangle}{\partial r}\right)=0. \tag{C.2}$$

Subsequently, the equation is integrated over depth,

$$\int_{-H}^{0}\frac{1}{r}\frac{\partial\langle r u_r c\rangle}{\partial r}+\frac{\partial\langle\left(u_z-w_s\right)c\rangle}{\partial z}-D_v\frac{\partial}{\partial z}\left(\phi\frac{\partial\langle c\rangle}{\partial z}\right)-D_h\frac{1}{r}\frac{\partial}{\partial r}\left(r\frac{\partial\langle c\rangle}{\partial r}\right)\mathrm{d}z=0. \tag{C.3}$$

Grouping the derivatives with respect to r and z and using Leibniz integral rule gives,

$$\begin{aligned}&\frac{1}{r}\frac{\partial}{\partial r}\int_{-H}^{0}\langle r u_r c\rangle-D_h r\frac{\partial\langle c\rangle}{\partial r}\,\mathrm{d}z-\frac{\partial H}{\partial r}\left(\langle u_r c\rangle-D_h\frac{\partial\langle c\rangle}{\partial r}\right)\Big|_{z=-H}\\&+\left(\langle\left(u_z-w_s\right)c\rangle-D_v\phi\frac{\partial\langle c\rangle}{\partial z}\right)\Big|_{z=0}-\left(\langle\left(u_z-w_s\right)c\rangle-D_v\phi\frac{\partial\langle c\rangle}{\partial z}\right)\Big|_{z=-H}=0.\end{aligned} \tag{C.4}$$

At the surface, equation (2.15) must hold and u_z must be zero. At the bottom, u_r and u_z must be zero. This results in,

$$\frac{1}{r}\frac{\partial}{\partial r}\int_{-H}^{0}\langle r u_r c\rangle-D_h r\frac{\partial\langle c\rangle}{\partial r}\,\mathrm{d}z+\left(\langle w_s c\rangle+D_h\frac{\partial\langle c\rangle}{\partial r}\frac{\partial H}{\partial r}+D_v\phi\frac{\partial\langle c\rangle}{\partial z}\right)\Big|_{z=-H}=0. \tag{C.5}$$

Now the balance between erosion and deposition at the bed, equation (2.21), is used. Substituting the definitions for erosion and deposition, equations (2.16) and (2.20), and using $n_r\approx\frac{dH}{dr}$ and $n_z\approx 1$, results at $z=-H$ in,

$$\begin{aligned}\langle D\rangle-\langle E\rangle=0\quad&\Leftrightarrow\\ w_s\langle c\rangle n_z+D_h\frac{\partial\langle c\rangle}{\partial r}n_r+D_v\frac{\partial\langle c\rangle}{\partial z}n_z=0\quad&\Leftrightarrow\\ w_s\langle c\rangle+D_h\frac{\partial\langle c\rangle}{\partial r}\frac{dH}{dr}+D_v\frac{\partial\langle c\rangle}{\partial z}=0.&\end{aligned} \tag{C.6}$$

This means equation (C.5) reduces to,

$$\frac{1}{r}\frac{\partial}{\partial r}\int_{-H}^{0}\langle ru_r c\rangle - D_h r\frac{\partial\langle c\rangle}{\partial r}\,\mathrm{d}z = 0. \tag{C.7}$$

Because $r \neq 0$, it follows that

$$r\int_{-H}^{0}\langle u_r c\rangle - D_h\frac{\partial\langle c\rangle}{\partial r}\,\mathrm{d}z = I, \tag{C.8}$$

with I a constant. Due to the boundary condition (2.13), the integral must be zero at the side walls. Consequently, the constant I must be equal to zero. This finally leads to the morphodynamic equilibrium condition,

$$\int_{-H}^{0}\langle u_r c\rangle - D_v\frac{\partial\langle c\rangle}{\partial r}\,\mathrm{d}z = 0, \tag{C.9}$$

for every r. When this condition holds, there is a morphodynamic equilibrium.

D

Coordinate transformation

In the first section of Chapter 3 is mentioned that a coordinate transformation is applied to solve the flow and concentration equations. The details of the transformation are given in this appendix.

Equations (2.1), (2.2), (2.3) and (2.12) are defined in the (r, θ, z) coordinate system in the physical domain. The cylindrical coordinate system (r, θ, z) is mapped onto a system (ξ, θ, σ), in which the coordinates ξ and σ are defined such that the concerned cross-section of the channel is represented by a rectangle in the computational domain. An example of a physical domain and the corresponding computational domain is visualised in Figure D.1.

The coordinate σ is defined as,

$$\sigma = \frac{z}{h} + 1, \tag{D.1}$$

such that σ is 0 at the bottom and 1 at the surface. Moreover,

$$\frac{\partial \xi}{\partial r} = 1 \qquad \text{and} \qquad \frac{\partial \xi}{\partial z} = 0. \tag{D.2}$$

When a line is parallel to the ξ-axis in the computational domain, this relates in the physical domain to a curve with constant relative height above the bottom.

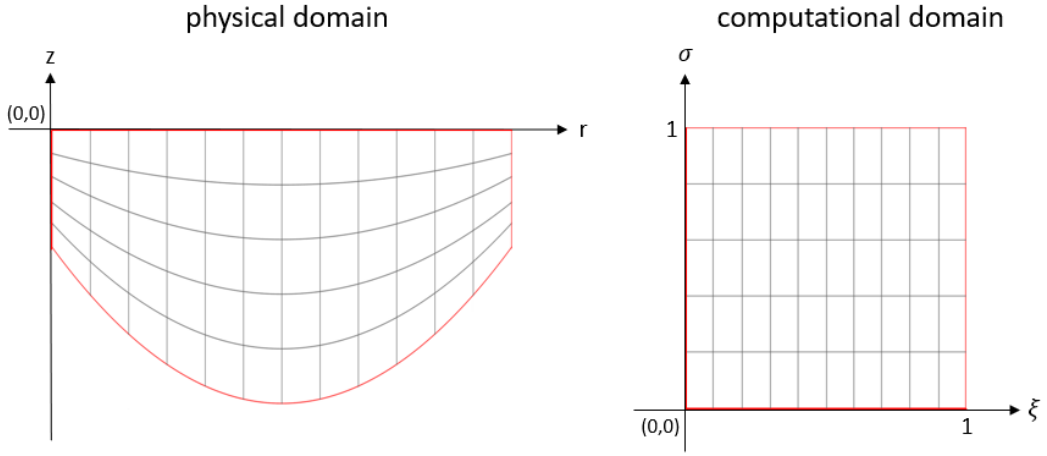

Figure D.1: On the left is an example of a physical domain in the (r, z) coordinate system. On the right is the corresponding computational domain which has a (ξ, σ) coordinate system.

The transformation results in the expressions,

$$\frac{\partial \sigma}{\partial z} = \frac{1}{h}, \tag{D.3}$$

$$\frac{\partial^2 \sigma}{\partial z^2} = 0, \tag{D.4}$$

$$\frac{\partial \sigma}{\partial r} = -\frac{z}{h^2}\frac{dh}{dr} = (1-\sigma)\frac{1}{h}\frac{dh}{dr}, \tag{D.5}$$

$$\frac{\partial^2 \sigma}{\partial r^2} = -\frac{z}{h^2}\frac{d^2h}{dr^2} + 2\frac{z}{h^3}\left(\frac{dh}{dr}\right)^2 = (1-\sigma)\left(\frac{1}{h}\frac{d^2h}{dr^2} - 2\left(\frac{1}{h}\frac{dh}{dr}\right)^2\right). \tag{D.6}$$

Which can be used for the following operations

$$\frac{\partial \cdot}{\partial r} = \frac{\partial \cdot}{\partial \xi} + \frac{\partial \sigma}{\partial r}\frac{\partial \cdot}{\partial \sigma}, \tag{D.7}$$

$$\frac{\partial^2 \cdot}{\partial r^2} = \frac{\partial^2 \cdot}{\partial \xi^2} + \left(\frac{\partial \sigma}{\partial r}\right)^2 \frac{\partial^2 \cdot}{\partial \sigma^2} + 2\frac{\partial \sigma}{\partial r}\frac{\partial^2 \cdot}{\partial \sigma \partial \xi} + \frac{\partial^2 \xi}{\partial r^2}\frac{\partial \cdot}{\partial \xi} + \frac{\partial^2 \sigma}{\partial r^2}\frac{\partial \cdot}{\partial \sigma}, \tag{D.8}$$

$$\frac{\partial \cdot}{\partial z} = \frac{\partial \sigma}{\partial z}\frac{\partial \cdot}{\partial \sigma}, \tag{D.9}$$

$$\frac{\partial^2 \cdot}{\partial z^2} = \left(\frac{\partial \sigma}{\partial z}\right)^2 \frac{\partial^2 \cdot}{\partial \sigma^2}. \tag{D.10}$$

Using the above expressions, equations (2.1), (2.2), (2.5) and (2.12) are transformed to

$$\begin{aligned}&\frac{\partial u_r}{\partial t} + u_r\left(\frac{\partial u_r}{\partial \xi} + \frac{\partial \sigma}{\partial r}\frac{\partial u_r}{\partial \sigma}\right) + u_z\frac{1}{h}\frac{\partial u_r}{\partial \sigma} - \gamma u_\theta - \frac{u_\theta^2}{r} = -\frac{g}{\rho_0}\int_\sigma^1 \frac{\partial \rho}{\partial r}\,\mathrm{d}\sigma' - g\frac{\partial \zeta}{\partial r}\\ &+ A_v\frac{1}{h^2}\frac{\partial}{\partial \sigma}\left(\phi\frac{\partial u_r}{\partial \sigma}\right) + A_h\frac{1}{r}\left(\frac{\partial}{\partial \xi}\left(r\left(\frac{\partial u_r}{\partial \xi} + \frac{\partial \sigma}{\partial r}\frac{\partial u_r}{\partial \sigma}\right)\right) + \frac{\partial \sigma}{\partial r}\frac{\partial}{\partial \sigma}\left(r\left(\frac{\partial u_r}{\partial \xi} + \frac{\partial \sigma}{\partial r}\frac{\partial u_r}{\partial \sigma}\right)\right)\right),\end{aligned} \tag{D.11}$$

$$\begin{aligned}&\frac{\partial u_\theta}{\partial t} + u_r\left(\frac{\partial u_\theta}{\partial \xi} + \frac{\partial \sigma}{\partial r}\frac{\partial u_\theta}{\partial \sigma}\right) + u_z\frac{1}{h}\frac{\partial u_\theta}{\partial \sigma} + \gamma u_r + \frac{u_\theta u_r}{r} = -\frac{g}{\rho_0}\int_\sigma^1 \frac{1}{r}\frac{\partial \rho}{\partial \theta}\,\mathrm{d}\sigma' - g\frac{1}{r}\frac{\partial \zeta}{\partial \theta} +\\ &A_v\frac{1}{h^2}\frac{\partial}{\partial \sigma}\left(\phi\frac{\partial u_\theta}{\partial \sigma}\right) + A_h\frac{1}{r}\left(\frac{\partial}{\partial \xi}\left(r\left(\frac{\partial u_\theta}{\partial \xi} + \frac{\partial \sigma}{\partial r}\frac{\partial u_\theta}{\partial \sigma}\right)\right) + \frac{\partial \sigma}{\partial r}\frac{\partial}{\partial \sigma}\left(r\left(\frac{\partial u_\theta}{\partial \xi} + \frac{\partial \sigma}{\partial r}\frac{\partial u_\theta}{\partial \sigma}\right)\right)\right),\end{aligned} \tag{D.12}$$

$$\int_0^1 u_r\,\mathrm{d}\sigma = 0, \tag{D.13}$$

$$\begin{aligned}&\frac{\partial c}{\partial t} + \frac{u_r c}{r} + u_r\left(\frac{\partial c}{\partial \xi} + \frac{\partial \sigma}{\partial r}\frac{\partial c}{\partial \sigma}\right) + (u_z - w_s)\frac{1}{h}\frac{\partial c}{\partial \sigma} = -D_v\frac{1}{h^2}\frac{\partial}{\partial \sigma}\left(\phi\frac{\partial c}{\partial \sigma}\right)\\ &- D_h\frac{1}{r}\left(\frac{\partial}{\partial \xi}\left(r\left(\frac{\partial c}{\partial \xi} + \frac{\partial \sigma}{\partial r}\frac{\partial c}{\partial \sigma}\right)\right) + \frac{\partial \sigma}{\partial r}\frac{\partial}{\partial \sigma}\left(r\left(\frac{\partial c}{\partial \xi} + \frac{\partial \sigma}{\partial r}\frac{\partial c}{\partial \sigma}\right)\right)\right).\end{aligned} \tag{D.14}$$

E

Eigenfunction expansion in the vertical domain

This appendix explains the series expansion in the vertical direction used to compute u_r, u_θ and c. The technique applied in this model is based on [5], where a special case of the Sturm-Liouville eigenvalue problem is used to simplify the vertical mixing term in the momentum balance. First, the eigenfunctions for the horizontal velocities are discussed in Section E.1. Next, the eigenfunctions for the concentration are discussed in Section E.2.

E.1. Eigenfunction expansion for horizontal velocities

With a series expansion in the vertical direction, the horizontal velocities can be expressed as,

$$u_r(\xi,\sigma,t) = \sum_{m=1}^{M+N} U_m(\xi,t) f_m(\xi,\sigma), \tag{E.1}$$

$$u_\theta(\xi,\sigma,t) = \sum_{m=1}^{M+N} V_m(\xi,t) f_m(\xi,\sigma). \tag{E.2}$$

The value for M can be chosen depending on the desired number eigenfunctions f_m. More eigenfunctions results in a higher accuracy but also leads to more computational time and required storage space. The eigenfunctions represent a problem with homogeneous boundary conditions at the surface and bottom boundary. To solve a situation with a non-zero wind shear stress, which is an in-homogeneous boundary condition, a different defined eigenfunction f_{M+1} is introduced. At the bottom boundary, the vertical mixing term cannot be represented with the eigenfunctions for $m = 1 \ldots (M+1)$. Therefore, the eigenfunction f_{M+2} is introduced. Later in this section, these additional eigenfunctions are explained more thoroughly. The number of differently defined eigenfunctions is indicated by N, in this case N equals two.

The eigenfunctions, $f_m(\xi,\sigma)$ are, for $m = 1 \ldots M$, derived from the Sturm-Liouville eigenvalue problem,

$$\frac{\partial}{\partial\sigma}\left(\phi(\xi,\sigma)\frac{\partial f_m}{\partial\sigma}\right) + \lambda_m f_m w(\xi,\sigma) = 0 \tag{E.3}$$

with

$$f_m(\xi,0) = \frac{\partial f_m}{\partial\sigma}(\xi,1) = 0. \tag{E.4}$$

The λ_m are eigenvalues and $w(\xi,\sigma)$ is a weight function. The weight function w can be chosen arbitrary but must be continuous and on $[0,1]$. The boundary conditions for the Sturm-Liouville eigenvalue problem correspond to a no-slip condition at the bottom and a zero wind shear stress at the surface.

Because this Sturm-Liouville eigenvalue problem is used, filling in the vertical diffusion term of the momentum balance leads to,

$$\frac{A_v}{h^2}\frac{\partial}{\partial\sigma}\left(\phi\frac{\partial u_r}{\partial\sigma}\right)=\frac{A_v}{h^2}\frac{\partial}{\partial\sigma}\left(\phi\sum_{m=1}^{M+N}U_m\frac{\partial f_m}{\partial\sigma}\right)=\frac{A_v}{h^2}\sum_{m=1}^{M+N}U_m\frac{\partial}{\partial\sigma}\left(\phi\frac{\partial f_m}{\partial\sigma}\right)=-\frac{A_v}{h^2}\sum_{m=1}^{M+N}U_m\lambda_m f_m w. \quad \text{(E.5)}$$

This result is much simpler than the original mixing term. For u_θ a similar result is obtained.

The solution of the Sturm-Liouville eigenvalue problem depends on the shape function of the eddy viscosity ϕ. Often the eigenvalues cannot be computed analytically but the computational effort can be decreased by a good choice for $w(\xi,\sigma)$. T.J. Zitman figured out a definition for $w(\xi,\sigma)$ that is especially suitable for this model. He advised to define the weight function as,

$$w(\xi,\sigma)=\frac{c_\eta(\xi)^2}{\phi(\xi,\sigma)},\quad c_\eta(\xi)=\left(\int_0^1\frac{1}{\phi(\xi,\sigma')}\,\mathrm{d}\sigma'\right)^{-1}. \quad \text{(E.6)}$$

To show why this is a suitable choice for the weight function, a coordinate transformation is applied from (ξ,σ) to (ψ,η). This coordinate system is defined such that η is 0 at the bottom and 1 at the surface and

$$\frac{\partial\psi}{\partial\sigma}=0,\qquad\frac{\partial\psi}{\partial\xi}=\frac{\partial\psi}{\partial r}=1. \quad \text{(E.7)}$$

After applying this transformation, equation (E.3) reads,

$$\frac{\partial}{\partial\eta}\left(\phi\frac{\partial\eta}{\partial\sigma}\frac{\partial f_m}{\partial\eta}\right)\frac{\partial\eta}{\partial\sigma}+\lambda_m f_m w=0. \quad \text{(E.8)}$$

The transformation is defined such that,

$$\phi\frac{\partial\eta}{\partial\sigma}=c_\eta, \quad \text{(E.9)}$$

with

$$c_\eta=\left(\int_0^1\frac{1}{\phi(\sigma)}\,\mathrm{d}\sigma\right)^{-1}, \quad \text{(E.10)}$$

which leads to,

$$\eta=\int_0^\sigma\frac{1}{\phi(\sigma')}\,\mathrm{d}\sigma'. \quad \text{(E.11)}$$

Using this and the choice for w, leads to

$$\frac{\partial}{\partial\eta}\left(\frac{\partial f_m}{\partial\eta}\right)+\lambda_m f_m=0, \quad \text{(E.12)}$$

which results in

$$f_m(\xi,\sigma)\propto\sin\left(\eta\sqrt{\lambda_m}\right). \quad \text{(E.13)}$$

with

$$\lambda_m=\left(m-\frac{1}{2}\right)\pi.$$

This means the eigenfunctions must be proportional to a sine in the (ξ,σ) domain as well,

$$f_m(\xi,\sigma)\propto\sin\left(c_\eta\sqrt{\lambda_m}\int_0^\sigma\frac{1}{\phi(\xi,\sigma')}\,\mathrm{d}\sigma'\right). \quad \text{(E.14)}$$

Clearly, the choice for w simplified the computation of the eigenvalues. Therefore, this choice for the weight function is used in the model.

At both the bottom and surface boundary, the flow cannot be represented by the eigenfunctions derived for $m=1\ldots M$. To deal with this, two more eigenfunctions are introduced, which are differently defined. At the surface, the boundary condition (2.4) cannot be met for a non-zero wind shear stress

since the derivative of f_m with respect to σ equals zero at the surface. To solve this, f_{M+1} is introduced which is derived from,

$$\frac{\partial}{\partial\sigma}\left(\phi(\xi,\sigma)\frac{\partial f_{M+1}}{\partial\sigma}\right)+\lambda_{M+1}f_{M+1}w(\xi,\sigma)=0 \tag{E.15}$$

with

$$f_{M+1}(\xi,0)=f_{M+1}(\xi,1)=0. \tag{E.16}$$

This leads to,

$$f_{M+1}(\xi,\sigma)\propto\sin(\pi\eta)=\sin\left(c_\eta\pi\int_0^\sigma\frac{1}{\phi(\xi,\sigma')}\,\mathrm{d}\sigma'\right). \tag{E.17}$$

As a consequence, the weights corresponding to f_{M+1} are determined by the wind shear stress,

$$A_zU_{M+1}=-\frac{h}{\pi c_\eta}\frac{\tau_{w,r}}{\rho_0},\qquad A_zV_{M+1}=-\frac{h}{\pi c_\eta}\frac{\tau_{w,\theta}}{\rho_0}. \tag{E.18}$$

At the bottom, there is a different inconsistency. Since the eigenfunctions are zero at the bottom, the vertical mixing, equation (E.5), cannot be represented there. Because the velocities are zero at the bottom, the momentum equation could then only hold for a zero pressure gradient, which is unlikely. This issue only occurs at exactly $\sigma=0$ and not slightly above.

This effect is called the Gibbs phenomena and to avoid this problem another eigenfunction, f_{M+2}, is added. This eigenfunction follows from,

$$\frac{\partial}{\partial\sigma}\left(\phi(\xi,\sigma)\frac{\partial f_{M+2}}{\partial\sigma}\right)=-w, \tag{E.19}$$

with

$$f_{M+2}(\xi,0)=\frac{\partial f_{M+2}}{\partial\sigma}(\xi,1)=0. \tag{E.20}$$

This results in,

$$f_{M+2}(\xi,\sigma)\propto\frac{\eta(2-\eta)}{2}=\frac{c_\eta}{2}\int_0^\sigma\frac{1}{\phi(\xi,\sigma')}\,\mathrm{d}\sigma'\left(2-c_\eta\int_0^\sigma\frac{1}{\phi(\xi,\sigma')}\,\mathrm{d}\sigma'\right). \tag{E.21}$$

By evaluating the momentum equations for $\sigma=0$, the expressions for U_{M+2} and V_{M+2} can be obtained,

$$U_{M+2}=-\frac{h^2}{A_v}\left(\frac{gh}{\rho_0}\int_1^0\frac{\partial\rho}{\partial r}\,\mathrm{d}\sigma+g\frac{\partial\zeta}{\partial r}-A_h\frac{1}{r}\frac{\partial}{\partial r}\left(r\frac{\partial u_r}{\partial r}\right)\right)\frac{1}{w(\xi,0)}, \tag{E.22}$$

$$V_{M+2}=-\frac{h^2}{A_v}\left(\frac{gh}{\rho_0}\int_1^0\frac{1}{r}\frac{\partial\rho}{\partial\theta}\,\mathrm{d}\sigma+g\frac{1}{r}\frac{\partial\zeta}{\partial\theta}-A_h\frac{1}{r}\frac{\partial}{\partial r}\left(r\frac{\partial u_\theta}{\partial r}\right)\right)\frac{1}{w(\xi,0)}. \tag{E.23}$$

Using the continuity equation (2.3), u_z can be eliminated from the momentum equations because it can be expressed as,

$$u_z=-\int_{-h}^{z}\frac{u_r}{r}+\frac{\partial u_r}{\partial r}\,\mathrm{d}z. \tag{E.24}$$

Applying the coordinate transformation to (ξ,θ,σ) and substituting the series expansion in the expression for u_z results in,

$$\begin{aligned}u_z=&-h\int_0^\sigma\frac{u_r}{r}+\frac{\partial u_r}{\partial\xi}+\frac{\partial\sigma'}{\partial r}\frac{\partial u_r}{\partial\sigma'}\,\mathrm{d}\sigma'=\\&-h\sum_{m=1}^{M+N}\left(U_m\int_0^\sigma\frac{f_m}{r}+\frac{\partial f_m}{\partial\xi}+\frac{\partial\sigma'}{\partial r}\frac{\partial f_m}{\partial\sigma'}\,\mathrm{d}\sigma'+\frac{\partial U_m}{\partial\xi}\int_0^\sigma f_m\,\mathrm{d}\sigma'\right).\end{aligned} \tag{E.25}$$

After applying the coordinate transformation explained in Appendix D, inserting the series expansions, substituting equation (E.25) for u_z and rearranging some of the terms, equations (2.1), (2.2) and (2.5) become,

$$\begin{aligned}
&\sum_{m=1}^{M+N} \frac{\partial U_m}{\partial t} f_m + \sum_{m=1}^{M+N}\sum_{n=1}^{M+N} U_m f_m \left(\frac{\partial U_n}{\partial \xi} f_n + U_n \frac{\partial f_n}{\partial \xi} + \frac{\partial \sigma}{\partial r} U_n \frac{\partial f_n}{\partial \sigma} \right) \\
&- \sum_{m=1}^{M+N}\sum_{n=1}^{M+N} U_m \frac{\partial f_m}{\partial \sigma} \left(U_n \int_0^\sigma \frac{f_n}{r} + \frac{\partial f_n}{\partial \xi} + \frac{\partial \sigma'}{\partial r}\frac{\partial f_n}{\partial \sigma'} \,\mathrm{d}\sigma + \frac{\partial U_n}{\partial \xi} \int_0^\sigma f_n \,\mathrm{d}\sigma' \right) - \gamma \sum_{m=1}^{M+N} V_n f_n \\
&- \frac{1}{r} \sum_{m=1}^{M+N}\sum_{n=1}^{M+N} V_m f_m V_n f_n + \frac{g}{\rho_0} \int_0^\sigma \frac{\partial \rho}{\partial r} \,\mathrm{d}\sigma' + g \frac{\partial \zeta}{\partial r} - A_v \frac{1}{h^2} \sum_{m=1}^{M+N} U_m \frac{\partial}{\partial \sigma} \phi \frac{\partial f_m}{\partial \sigma} - A_h L(U_m, f_m) = 0,
\end{aligned} \tag{E.26}$$

$$\begin{aligned}
&\sum_{m=1}^{M+N} \frac{\partial V_m}{\partial t} f_m + \sum_{m=1}^{M+N}\sum_{n=1}^{M+N} U_m f_m \left(\frac{\partial V_n}{\partial \xi} f_n + V_n \frac{\partial f_n}{\partial \xi} + \frac{\partial \sigma}{\partial r} V_n \frac{\partial f_n}{\partial \sigma} \right) \\
&- \sum_{m=1}^{M+N}\sum_{n=1}^{M+N} V_m \frac{\partial f_m}{\partial \sigma} \left(U_n \int_0^\sigma \frac{f_n}{r} + \frac{\partial f_n}{\partial \xi} + \frac{\partial \sigma'}{\partial r}\frac{\partial f_n}{\partial \sigma'} \,\mathrm{d}\sigma + \frac{\partial U_n}{\partial \xi} \int_0^\sigma f_n \,\mathrm{d}\sigma' \right) + \gamma \sum_{m=1}^{M+N} U_n f_n \\
&- \frac{1}{r} \sum_{m=1}^{M+N}\sum_{n=1}^{M+N} U_m f_m V_n f_n + \frac{g}{\rho_0} \int_0^\sigma \frac{1}{r}\frac{\partial \rho}{\partial \theta} \,\mathrm{d}\sigma' + g \frac{1}{r}\frac{\partial \zeta}{\partial \theta} - A_v \frac{1}{h^2} \sum_{m=1}^{M+N} V_m \frac{\partial}{\partial \sigma} \phi \frac{\partial f_m}{\partial \sigma} - A_h L(V_m, f_m) = 0,
\end{aligned} \tag{E.27}$$

$$\int_0^1 \sum_{m=1}^{M+N} U_m f_m \,\mathrm{d}\sigma = 0. \tag{E.28}$$

The operator $L(*, \star)$ is used to slightly simplify the equations. $L(*, \star)$ is defined as,

$$L(*, \star) = \frac{1}{r} \sum_{m=1}^{M+N} \left(\frac{\partial}{\partial \xi} \left(r \left(\frac{\partial *}{\partial \xi} \star + * \left(\frac{\partial \star}{\partial \xi} + \frac{\partial \sigma}{\partial r}\frac{\partial \star}{\partial \sigma} \right) \right) \right) + \frac{\partial \sigma}{\partial r}\frac{\partial}{\partial \sigma} \left(r \left(\frac{\partial *}{\partial \xi} \star + * \left(\frac{\partial \star}{\partial \xi} + \frac{\partial \sigma}{\partial r}\frac{\partial \star}{\partial \sigma} \right) \right) \right) \right) \tag{E.29}$$

The model equations are combined with the boundary conditions to describe the flow in the cross-section. The boundary conditions are, at the surface,

$$A_z U_{M+1} + \frac{h}{\pi c_\eta} \frac{\tau_{w,r}}{\rho_0} = 0, \tag{E.30}$$

$$A_z V_{M+1} + \frac{h}{\pi c_\eta} \frac{\tau_{w,\theta}}{\rho_0} = 0, \tag{E.31}$$

and at the bottom,

$$\frac{A_v}{h^2} U_{M+2} + \frac{gh}{\rho_0 w(\xi, 0)} \int_0^1 \frac{\partial \rho}{\partial r} \,\mathrm{d}\sigma + \frac{g}{w(\xi, 0)} \frac{\partial \zeta}{\partial r} - \frac{A_h}{w(\xi, 0)} L(U_m, f_m) = 0, \tag{E.32}$$

$$\frac{A_v}{h^2} V_{M+2} + \frac{gh}{\rho_0 w(\xi, 0)} \int_0^1 \frac{1}{r}\frac{\partial \rho}{\partial \theta} \,\mathrm{d}\sigma + \frac{g}{w(\xi, 0)} \frac{1}{r}\frac{\partial \zeta}{\partial \theta} - \frac{A_h}{w(\xi, 0)} L(U_m, f_m) = 0. \tag{E.33}$$

In addition, at the side walls, the velocities must be equal to 0.

E.2. Eigenfunction expansion for sediment concentration

For the sediment concentration, a similar eigenfunction expansion is used as for the flow. The concentration is written as

$$c(\xi,\sigma,t)=\sum_{m=1}^{M+N} C_m(\xi,t)d_m(\xi,\sigma), \tag{E.34}$$

The eigenfunctions d_m are different than the eigenfunctions for the flow since different boundary conditions are used for the Sturm-Liouville eigenvalue problem. For $m=1\ldots M$, the eigenfunctions d_m are derived from the following Sturm-Liouville eigenvalue problem,

$$\frac{\partial}{\partial\sigma}\left(\phi(\xi,\sigma)\frac{\partial d_m}{\partial\sigma}+\mu_m d_m w(\xi,\sigma)\right)=0, \tag{E.35}$$

with the boundary conditions,

$$\left.\frac{\partial d_m}{\partial\sigma}\right|_{\sigma=0}=\left.\frac{\partial d_m}{\partial\sigma}\right|_{\sigma=1}=0. \tag{E.36}$$

The same coordinate transformation to (ψ,η) and definition for w are used as in the previous section. This leads to,

$$d_m\propto\cos(\eta(\xi,\sigma)\sqrt{\mu_m})=\cos\left(c_\eta\sqrt{\mu_m}\int_0^\sigma\frac{1}{\phi(\xi,\sigma')}\,\mathrm{d}\sigma'\right), \tag{E.37}$$

with

$$\sqrt{\mu_m}=(m-1)\pi. \tag{E.38}$$

Comparable with the flow, this eigenfunction expansion also leads to inconsistencies at both the surface and bottom boundary because the boundary conditions for the concentration are not homogeneous. To solve this, again two eigenfunctions are added. These are chosen to be the same eigenfunctions as used for the flow, so $d_{M+1}=f_{M+1}$ and $d_{M+2}=f_{M+2}$.

Filling in the eigenfunction expansion for the surface boundary condition (2.15), results in,

$$\sum_{m=1}^{M+N} C_m\left(w_s d_m(\xi,1)+D_v\phi(\xi,1)\frac{1}{h}\frac{\partial d_m(\xi,1)}{\partial z}\right)=0. \tag{E.39}$$

Since

$$d_m(\xi,1)=\begin{cases}-(-1)^m, & \text{for } m=1\ldots M\\ 0, & \text{for } m=M+1\\ \frac{1}{2} & \text{for } m=M+2\end{cases};\quad \phi(\xi,1)\frac{\partial d_m(\xi,1)}{\partial\sigma}=\begin{cases}0, & \text{for } m=1\ldots M\\ -\pi c_\eta, & \text{for } m=M+1\\ 0 & \text{for } m=M+2\end{cases}, \tag{E.40}$$

this boundary condition is equivalent to

$$w_s\sum_{m=1}^{M}(-1)^m C_m-\frac{\pi c_\eta}{h}D_v C_{M+1}+\frac{1}{2}w_s C_{M+2}=0. \tag{E.41}$$

For the bottom boundary condition (2.19), substituting c by the eigenfunction expansion gives,

$$-D_v\phi(\xi,0)\frac{1}{h}\sum_{m=M+1}^{M+N} C_m\frac{\partial d_m}{\partial\sigma}=\frac{w_s\rho_s}{g'D_s}a(r)\chi. \tag{E.42}$$

It is only necessary to sum over $(M+1)$ till $(M+N)$ because for $m=1\ldots M$, the derivative of d_m with respect to σ is equal to zero at $\sigma=0$. For $m=(M+1)$ and $m=(M+2)$ the following holds,

$$\frac{\partial d_m(\xi,0)}{\partial\sigma}=\frac{c_\eta}{\phi(\xi,0)}(1-\delta_{m,M+1}(1-\pi)). \tag{E.43}$$

Therefore, the boundary condition can be rewritten as,

$$-\frac{c_\eta}{h}D_v\sum_{m=M+1}^{M+N}C_m(1-\delta_{m,M+1}(1-\pi))=\frac{w_s\rho_s}{g'D_s}a(r)\chi. \tag{E.44}$$

After applying the coordinate transformation outlined in Appendix D and filling in the series expansion, the equation for the sediment concentration (2.12), becomes,

$$\begin{aligned}&\sum_{m=1}^{M+N}\frac{\partial C_m}{\partial t}d_m+\sum_{m=1}^{M+N}\sum_{n=1}^{M+N}\frac{U_m f_m C_n d_n}{r}+\sum_{m=1}^{M+N}\sum_{n=1}^{M+N}U_m f_m\left(\frac{\partial C_n}{\partial\xi}d_n+C_n\left(\frac{\partial d_n}{\partial\xi}+\frac{\partial\sigma}{\partial r}\frac{\partial d_n}{\partial\sigma}\right)\right)+\\&u_z\frac{1}{h}\sum_{m=1}^{M+N}C_m\frac{\partial d_m}{\partial\sigma}-w_s\frac{1}{h}\sum_{m=1}^{M+N}C_m\frac{\partial d_m}{\partial\sigma}-D_v\frac{1}{h^2}\sum_{m=1}^{M+N}C_m\frac{\partial}{\partial\sigma}\left(\phi\frac{\partial d_m}{\partial\sigma}\right)-D_h L(C_m,d_m)=0,\end{aligned} \tag{E.45}$$

with $L(*,\star)$ as defined in equation (E.29). This is combined with the equations for boundary conditions to describe the distribution of sediment. For the surface and bottom boundary conditions, equations (E.41) and (E.44) are used. For the side walls, equation (2.14) must be transformed to the (ξ,σ) coordinate system and the series expansions should be substituted. Since the concentration is described with the same d_m at ξ_1 as at ξ_2 and at ξ_L as at ξ_{L-1}, it must hold that the derivative of d_m with respect to r equals zero at the side walls. This results in,

$$\frac{\partial c}{\partial r}=\sum_{m=1}^{M+N}\left(\frac{\partial C_m}{\partial\xi}d_m+C_m\frac{\partial d_m}{\partial\sigma}\frac{\partial\sigma}{\partial r}\right)=0, \tag{E.46}$$

at the side walls.

F

Model Equations

In Chapter 2 the model equations were introduced and in Chapter 3 is explained how they can be solved. In this appendix the model equations resulting after applying the coordinate transformation, eigenfunction expansions and Galerkin method. To make this slightly more structured and compact, some coefficients are used in the notation and implementation of these equations. In the first section the model equations for the flow are given, the second section contains the equations for the sediment concentration and in the third section the equations for the side walls are described. The last section contains the definitions of the coefficients Φ, Ψ and T which are used in the model equations.

F.1. Model equations for flow

Momentum Equation, cross-channel, test function 1

$$
\begin{aligned}
&-\frac{\pi}{\omega}\frac{1}{2\Delta\xi}\sum_{m=1}^{M+N}\sum_{n=1}^{M+N}\left\{2U_m^{(0)}(\xi_{i-1})\,U_n^{(0)}(\xi_i)+\sum_{k=1}^{K}\left(U_{m,k}^{(c)}(\xi_{i-1})\,U_{n,k}^{(c)}(\xi_i)+U_{m,k}^{(s)}(\xi_{i-1})\,U_{n,k}^{(s)}(\xi_i)\right)\right\}\Phi_{m,n,p}^{(arx)}\\
&+\frac{\pi}{\omega}\sum_{m=1}^{M+N}\sum_{n=1}^{M+N}\left\{2U_m^{(0)}(\xi_i)\,U_n^{(0)}(\xi_i)+\sum_{k=1}^{K}\left(U_{m,k}^{(c)}(\xi_i)\,U_{n,k}^{(c)}(\xi_i)+U_{m,k}^{(s)}(\xi_i)\,U_{n,k}^{(s)}(\xi_i)\right)\right\}\Phi_{m,n,p}^{(ar)}\\
&+\frac{\pi}{\omega}\frac{1}{2\Delta\xi}\sum_{m=1}^{M+N}\sum_{n=1}^{M+N}\left\{2U_m^{(0)}(\xi_{i+1})\,U_n^{(0)}(\xi_i)+\sum_{k=1}^{K}\left(U_{m,k}^{(c)}(\xi_{i+1})\,U_{n,k}^{(c)}(\xi_i)+U_{m,k}^{(s)}(\xi_{i+1})\,U_{n,k}^{(s)}(\xi_i)\right)\right\}\Phi_{m,n,p}^{(arx)}\\
&-\frac{\pi}{\omega}\frac{1}{2\Delta\xi}\sum_{m=1}^{M+N}\sum_{n=1}^{M+N}\left\{2U_m^{(0)}(\xi_i)\,U_n^{(0)}(\xi_{i-1})+\sum_{k=1}^{K}\left(U_{m,k}^{(c)}(\xi_i)\,U_{n,k}^{(c)}(\xi_{i-1})+U_{m,k}^{(s)}(\xi_i)\,U_{n,k}^{(s)}(\xi_{i-1})\right)\right\}\Phi_{m,n,p}^{(azx)}\\
&+\frac{\pi}{\omega}\sum_{m=1}^{M+N}\sum_{n=1}^{M+N}\left\{2U_m^{(0)}(\xi_i)\,U_n^{(0)}(\xi_i)+\sum_{k=1}^{K}\left(U_{m,k}^{(c)}(\xi_i)\,U_{n,k}^{(c)}(\xi_i)+U_{m,k}^{(s)}(\xi_i)\,U_{n,k}^{(s)}(\xi_i)\right)\right\}\Phi_{m,n,p}^{(az)}\\
&+\frac{\pi}{\omega}\frac{1}{2\Delta\xi}\sum_{m=1}^{M+N}\sum_{n=1}^{M+N}\left\{2U_m^{(0)}(\xi_i)\,U_n^{(0)}(\xi_{i+1})+\sum_{k=1}^{K}\left(U_{m,k}^{(c)}(\xi_i)\,U_{n,k}^{(c)}(\xi_{i+1})+U_{m,k}^{(s)}(\xi_i)\,U_{n,k}^{(s)}(\xi_{i+1})\right)\right\}\Phi_{m,n,p}^{(azx)}
\end{aligned}
$$

$$
\begin{aligned}
&-\gamma\frac{2\pi}{\omega}\sum_{m=1}^{M+N}V_m^{(0)}(\xi_i)\,\Phi_{m,p}^{(icd)}\\
&-\frac{\pi}{\omega}\sum_{m=1}^{M+N}\sum_{n=1}^{M+N}\left\{2V_m^{(0)}(\xi_i)\,V_n^{(0)}(\xi_i)+\sum_{k=1}^{K}\left(V_{m,k}^{(c)}(\xi_i)\,V_{n,k}^{(c)}(\xi_i)+V_{m,k}^{(s)}(\xi_i)\,V_{n,k}^{(s)}(\xi_i)\right)\right\}\Phi_{m,n,p}^{(cur)}\\
&+g\frac{2\pi}{\omega}P^{(0)}\Phi_{m,p}^{(dr)}+g\frac{2\pi}{\omega}E^{(0)}(\xi_i)\,\Phi_p^{(sr)}\\
&-\frac{\pi}{\omega}\sum_{m=1}^{M+N}\left\{2U_m^{(0)}(\xi_i)\,A^{(0)}+\sum_{k=1}^{K}\left(U_{m,k}^{(c)}(\xi_i)\,A_k^{(c)}+U_{m,k}^{(s)}(\xi_i)\,A_k^{(s)}\right)\right\}\Phi_{m,p}^{(mix)}\\
&-A_h\frac{2\pi}{\omega}\sum_{m=1}^{M+N}\left\{U_m^{(0)}(\xi_{i-1})\left(-\frac{1}{2\Delta\xi}\Phi_{m,p}^{(difx)}+\frac{1}{\Delta\xi^2}\Phi_{m,p}^{(icd)}\right)+U_m^{(0)}(\xi_i)\left(\Phi_{m,p}^{(dif)}-\frac{2}{\Delta\xi^2}\Phi_{m,p}^{(icd)}\right)\right.\\
&\qquad\left.+U_m^{(0)}(\xi_{i+1})\left(\frac{1}{2\Delta\xi}\Phi_{m,p}^{(difx)}+\frac{1}{\Delta\xi^2}\Phi_{m,p}^{(icd)}\right)\right\}\\
&=0\qquad\text{for } p=1\ldots M
\end{aligned}
\tag{F.1}
$$

Wind, cross-channel, test function 1

$$
\frac{2\pi}{\omega}U_{M+1}^{(0)}(\xi_i)A^{(0)}+\frac{\pi}{\omega}\sum_{k=1}^{K}\left(U_{M+1}^{(c)}(\xi_i)A_k^{(c)}+U_{M+1}^{(s)}(\xi_i)A_k^{(s)}\right)+\frac{2\pi}{\omega}\frac{h}{\pi c}\frac{\tau_{w,r}}{\rho_0}=0 \tag{F.2}
$$

Gibbs Effect, cross-channel, test function 1

$$
\begin{aligned}
&\frac{1}{h^2}\left(\frac{2\pi}{\omega}U_{M+2}^{(0)}(\xi_i)\,A^{(0)}+\frac{\pi}{\omega}\sum_{k=1}^{K}\left(U_{M+2,k}^{(c)}(\xi_i)\,A_k^{(c)}+U_{M+2,k}^{(s)}(\xi_i)\,A_k^{(s)}\right)\right)+\frac{2\pi}{\omega}\frac{g}{w(0)}E^{(0)}(\xi_i)\\
&+\frac{2\pi}{\omega}\frac{gh}{w(0)}P^{(0)}-\frac{2\pi}{\omega}\frac{A_h}{w(0)}\sum_{m=1}^{M+N}\left(U_m^{(0)}(\xi_i)\,\Phi_m^{(grx)}+\frac{1}{2\Delta\xi}\left(-U_m^{(0)}(\xi_{i-1})+U_m^{(0)}(\xi_{i+1})\right)\Phi_m^{(gr)}\right)=0
\end{aligned}
\tag{F.3}
$$

Momentum Equation, along-channel, test function 1

$$
\begin{aligned}
&-\frac{\pi}{\omega}\frac{1}{2\Delta\xi}\sum_{m=1}^{M+N}\sum_{n=1}^{M+N}\left\{2V_m^{(0)}(\xi_{i-1})\,U_n^{(0)}(\xi_i)+\sum_{k=1}^{K}\left(V_{m,k}^{(c)}(\xi_{i-1})\,U_{n,k}^{(c)}(\xi_i)+V_{m,k}^{(s)}(\xi_{i-1})\,U_{n,k}^{(s)}(\xi_i)\right)\right\}\Phi_{m,n,p}^{(arx)}\\
&+\frac{\pi}{\omega}\sum_{m=1}^{M+N}\sum_{n=1}^{M+N}\left\{2V_m^{(0)}(\xi_i)\,U_n^{(0)}(\xi_i)+\sum_{k=1}^{K}\left(V_{m,k}^{(c)}(\xi_i)\,U_{n,k}^{(c)}(\xi_i)+V_{m,k}^{(s)}(\xi_i)\,U_{n,k}^{(s)}(\xi_i)\right)\right\}\Phi_{m,n,p}^{(ar)}\\
&+\frac{\pi}{\omega}\frac{1}{2\Delta\xi}\sum_{m=1}^{M+N}\sum_{n=1}^{M+N}\left\{2V_m^{(0)}(\xi_{i+1})\,U_n^{(0)}(\xi_i)+\sum_{k=1}^{K}\left(V_{m,k}^{(c)}(\xi_{i+1})\,U_{n,k}^{(c)}(\xi_i)+V_{m,k}^{(s)}(\xi_{i+1})\,U_{n,k}^{(s)}(\xi_i)\right)\right\}\Phi_{m,n,p}^{(arx)}\\
&-\frac{\pi}{\omega}\frac{1}{2\Delta\xi}\sum_{m=1}^{M+N}\sum_{n=1}^{M+N}\left\{2V_m^{(0)}(\xi_i)\,U_n^{(0)}(\xi_{i-1})+\sum_{k=1}^{K}\left(V_{m,k}^{(c)}(\xi_i)\,U_{n,k}^{(c)}(\xi_{i-1})+V_{m,k}^{(s)}(\xi_i)\,U_{n,k}^{(s)}(\xi_{i-1})\right)\right\}\Phi_{m,n,p}^{(azx)}\\
&+\frac{\pi}{\omega}\sum_{m=1}^{M+N}\sum_{n=1}^{M+N}\left\{2V_m^{(0)}(\xi_i)\,U_n^{(0)}(\xi_i)+\sum_{k=1}^{K}\left(V_{m,k}^{(c)}(\xi_i)\,U_{n,k}^{(c)}(\xi_i)+V_{m,k}^{(s)}(\xi_i)\,U_{n,k}^{(s)}(\xi_i)\right)\right\}\Phi_{m,n,p}^{(az)}\\
&+\frac{\pi}{\omega}\frac{1}{2\Delta\xi}\sum_{m=1}^{M+N}\sum_{n=1}^{M+N}\left\{2V_m^{(0)}(\xi_i)\,U_n^{(0)}(\xi_{i+1})+\sum_{k=1}^{K}\left(V_{m,k}^{(c)}(\xi_i)\,U_{n,k}^{(c)}(\xi_{i+1})+V_{m,k}^{(s)}(\xi_i)\,U_{n,k}^{(s)}(\xi_{i+1})\right)\right\}\Phi_{m,n,p}^{(azx)}
\end{aligned}
$$

$$
\begin{aligned}
&+\gamma\frac{2\pi}{\omega}\sum_{m=1}^{M+N}U_m^{(0)}(\xi_i)\,\Phi_{m,p}^{(icd)}\\
&-\frac{\pi}{\omega}\sum_{m=1}^{M+N}\sum_{n=1}^{M+N}\left\{2V_m^{(0)}(\xi_i)\,U_n^{(0)}(\xi_i)+\sum_{k=1}^{K}\left(V_{m,k}^{(c)}(\xi_i)\,U_{n,k}^{(c)}(\xi_i)+V_{m,k}^{(s)}(\xi_i)\,U_{n,k}^{(s)}(\xi_i)\right)\right\}\Phi_{m,n,p}^{(cur)}\\
&+g\frac{2\pi}{\omega}Y^{(0)}\Phi_p^{(dt)}+g\frac{2\pi}{\omega}H^{(0)}(\xi_i)\,\Phi_p^{(st)}\\
&-\frac{\pi}{\omega}\sum_{m=1}^{M+N}\left\{2V_m^{(0)}(\xi_i)\,A^{(0)}+\sum_{k=1}^{K}\left(V_{m,k}^{(c)}(\xi_i)\,A_k^{(c)}+V_{m,k}^{(s)}(\xi_i)\,A_k^{(s)}\right)\right\}\Phi_{m,p}^{(mix)}\\
&-A_h\frac{2\pi}{\omega}\sum_{m=1}^{M+N}\left\{V_m^{(0)}(\xi_{i-1})\left(-\frac{1}{2\Delta\xi}\Phi_{m,p}^{(difx)}+\frac{1}{\Delta\xi^2}\Phi_{m,p}^{(icd)}\right)+V_m^{(0)}(\xi_i)\left(\Phi_{m,p}^{(dif)}-\frac{2}{\Delta\xi^2}\Phi_{m,p}^{(icd)}\right)\right.\\
&\qquad\left.+V_m^{(0)}(\xi_{i+1})\left(\frac{1}{2\Delta\xi}\Phi_{m,p}^{(difx)}+\frac{1}{\Delta\xi^2}\Phi_{m,p}^{(icd)}\right)\right\}\\
&=0\qquad\text{for } p=1\ldots M
\end{aligned}
\tag{F.4}
$$

Wind, along-channel, test function 1

$$
\frac{2\pi}{\omega}V_{M+1}^{(0)}(\xi_i)A^{(0)}+\frac{\pi}{\omega}\sum_{k=1}^{K}\left(V_{M+1}^{(c)}A_k^{(c)}(\xi_i)+V_{M+1}^{(s)}(\xi_i)A_k^{(s)}\right)+\frac{2\pi}{\omega}\frac{h}{\pi c}\frac{\tau_{w,\theta}}{\rho_0}=0 \tag{F.5}
$$

Gibbs Effect, along-channel, test function 1

$$
\begin{aligned}
&\frac{1}{h^2}\left(\frac{2\pi}{\omega}V_{M+2}^{(0)}(\xi_i)\,A^{(0)}+\frac{\pi}{\omega}\sum_{k=1}^{K}\left(V_{M+2,k}^{(c)}(\xi_i)\,A_k^{(c)}+V_{M+2,k}^{(s)}(\xi_i)\,A_k^{(s)}\right)\right)+\frac{2\pi}{\omega}\frac{g}{w(0)}\frac{r_0}{r}H^{(0)}\\
&+\frac{2\pi}{\omega}\frac{gh}{w(0)}\frac{r_0}{r}Y^{(0)}-\frac{2\pi}{\omega}\frac{A_h}{w(0)}\sum_{m=1}^{M+N}\left(V_m^{(0)}(\xi_i)\,\Phi_m^{(\mathrm{gr}x)}+\frac{1}{2\Delta\xi}\left(-V_m^{(0)}(\xi_{i-1})+V_m^{(0)}(\xi_{i+1})\right)\Phi_m^{(\mathrm{gr})}\right)=0
\end{aligned}
\tag{F.6}
$$

Rigid lid effect, test function 1

$$
\frac{2\pi}{\omega}\sum_{m=1}^{M+N}U_m^{(0)}(\xi_i)\Phi_m^{(q)} \tag{F.7}
$$

Momentum Equation, cross-channel, test function $\cos(q\omega t)$

$$
\begin{aligned}
&\sum_{m=1}^{M+N}q\pi U_{m,q}^{(s)}\Phi_{m,q}^{(icd)}\\
&-\frac{\pi}{\omega}\frac{1}{2\Delta\xi}\sum_{m=1}^{M+N}\sum_{n=1}^{M+N}\left\{\left(U_m^{(0)}(\xi_{i-1})\,U_{n,q}^{(c)}(\xi_i)+U_{m,q}^{(c)}(\xi_{i-1})\,U_n^{(0)}(\xi_i)\right)\right.\\
&\qquad\left.+\sum_{k=1}^{K}\sum_{j=1}^{K}\left(U_{m,k}^{(c)}(\xi_{i-1})\,U_{n,j}^{(c)}(\xi_i)\,T_{k,j,q}^{(ccc)}+U_{m,k}^{(s)}(\xi_{i-1})\,U_{n,j}^{(s)}(\xi_i)\,T_{k,j,q}^{(ssc)}\right)\right\}\Phi_{m,n,p}^{(arx)}
\end{aligned}
$$

$$
\begin{aligned}
&+\frac{\pi}{\omega}\frac{1}{2\Delta\xi}\sum_{m=1}^{M+N}\sum_{n=1}^{M+N}\Bigg\{\left(U_m^{(0)}(\xi_i)\,U_{n,q}^{(c)}(\xi_i)+U_{m,q}^{(c)}(\xi_i)\,U_n^{(0)}(\xi_i)\right)\\
&\qquad\qquad+\sum_{k=1}^{K}\sum_{j=1}^{K}\left(U_{m,k}^{(c)}(\xi_i)\,U_{n,j}^{(c)}(\xi_i)\,T_{k,j,q}^{(ccc)}+U_{m,k}^{(s)}(\xi_i)\,U_{n,j}^{(s)}(\xi_i)\,T_{k,j,q}^{(ssc)}\right)\Bigg\}\Phi_{m,n,p}^{(ar)}\\
&+\frac{\pi}{\omega}\frac{1}{2\Delta\xi}\sum_{m=1}^{M+N}\sum_{n=1}^{M+N}\Bigg\{\left(U_m^{(0)}(\xi_{i+1})\,U_{n,q}^{(c)}(\xi_i)+U_{m,q}^{(c)}(\xi_{i+1})\,U_n^{(0)}(\xi_i)\right)\\
&\qquad\qquad+\sum_{k=1}^{K}\sum_{j=1}^{K}\left(U_{m,k}^{(c)}(\xi_{i+1})\,U_{n,j}^{(c)}(\xi_i)\,T_{k,j,q}^{(ccc)}+U_{m,k}^{(s)}(\xi_{i+1})\,U_{n,j}^{(s)}(\xi_i)\,T_{k,j,q}^{(ssc)}\right)\Bigg\}\Phi_{m,n,p}^{(arx)}\\
&-\frac{\pi}{\omega}\frac{1}{2\Delta\xi}\sum_{m=1}^{M+N}\sum_{n=1}^{M+N}\Bigg\{\left(U_m^{(0)}(\xi_i)\,U_{n,q}^{(c)}(\xi_{i-1})+U_{m,q}^{(c)}(\xi_i)\,U_n^{(0)}(\xi_{i-1})\right)\\
&\qquad\qquad+\sum_{k=1}^{K}\sum_{j=1}^{K}\left(U_{m,k}^{(c)}(\xi_i)\,U_{n,j}^{(c)}(\xi_{i-1})\,T_{k,j,q}^{(ccc)}+U_{m,k}^{(s)}(\xi_i)\,U_{n,j}^{(s)}(\xi_{i-1})\,T_{k,j,q}^{(ssc)}\right)\Bigg\}\Phi_{m,n,p}^{(azx)}\\
&+\frac{\pi}{\omega}\frac{1}{2\Delta\xi}\sum_{m=1}^{M+N}\sum_{n=1}^{M+N}\Bigg\{\left(U_m^{(0)}(\xi_i)\,U_{n,q}^{(c)}(\xi_i)+U_{m,q}^{(c)}(\xi_i)\,U_n^{(0)}(\xi_i)\right)\\
&\qquad\qquad+\sum_{k=1}^{K}\sum_{j=1}^{K}\left(U_{m,k}^{(c)}(\xi_i)\,U_{n,j}^{(c)}(\xi_i)\,T_{k,j,q}^{(ccc)}+U_{m,k}^{(s)}(\xi_i)\,U_{n,j}^{(s)}(\xi_i)\,T_{k,j,q}^{(ssc)}\right)\Bigg\}\Phi_{m,n,p}^{(az)}\\
&+\frac{\pi}{\omega}\frac{1}{2\Delta\xi}\sum_{m=1}^{M+N}\sum_{n=1}^{M+N}\Bigg\{\left(U_m^{(0)}(\xi_i)\,U_{n,q}^{(c)}(\xi_{i+1})+U_{m,q}^{(c)}(\xi_i)\,U_n^{(0)}(\xi_{i+1})\right)\\
&\qquad\qquad+\sum_{k=1}^{K}\sum_{j=1}^{K}\left(U_{m,k}^{(c)}(\xi_i)\,U_{n,j}^{(c)}(\xi_{i+1})\,T_{k,j,q}^{(ccc)}+U_{m,k}^{(s)}(\xi_i)\,U_{n,j}^{(s)}(\xi_{i+1})\,T_{k,j,q}^{(ssc)}\right)\Bigg\}\Phi_{m,n,p}^{(azx)}\\
&-\gamma\frac{2\pi}{\omega}\sum_{m=1}^{M+N}V_m^{(c)}(\xi_i)\,\Phi_{m,p}^{(icd)}\\
&-\frac{\pi}{\omega}\sum_{m=1}^{M+N}\sum_{n=1}^{M+N}\Bigg\{\left(V_m^{(0)}(\xi_i)\,V_{n,q}^{(c)}(\xi_i)+V_m^{(0)}(\xi_i)\,V_{n,q}^{(c)}(\xi_i)\right)\\
&\qquad\qquad+\sum_{k=1}^{K}\sum_{j=1}^{K}\left(V_{m,k}^{(c)}(\xi_i)\,V_{n,k}^{(c)}(\xi_i)\,T_{k,j,q}^{(ccc)}+V_{m,k}^{(s)}(\xi_i)\,V_{n,k}^{(s)}(\xi_i)\,T_{k,j,q}^{(ssc)}\right)\Bigg\}\Phi_{m,n,p}^{(cur)}\\
&+g\frac{2\pi}{\omega}P^{(c)}\Phi_{m,p}^{(dr)}+g\frac{2\pi}{\omega}E^{(c)}(\xi_i)\,\Phi_p^{(sr)}\\
&-\frac{\pi}{\omega}\sum_{m=1}^{M+N}\left\{\left(U_m^{(0)}(\xi_i)\,A_q^{(c)}+U_{m,q}^{(c)}(\xi_i)\,A^{(0)}\right)+\sum_{k=1}^{K}\sum_{j=1}^{K}\left(U_{m,k}^{(c)}(\xi_i)\,A_j^{(c)}T_{k,j,q}^{(ccc)}+U_{m,k}^{(s)}(\xi_i)\,A_j^{(s)}T_{k,j,q}^{(ssc)}\right)\right\}\Phi_{m,p}^{(mix)}\\
&-A_h\frac{2\pi}{\omega}\sum_{m=1}^{M+N}\Bigg\{U_m^{(c)}(\xi_{i-1})\left(-\frac{1}{2\Delta\xi}\Phi_{m,p}^{(difx)}+\frac{1}{\Delta\xi^2}\Phi_{m,p}^{(icd)}\right)+U_m^{(c)}(\xi_i)\left(\Phi_{m,p}^{(dif)}-\frac{2}{\Delta\xi^2}\Phi_{m,p}^{(icd)}\right)\\
&\qquad\qquad+U_m^{(c)}(\xi_{i+1})\left(\frac{1}{2\Delta\xi}\Phi_{m,p}^{(difx)}+\frac{1}{\Delta\xi^2}\Phi_{m,p}^{(icd)}\right)\Bigg\}\\
&=0\qquad\text{for } p=1\ldots M
\end{aligned}
\tag{F.8}
$$

Wind, cross-channel, test function $\cos(q\omega t)$

$$\frac{\pi}{\omega}\left(U_{M+1}^{(0)}(\xi_i)A_q^{(c)} + U_{M+1,q}^{(c)}(\xi_i)A^{(0)}\right) + \frac{\pi}{\omega}\sum_{k=1}^{K}\sum_{j=1}^{K}\left(U_{M+1,k}^{(c)}(\xi_i)A_j^{(c)}T_{k,j,q}^{(ccc)} + U_{M+1,k}^{(s)}(\xi_i)A_j^{(s)}T_{k,j,q}^{(ssc)}\right) = 0 \quad \text{(F.9)}$$

Gibbs Effect, cross-channel, test function $\cos(q\omega t)$

$$\begin{aligned}
&\frac{\pi}{\omega}\frac{1}{h^2}\left(\left(U_{M+2}^{(0)}(\xi_i)\,A_q^{(c)} + U_{M+2,q}^{(c)}(\xi_i)\,A^{(0)}\right) + \sum_{k=1}^{K}\sum_{j=1}^{K}\left(U_{M+2,k}^{(c)}(\xi_i)\,A_j^{(c)}T_{k,j,q}^{(ccc)} + U_{M+2,k}^{(s)}(\xi_i)\,A_j^{(s)}T_{k,j,q}^{(ssc)}\right)\right)\\
&+\frac{\pi}{\omega}\frac{g}{w(0)}E_q^{(c)}(\xi_i) + \frac{\pi}{\omega}\frac{gh}{w(0)}P_q^{(c)}\\
&-\frac{\pi}{\omega}\frac{A_h}{w(0)}\sum_{m=1}^{M+N}\left(U_{m,q}^{(c)}(\xi_i)\,\Phi_m^{(grx)} + \frac{1}{2\Delta\xi}\left(-U_{m,q}^{(c)}(\xi_{i-1}) + U_{m,q}^{(c)}(\xi_{i+1})\right)\Phi_m^{(gr)}\right) = 0
\end{aligned} \quad \text{(F.10)}$$

Momentum Equation, along-channel, test function $\cos(q\omega t)$

$$\begin{aligned}
&\sum_{m=1}^{M+N} q\pi V_{m,q}^{(s)}\Phi_{m,q}^{(icd)}\\
&-\frac{\pi}{\omega}\frac{1}{2\Delta\xi}\sum_{m=1}^{M+N}\sum_{n=1}^{M+N}\left\{\left(V_m^{(0)}(\xi_{i-1})\,U_{n,q}^{(c)}(\xi_i) + V_{m,q}^{(c)}(\xi_{i-1})\,U_n^{(0)}(\xi_i)\right)\right.\\
&\qquad\left.+\sum_{k=1}^{K}\sum_{j=1}^{K}\left(V_{m,k}^{(c)}(\xi_{i-1})\,U_{n,j}^{(c)}(\xi_i)\,T_{k,j,q}^{(ccc)} + V_{m,k}^{(s)}(\xi_{i-1})\,U_{n,j}^{(s)}(\xi_i)\,T_{k,j,q}^{(ssc)}\right)\right\}\Phi_{m,n,p}^{(arx)}\\
&+\frac{\pi}{\omega}\frac{1}{2\Delta\xi}\sum_{m=1}^{M+N}\sum_{n=1}^{M+N}\left\{\left(V_m^{(0)}(\xi_i)\,U_{n,q}^{(c)}(\xi_i) + V_{m,q}^{(c)}(\xi_i)\,U_n^{(0)}(\xi_i)\right)\right.\\
&\qquad\left.+\sum_{k=1}^{K}\sum_{j=1}^{K}\left(V_{m,k}^{(c)}(\xi_i)\,U_{n,j}^{(c)}(\xi_i)\,T_{k,j,q}^{(ccc)} + V_{m,k}^{(s)}(\xi_i)\,U_{n,j}^{(s)}(\xi_i)\,T_{k,j,q}^{(ssc)}\right)\right\}\Phi_{m,n,p}^{(ar)}\\
&+\frac{\pi}{\omega}\frac{1}{2\Delta\xi}\sum_{m=1}^{M+N}\sum_{n=1}^{M+N}\left\{\left(V_m^{(0)}(\xi_{i+1})\,U_{n,q}^{(c)}(\xi_i) + V_{m,q}^{(c)}(\xi_{i+1})\,U_n^{(0)}(\xi_i)\right)\right.\\
&\qquad\left.+\sum_{k=1}^{K}\sum_{j=1}^{K}\left(V_{m,k}^{(c)}(\xi_{i+1})\,U_{n,j}^{(c)}(\xi_i)\,T_{k,j,q}^{(ccc)} + V_{m,k}^{(s)}(\xi_{i+1})\,U_{n,j}^{(s)}(\xi_i)\,T_{k,j,q}^{(ssc)}\right)\right\}\Phi_{m,n,p}^{(arx)}\\
&-\frac{\pi}{\omega}\frac{1}{2\Delta\xi}\sum_{m=1}^{M+N}\sum_{n=1}^{M+N}\left\{\left(V_m^{(0)}(\xi_i)\,U_{n,q}^{(c)}(\xi_{i-1}) + V_{m,q}^{(c)}(\xi_i)\,U_n^{(0)}(\xi_{i-1})\right)\right.\\
&\qquad\left.+\sum_{k=1}^{K}\sum_{j=1}^{K}\left(V_{m,k}^{(c)}(\xi_i)\,U_{n,j}^{(c)}(\xi_{i-1})\,T_{k,j,q}^{(ccc)} + V_{m,k}^{(s)}(\xi_i)\,U_{n,j}^{(s)}(\xi_{i-1})\,T_{k,j,q}^{(ssc)}\right)\right\}\Phi_{m,n,p}^{(azx)}
\end{aligned}$$

$$
\begin{aligned}
&+\frac{\pi}{\omega}\frac{1}{2\Delta\xi}\sum_{m=1}^{M+N}\sum_{n=1}^{M+N}\Bigg\{\left(V_m^{(0)}(\xi_i)\,U_{n,q}^{(c)}(\xi_i)+V_{m,q}^{(c)}(\xi_i)\,U_n^{(0)}(\xi_i)\right)\\
&\qquad\qquad+\sum_{k=1}^{K}\sum_{j=1}^{K}\left(V_{m,k}^{(c)}(\xi_i)\,U_{n,j}^{(c)}(\xi_i)\,T_{k,j,q}^{(ccc)}+V_{m,k}^{(s)}(\xi_i)\,U_{n,j}^{(s)}(\xi_i)\,T_{k,j,q}^{(ssc)}\right)\Bigg\}\Phi_{m,n,p}^{(az)}\\
&+\frac{\pi}{\omega}\frac{1}{2\Delta\xi}\sum_{m=1}^{M+N}\sum_{n=1}^{M+N}\Bigg\{\left(V_m^{(0)}(\xi_i)\,U_{n,q}^{(c)}(\xi_{i+1})+V_{m,q}^{(c)}(\xi_i)\,U_n^{(0)}(\xi_{i+1})\right)\\
&\qquad\qquad+\sum_{k=1}^{K}\sum_{j=1}^{K}\left(V_{m,k}^{(c)}(\xi_i)\,U_{n,j}^{(c)}(\xi_{i+1})\,T_{k,j,q}^{(ccc)}+V_{m,k}^{(s)}(\xi_i)\,U_{n,j}^{(s)}(\xi_{i+1})\,T_{k,j,q}^{(ssc)}\right)\Bigg\}\Phi_{m,n,p}^{(azx)}\\
&-\gamma\frac{2\pi}{\omega}\sum_{m=1}^{M+N}U_m^{(c)}(\xi_i)\,\Phi_{m,p}^{(icd)}\\
&-\frac{\pi}{\omega}\sum_{m=1}^{M+N}\sum_{n=1}^{M+N}\Bigg\{\left(V_m^{(0)}(\xi_i)\,U_{n,q}^{(c)}(\xi_i)+V_m^{(c)}(\xi_i)\,U_{n,q}^{(0)}(\xi_i)\right)\\
&\qquad\qquad+\sum_{k=1}^{K}\sum_{j=1}^{K}\left(V_{m,k}^{(c)}(\xi_i)\,U_{n,k}^{(c)}(\xi_i)\,T_{k,j,q}^{(ccc)}+V_{m,k}^{(s)}(\xi_i)\,U_{n,k}^{(s)}(\xi_i)\,T_{k,j,q}^{(ssc)}\right)\Bigg\}\Phi_{m,n,p}^{(cur)}\\
&+g\frac{2\pi}{\omega}Y^{(c)}\Phi_{m,p}^{(dt)}+g\frac{2\pi}{\omega}H^{(c)}(\xi_i)\,\Phi_p^{(st)}\\
&-\frac{\pi}{\omega}\sum_{m=1}^{M+N}\left\{\left(V_m^{(0)}(\xi_i)\,A_q^{(c)}+V_{m,q}^{(c)}(\xi_i)\,A^{(0)}\right)+\sum_{k=1}^{K}\sum_{j=1}^{K}\left(V_{m,k}^{(c)}(\xi_i)\,A_j^{(c)}T_{k,j,q}^{(ccc)}+V_{m,k}^{(s)}(\xi_i)\,A_j^{(s)}T_{k,j,q}^{(ssc)}\right)\right\}\Phi_{m,p}^{(mix)}\\
&-A_h\frac{2\pi}{\omega}\sum_{m=1}^{M+N}\Bigg\{V_m^{(c)}(\xi_{i-1})\left(-\frac{1}{2\Delta\xi}\Phi_{m,p}^{(difx)}+\frac{1}{\Delta\xi^2}\Phi_{m,p}^{(icd)}\right)+V_m^{(c)}(\xi_i)\left(\Phi_{m,p}^{(dif)}-\frac{2}{\Delta\xi^2}\Phi_{m,p}^{(icd)}\right)\\
&\qquad\qquad+V_m^{(c)}(\xi_{i+1})\left(\frac{1}{2\Delta\xi}\Phi_{m,p}^{(difx)}+\frac{1}{\Delta\xi^2}\Phi_{m,p}^{(icd)}\right)\Bigg\}\\
&=0\qquad\text{for } p=1\ldots M
\end{aligned}
\tag{F.11}
$$

Wind, along-channel, test function $\cos(q\omega t)$

$$
\frac{\pi}{\omega}\left(V_{M+1}^{(0)}(\xi_i)A_q^{(c)}+V_{M+1,q}^{(c)}(\xi_i)A^{(0)}\right)+\frac{\pi}{\omega}\sum_{k=1}^{K}\sum_{j=1}^{K}\left(V_{M+1,k}^{(c)}(\xi_i)A_j^{(c)}T_{k,j,q}^{(ccc)}+V_{M+1,k}^{(s)}(\xi_i)A_j^{(s)}T_{k,j,q}^{(ssc)}\right)=0 \tag{F.12}
$$

Gibbs Effect, along-channel, test function $\cos(q\omega t)$

$$
\begin{aligned}
&\frac{\pi}{\omega}\frac{1}{h^2}\left(\left(V_{M+2}^{(0)}(\xi_i)\,A_q^{(c)}+V_{M+2,q}^{(c)}(\xi_i)\,A^{(0)}\right)+\sum_{k=1}^{K}\sum_{j=1}^{K}\left(V_{M+2,k}^{(c)}(\xi_i)\,A_j^{(c)}T_{k,j,q}^{(ccc)}+V_{M+2,k}^{(s)}(\xi_i)\,A_j^{(s)}T_{k,j,q}^{(ssc)}\right)\right)\\
&+\frac{\pi}{\omega}\frac{g}{w(0)}\frac{r_0}{r}H_q^{(c)}+\frac{\pi}{\omega}\frac{gh}{w(0)}\frac{r_0}{r}Y_q^{(c)}\\
&-\frac{\pi}{\omega}\frac{A_h}{w(0)}\sum_{m=1}^{M+N}\left(V_{m,q}^{(c)}(\xi_i)\,\Phi_m^{(grx)}+\frac{1}{2\Delta\xi}\left(-V_{m,q}^{(c)}(\xi_{i-1})+V_{m,q}^{(c)}(\xi_{i+1})\right)\Phi_m^{(gr)}\right)=0
\end{aligned}
\tag{F.13}
$$

Rigid lid effect, test function $\cos(q\omega t)$

$$\frac{\pi}{\omega}\sum_{m=1}^{M+N} U_{m,q}^{(c)}(\xi_i)\Phi_m^{(q)} \tag{F.14}$$

Momentum Equation, cross-channel, test function $\sin(q\omega t)$

$$\begin{aligned}
&\sum_{m=1}^{M+N} q\pi U_{m,q}^{(c)}\Phi_{m,q}^{(icd)} \\
&-\frac{\pi}{\omega}\frac{1}{2\Delta\xi}\sum_{m=1}^{M+N}\sum_{n=1}^{M+N}\Bigg\{\left(U_m^{(0)}(\xi_{i-1})\,U_{n,q}^{(s)}(\xi_i)+U_{m,q}^{(s)}(\xi_{i-1})\,U_n^{(0)}(\xi_i)\right) \\
&\qquad\qquad+\sum_{k=1}^{K}\sum_{j=1}^{K}\left(U_{m,k}^{(c)}(\xi_{i-1})\,U_{n,j}^{(s)}(\xi_i)\,T_{k,j,q}^{(css)}+U_{m,k}^{(s)}(\xi_{i-1})\,U_{n,j}^{(c)}(\xi_i)\,T_{k,j,q}^{(scs)}\right)\Bigg\}\Phi_{m,n,p}^{(arx)} \\
&+\frac{\pi}{\omega}\frac{1}{2\Delta\xi}\sum_{m=1}^{M+N}\sum_{n=1}^{M+N}\Bigg\{\left(U_m^{(0)}(\xi_i)\,U_{n,q}^{(s)}(\xi_i)+U_{m,q}^{(s)}(\xi_i)\,U_n^{(0)}(\xi_i)\right) \\
&\qquad\qquad+\sum_{k=1}^{K}\sum_{j=1}^{K}\left(U_{m,k}^{(c)}(\xi_i)\,U_{n,j}^{(s)}(\xi_i)\,T_{k,j,q}^{(css)}+U_{m,k}^{(s)}(\xi_i)\,U_{n,j}^{(c)}(\xi_i)\,T_{k,j,q}^{(scs)}\right)\Bigg\}\Phi_{m,n,p}^{(ar)} \\
&+\frac{\pi}{\omega}\frac{1}{2\Delta\xi}\sum_{m=1}^{M+N}\sum_{n=1}^{M+N}\Bigg\{\left(U_m^{(0)}(\xi_{i+1})\,U_{n,q}^{(s)}(\xi_i)+U_{m,q}^{(s)}(\xi_{i+1})\,U_n^{(0)}(\xi_i)\right) \\
&\qquad\qquad+\sum_{k=1}^{K}\sum_{j=1}^{K}\left(U_{m,k}^{(c)}(\xi_{i+1})\,U_{n,j}^{(s)}(\xi_i)\,T_{k,j,q}^{(css)}+U_{m,k}^{(s)}(\xi_{i+1})\,U_{n,j}^{(c)}(\xi_i)\,T_{k,j,q}^{(scs)}\right)\Bigg\}\Phi_{m,n,p}^{(arx)} \\
&-\frac{\pi}{\omega}\frac{1}{2\Delta\xi}\sum_{m=1}^{M+N}\sum_{n=1}^{M+N}\Bigg\{\left(U_m^{(0)}(\xi_i)\,U_{n,q}^{(s)}(\xi_{i-1})+U_{m,q}^{(s)}(\xi_i)\,U_n^{(0)}(\xi_{i-1})\right) \\
&\qquad\qquad+\sum_{k=1}^{K}\sum_{j=1}^{K}\left(U_{m,k}^{(c)}(\xi_i)\,U_{n,j}^{(s)}(\xi_{i-1})\,T_{k,j,q}^{(css)}+U_{m,k}^{(s)}(\xi_i)\,U_{n,j}^{(c)}(\xi_{i-1})\,T_{k,j,q}^{(scs)}\right)\Bigg\}\Phi_{m,n,p}^{(azx)} \\
&+\frac{\pi}{\omega}\frac{1}{2\Delta\xi}\sum_{m=1}^{M+N}\sum_{n=1}^{M+N}\Bigg\{\left(U_m^{(0)}(\xi_i)\,U_{n,q}^{(s)}(\xi_i)+U_{m,q}^{(s)}(\xi_i)\,U_n^{(0)}(\xi_i)\right) \\
&\qquad\qquad+\sum_{k=1}^{K}\sum_{j=1}^{K}\left(U_{m,k}^{(c)}(\xi_i)\,U_{n,j}^{(s)}(\xi_i)\,T_{k,j,q}^{(css)}+U_{m,k}^{(s)}(\xi_i)\,U_{n,j}^{(c)}(\xi_i)\,T_{k,j,q}^{(scs)}\right)\Bigg\}\Phi_{m,n,p}^{(az)} \\
&+\frac{\pi}{\omega}\frac{1}{2\Delta\xi}\sum_{m=1}^{M+N}\sum_{n=1}^{M+N}\Bigg\{\left(U_m^{(0)}(\xi_i)\,U_{n,q}^{(s)}(\xi_{i+1})+U_{m,q}^{(s)}(\xi_i)\,U_n^{(0)}(\xi_{i+1})\right) \\
&\qquad\qquad+\sum_{k=1}^{K}\sum_{j=1}^{K}\left(U_{m,k}^{(c)}(\xi_i)\,U_{n,j}^{(s)}(\xi_{i+1})\,T_{k,j,q}^{(css)}+U_{m,k}^{(s)}(\xi_i)\,U_{n,j}^{(c)}(\xi_{i+1})\,T_{k,j,q}^{(scs)}\right)\Bigg\}\Phi_{m,n,p}^{(azx)} \\
&-\gamma\frac{2\pi}{\omega}\sum_{m=1}^{M+N}V_m^{(c)}(\xi_i)\,\Phi_{m,p}^{(icd)}
\end{aligned}$$

$$
\begin{aligned}
&-\frac{\pi}{\omega}\sum_{m=1}^{M+N}\sum_{n=1}^{M+N}\Bigg\{\left(V_m^{(0)}(\xi_i)\,V_{n,q}^{(s)}(\xi_i)+V_m^{(0)}(\xi_i)\,V_{n,q}^{(s)}(\xi_i)\right)\\
&\qquad\qquad+\sum_{k=1}^{K}\sum_{j=1}^{K}\left(V_{m,k}^{(c)}(\xi_i)\,V_{n,k}^{(s)}(\xi_i)\,T_{k,j,q}^{(css)}+V_{m,k}^{(s)}(\xi_i)\,V_{n,k}^{(c)}(\xi_i)\,T_{k,j,q}^{(scs)}\right)\Bigg\}\Phi_{m,n,p}^{(cur)}\\
&+g\frac{2\pi}{\omega}P^{(s)}\Phi_{m,p}^{(dr)}+g\frac{2\pi}{\omega}E^{(s)}(\xi_i)\,\Phi_p^{(sr)}\\
&-\frac{\pi}{\omega}\sum_{m=1}^{M+N}\left\{\left(U_m^{(0)}(\xi_i)\,A_q^{(s)}+U_{m,q}^{(s)}(\xi_i)\,A^{(0)}\right)+\sum_{k=1}^{K}\sum_{j=1}^{K}\left(U_{m,k}^{(c)}(\xi_i)\,A_j^{(s)}T_{k,j,q}^{(css)}+U_{m,k}^{(s)}(\xi_i)\,A_j^{(c)}T_{k,j,q}^{(scs)}\right)\right\}\Phi_{m,p}^{(mix)}\\
&-A_h\frac{2\pi}{\omega}\sum_{m=1}^{M+N}\Bigg\{U_m^{(s)}(\xi_{i-1})\left(-\frac{1}{2\Delta\xi}\Phi_{m,p}^{(difx)}+\frac{1}{\Delta\xi^2}\Phi_{m,p}^{(icd)}\right)+U_m^{(s)}(\xi_i)\left(\Phi_{m,p}^{(dif)}-\frac{2}{\Delta\xi^2}\Phi_{m,p}^{(icd)}\right)\\
&\qquad\qquad+U_m^{(s)}(\xi_{i+1})\left(\frac{1}{2\Delta\xi}\Phi_{m,p}^{(difx)}+\frac{1}{\Delta\xi^2}\Phi_{m,p}^{(icd)}\right)\Bigg\}\\
&=0\qquad\text{for } p=1\ldots M
\end{aligned}
\tag{F.15}
$$

Wind, cross-channel, test function $\sin(q\omega t)$

$$
\frac{\pi}{\omega}\left(U_{M+1}^{(0)}(\xi_i)A_q^{(s)}+U_{M+1,q}^{(s)}(\xi_i)A^{(0)}\right)+\frac{\pi}{\omega}\sum_{k=1}^{K}\sum_{j=1}^{K}\left(U_{M+1,k}^{(c)}(\xi_i)A_j^{(s)}T_{k,j,q}^{(css)}+U_{M+1,k}^{(s)}(\xi_i)A_j^{(c)}T_{k,j,q}^{(scs)}\right)=0
\tag{F.16}
$$

Gibbs Effect, cross-channel, test function $\sin(q\omega t)$

$$
\begin{aligned}
&\frac{\pi}{\omega}\frac{1}{h^2}\left(\left(U_{M+2}^{(0)}(\xi_i)\,A_q^{(s)}+U_{M+2,q}^{(s)}(\xi_i)\,A^{(0)}\right)+\sum_{k=1}^{K}\sum_{j=1}^{K}\left(U_{M+2,k}^{(c)}(\xi_i)\,A_j^{(s)}T_{k,j,q}^{(css)}+U_{M+2,k}^{(s)}(\xi_i)\,A_j^{(c)}T_{k,j,q}^{(scs)}\right)\right)\\
&+\frac{\pi}{\omega}\frac{g}{w(0)}E_q^{(s)}(\xi_i)+\frac{\pi}{\omega}\frac{gh}{w(0)}P_q^{(s)}(\xi_i)\\
&-\frac{\pi}{\omega}\frac{A_h}{w(0)}\sum_{m=1}^{M+N}\left(U_{m,q}^{(s)}(\xi_i)\,\Phi_m^{(grx)}+\frac{1}{2\Delta\xi}\left(-U_{m,q}^{(s)}(\xi_{i-1})+U_{m,q}^{(s)}(\xi_{i+1})\right)\Phi_m^{(gr)}\right)=0
\end{aligned}
\tag{F.17}
$$

Momentum Equation, along-channel, test function $\sin(q\omega t)$

$$
\begin{aligned}
&\sum_{m=1}^{M+N}q\pi V_{m,q}^{(c)}\Phi_{m,q}^{(icd)}\\
&-\frac{\pi}{\omega}\frac{1}{2\Delta\xi}\sum_{m=1}^{M+N}\sum_{n=1}^{M+N}\Bigg\{\left(V_m^{(0)}(\xi_{i-1})\,U_{n,q}^{(s)}(\xi_i)+V_{m,q}^{(s)}(\xi_{i-1})\,U_n^{(0)}(\xi_i)\right)\\
&\qquad\qquad+\sum_{k=1}^{K}\sum_{j=1}^{K}\left(V_{m,k}^{(c)}(\xi_{i-1})\,U_{n,j}^{(s)}(\xi_i)\,T_{k,j,q}^{(css)}+V_{m,k}^{(s)}(\xi_{i-1})\,U_{n,j}^{(c)}(\xi_i)\,T_{k,j,q}^{(scs)}\right)\Bigg\}\Phi_{m,n,p}^{(arx)}
\end{aligned}
$$

$$
\begin{aligned}
&+\frac{\pi}{\omega}\frac{1}{2\Delta\xi}\sum_{m=1}^{M+N}\sum_{n=1}^{M+N}\Bigg\{\left(V_m^{(0)}(\xi_i)\,U_{n,q}^{(s)}(\xi_i)+V_{m,q}^{(s)}(\xi_i)\,U_n^{(0)}(\xi_i)\right)\\
&\qquad+\sum_{k=1}^{K}\sum_{j=1}^{K}\left(V_{m,k}^{(c)}(\xi_i)\,U_{n,j}^{(s)}(\xi_i)\,T_{k,j,q}^{(css)}+V_{m,k}^{(s)}(\xi_i)\,U_{n,j}^{(c)}(\xi_i)\,T_{k,j,q}^{(scs)}\right)\Bigg\}\Phi_{m,n,p}^{(ar)}\\
&+\frac{\pi}{\omega}\frac{1}{2\Delta\xi}\sum_{m=1}^{M+N}\sum_{n=1}^{M+N}\Bigg\{\left(V_m^{(0)}(\xi_{i+1})\,U_{n,q}^{(s)}(\xi_i)+V_{m,q}^{(s)}(\xi_{i+1})\,U_n^{(0)}(\xi_i)\right)\\
&\qquad+\sum_{k=1}^{K}\sum_{j=1}^{K}\left(V_{m,k}^{(c)}(\xi_{i+1})\,U_{n,j}^{(s)}(\xi_i)\,T_{k,j,q}^{(css)}+V_{m,k}^{(s)}(\xi_{i+1})\,U_{n,j}^{(c)}(\xi_i)\,T_{k,j,q}^{(scs)}\right)\Bigg\}\Phi_{m,n,p}^{(arx)}\\
&-\frac{\pi}{\omega}\frac{1}{2\Delta\xi}\sum_{m=1}^{M+N}\sum_{n=1}^{M+N}\Bigg\{\left(V_m^{(0)}(\xi_i)\,U_{n,q}^{(s)}(\xi_{i-1})+V_{m,q}^{(s)}(\xi_i)\,U_n^{(0)}(\xi_{i-1})\right)\\
&\qquad+\sum_{k=1}^{K}\sum_{j=1}^{K}\left(V_{m,k}^{(c)}(\xi_i)\,U_{n,j}^{(s)}(\xi_{i-1})\,T_{k,j,q}^{(css)}+V_{m,k}^{(s)}(\xi_i)\,U_{n,j}^{(c)}(\xi_{i-1})\,T_{k,j,q}^{(scs)}\right)\Bigg\}\Phi_{m,n,p}^{(azx)}\\
&+\frac{\pi}{\omega}\frac{1}{2\Delta\xi}\sum_{m=1}^{M+N}\sum_{n=1}^{M+N}\Bigg\{\left(V_m^{(0)}(\xi_i)\,U_{n,q}^{(s)}(\xi_i)+V_{m,q}^{(s)}(\xi_i)\,U_n^{(0)}(\xi_i)\right)\\
&\qquad+\sum_{k=1}^{K}\sum_{j=1}^{K}\left(V_{m,k}^{(c)}(\xi_i)\,U_{n,j}^{(s)}(\xi_i)\,T_{k,j,q}^{(css)}+V_{m,k}^{(s)}(\xi_i)\,U_{n,j}^{(c)}(\xi_i)\,T_{k,j,q}^{(scs)}\right)\Bigg\}\Phi_{m,n,p}^{(az)}\\
&+\frac{\pi}{\omega}\frac{1}{2\Delta\xi}\sum_{m=1}^{M+N}\sum_{n=1}^{M+N}\Bigg\{\left(V_m^{(0)}(\xi_i)\,U_{n,q}^{(s)}(\xi_{i+1})+V_{m,q}^{(s)}(\xi_i)\,U_n^{(0)}(\xi_{i+1})\right)\\
&\qquad+\sum_{k=1}^{K}\sum_{j=1}^{K}\left(V_{m,k}^{(c)}(\xi_i)\,U_{n,j}^{(s)}(\xi_{i+1})\,T_{k,j,q}^{(css)}+V_{m,k}^{(s)}(\xi_i)\,U_{n,j}^{(c)}(\xi_{i+1})\,T_{k,j,q}^{(scs)}\right)\Bigg\}\Phi_{m,n,p}^{(azx)}\\
&-\gamma\frac{2\pi}{\omega}\sum_{m=1}^{M+N}U_m^{(s)}(\xi_i)\,\Phi_{m,p}^{(icd)}\\
&-\frac{\pi}{\omega}\sum_{m=1}^{M+N}\sum_{n=1}^{M+N}\Bigg\{\left(V_m^{(0)}(\xi_i)\,U_{n,q}^{(s)}(\xi_i)+V_m^{(s)}(\xi_i)\,U_{n,q}^{(0)}(\xi_i)\right)\\
&\qquad+\sum_{k=1}^{K}\sum_{j=1}^{K}\left(V_{m,k}^{(c)}(\xi_i)\,U_{n,k}^{(s)}(\xi_i)\,T_{k,j,q}^{(css)}+V_{m,k}^{(s)}(\xi_i)\,U_{n,k}^{(c)}(\xi_i)\,T_{k,j,q}^{(scs)}\right)\Bigg\}\Phi_{m,n,p}^{(cur)}\\
&+g\frac{2\pi}{\omega}Y^{(s)}\Phi_{m,p}^{(dt)}+g\frac{2\pi}{\omega}H^{(s)}(\xi_i)\,\Phi_p^{(st)}\\
&-\frac{\pi}{\omega}\sum_{m=1}^{M+N}\left\{\left(V_m^{(0)}(\xi_i)\,A_q^{(s)}+V_{m,q}^{(s)}(\xi_i)\,A^{(0)}\right)+\sum_{k=1}^{K}\sum_{j=1}^{K}\left(V_{m,k}^{(c)}(\xi_i)\,A_j^{(s)}T_{k,j,q}^{(css)}+V_{m,k}^{(s)}(\xi_i)\,A_j^{(c)}T_{k,j,q}^{(scs)}\right)\right\}\Phi_{m,p}^{(mix)}\\
&-A_h\frac{2\pi}{\omega}\sum_{m=1}^{M+N}\Bigg\{V_m^{(s)}(\xi_{i-1})\left(-\frac{1}{2\Delta\xi}\Phi_{m,p}^{(difx)}+\frac{1}{\Delta\xi^2}\Phi_{m,p}^{(icd)}\right)+V_m^{(s)}(\xi_i)\left(\Phi_{m,p}^{(dif)}-\frac{2}{\Delta\xi^2}\Phi_{m,p}^{(icd)}\right)\\
&\qquad+V_m^{(s)}(\xi_{i+1})\left(\frac{1}{2\Delta\xi}\Phi_{m,p}^{(difx)}+\frac{1}{\Delta\xi^2}\Phi_{m,p}^{(icd)}\right)\Bigg\}\\
&=0\qquad\text{for } p=1\ldots M
\end{aligned}
\tag{F.18}
$$

Wind, along-channel, test function $\sin(q\omega t)$

$$\frac{\pi}{\omega}\left(V_{M+1}^{(0)}(\xi_i)A_q^{(s)} + V_{M+1,q}^{(s)}(\xi_i)A^{(0)}\right) + \frac{\pi}{\omega}\sum_{k=1}^{K}\sum_{j=1}^{K}\left(V_{M+1,k}^{(c)}(\xi_i)A_j^{(s)}T_{k,j,q}^{(css)} + V_{M+1,k}^{(s)}(\xi_i)A_j^{(c)}T_{k,j,q}^{(scs)}\right) = 0 \quad \text{(F.19)}$$

Gibbs Effect, along-channel, test function $\sin(q\omega t)$

$$\begin{aligned}&\frac{\pi}{\omega}\frac{1}{h^2}\left(\left(V_{M+2}^{(0)}(\xi_i)\,A_q^{(s)} + V_{M+2,q}^{(s)}(\xi_i)\,A^{(0)}\right) + \sum_{k=1}^{K}\sum_{j=1}^{K}\left(V_{M+2,k}^{(c)}(\xi_i)\,A_j^{(s)}T_{k,j,q}^{(ccc)} + V_{M+2,k}^{(s)}(\xi_i)\,A_j^{(c)}T_{k,j,q}^{(ssc)}\right)\right)\\ &+\frac{\pi}{\omega}\frac{g}{w(0)}\frac{r_0}{r}H_q^{(s)} + \frac{\pi}{\omega}\frac{gh}{w(0)}\frac{r_0}{r}Y_q^{(s)}\\ &-\frac{\pi}{\omega}\frac{A_h}{w(0)}\sum_{m=1}^{M+N}\left(V_{m,q}^{(s)}(\xi_i)\,\Phi_m^{(grx)} + \frac{1}{2\Delta\xi}\left(-V_{m,q}^{(s)}(\xi_{i-1}) + V_{m,q}^{(s)}(\xi_{i+1})\right)\Phi_m^{(gr)}\right) = 0\end{aligned} \quad \text{(F.20)}$$

Rigid lid effect, test function $\sin(q\omega t)$

$$\frac{\pi}{\omega}\sum_{m=1}^{M+N}U_{m,q}^{(s)}(\xi_i)\Phi_m^{(q)} \quad \text{(F.21)}$$

F.2. Model equations for sediment

Concentration Equation, test function 1

$$\begin{aligned}&\frac{1}{\Delta\xi}\sum_{m=1}^{M+N}\left(C_m^{(0)}(\xi_{i+1}) - C_m^{(0)}(\xi_{i-1})\right)\Gamma_{m,p}^{(0)}\\ &+\frac{1}{2\Delta\xi}\sum_{m=1}^{M+N}\sum_{k=1}^{K}\left(\left(C_m^{(c)}(\xi_{i+1}) - C_m^{(c)}(\xi_{i-1})\right)\Gamma_{m,k,p}^{(c)} + \left(C_m^{(s)}(\xi_{i+1}) - C_m^{(s)}(\xi_{i-1})\right)\Gamma_{m,k,p}^{(s)}\right)\\ &+2\sum_{m=1}^{M+N}C_m^{(0)}(\xi_i)\,\Lambda_{m,p}^{(0)} + \sum_{m=1}^{M+N}\sum_{k=1}^{K}\left(C_{m,k}^{(c)}(\xi_i)\,\Lambda_{m,k,p}^{(c)} + C_{m,k}^{(s)}(\xi_i)\,\Lambda_{m,k,p}^{(s)}\right)\\ &+\frac{2}{\Delta\xi^2}D_h\sum_{m=1}^{M+N}\left(2C_m^{(0)}(\xi_i) - C_m^{(0)}(\xi_{i+1}) - C_m^{(0)}(\xi_{i-1})\right)\Psi_{m,p}^{(\mathrm{id})}\\ &=0\end{aligned} \quad \text{(F.22)}$$

Surface Boundary Condition, test function 1

$$2w_s\sum_{m=1}^{M}(-1)^m C_m^{(0)} - w_s C_{M+2}^{(0)} - \frac{\pi c_n}{h}\left(2D^{(0)}C_{M+1}^{(0)} + \sum_{k=1}^{K}\left(C_{M+1,k}^{(c)}D_k^{(c)} + C_{M+1,k}^{(s)}D_k^{(s)}\right)\right) = 0 \quad \text{(F.23)}$$

Bottom Boundary Condition, test function 1

$$-\frac{c_n}{h}\sum_{m=M+1}^{M+N}\left(2C_m^{(0)}D^{(0)} + \sum_{k=1}^{K}C_{m,k}^{(c)}D_k^{(c)} + C_{m,k}^{(s)}D_k^{(s)}\right)\left(1-\delta_{m,M+1}(1-\pi)\right) = 2\alpha_s a(r)X^{(0)} \quad \text{(F.24)}$$

Concentration Equation, test function $\cos(q\omega t)$

$$\begin{aligned}
&\frac{1}{\Delta\xi}\sum_{m=1}^{M+N}\left(\left(C_m^{(0)}(\xi_{i+1})-C_m^{(0)}(\xi_{i-1})\right)\Gamma_{m,q,p}^{(c)}+\left(C_m^{(c)}(\xi_{i+1})-C_m^{(c)}(\xi_{i-1})\right)\Gamma_{m,p}^{(0)}\right)\\
&+\frac{1}{2\Delta\xi}\sum_{m=1}^{M+N}\sum_{k=1}^{K}\left(\left(C_m^{(c)}(\xi_{i+1})-C_m^{(c)}(\xi_{i-1})\right)\Gamma_{m,j,p}^{(c)}T_{k,j,q}^{(ccc)}+\left(C_m^{(s)}(\xi_{i+1})-C_m^{(s)}(\xi_{i-1})\right)\Gamma_{m,j,p}^{(s)}T_{k,j,q}^{(ssc)}\right)\\
&+2\sum_{m=1}^{M+N}\left(C_m^{(0)}(\xi_i)\Lambda_{m,q,p}^{(c)}+C_{m,q}^{(c)}(\xi_i)\Lambda_{m,p}^{(0)}\right)+\sum_{m=1}^{M+N}\sum_{k=1}^{K}\sum_{j=1}^{K}\left(C_{m,k}^{(c)}(\xi_i)\Lambda_{m,j,p}^{(c)}T_{k,j,q}^{(ccc)}+C_{m,k}^{(s)}(\xi_i)\Lambda_{m,j,p}^{(s)}T_{k,j,q}^{(ssc)}\right)\\
&+\delta_{k,q}\frac{1}{\Delta\xi^2}D_h\sum_{m=1}^{M+N}\left(2C_m^{(c)}(\xi_i)-C_m^{(c)}(\xi_{i+1})-C_m^{(c)}(\xi_{i-1})\right)\Psi_{m,p}^{(\mathrm{id})}\\
&=0
\end{aligned}\tag{F.25}$$

Surface Boundary Condition, test function $\cos(q\omega t)$

$$\begin{aligned}
&w_s\sum_{m=1}^{M}(-1)^m C_{m,q}^{(c)}-\frac{1}{2}w_s C_{M+2,q}^{(c)}\\
&-\frac{\pi c_n}{h}\left(C_{M+1}^{(0)}D_q^{(c)}+C_{M+1,q}^{(c)}D^{(0)}+\sum_{k=1}^{K}\sum_{j=1}^{K}\left(T_{k,j,q}^{(ccc)}C_{M+1,k}^{(c)}D_j^{(c)}+T_{kj,q}^{(ssc)}C_{M+1,k}^{(s)}D_j^{(s)}\right)\right)=0
\end{aligned}\tag{F.26}$$

Bottom Boundary Condition, test function $\cos(q\omega t)$

$$\begin{aligned}
&-\frac{c_\eta}{h}\sum_{m=M+1}^{M+N}\left(C_m^{(0)}D_q^{(c)}+C_{m,q}^{(c)}D^{(0)}+\sum_{k=1}^{K}\sum_{j=1}^{K}\left(T_{k,j,q}^{(ccc)}C_{m,k}^{(c)}D_k^{(c)}+T_{k,j,q}^{(ssc)}C_{m,k}^{(s)}D_k^{(s)}\right)\right)\left(1-\delta_{m,M+1}(1-\pi)\right)\\
&=\alpha_s a(r)X_q^{(c)}
\end{aligned}\tag{F.27}$$

Concentration Equation, test function $\sin(q\omega t)$

$$\begin{aligned}
&\frac{1}{\Delta\xi}\sum_{m=1}^{M+N}\left(\left(C_m^{(0)}(\xi_{i+1})-C_m^{(0)}(\xi_{i-1})\right)\Gamma_{m,q,p}^{(s)}+\left(C_m^{(s)}(\xi_{i+1})-C_m^{(s)}(\xi_{i-1})\right)\Gamma_{m,p}^{(0)}\right)\\
&+\frac{1}{2\Delta\xi}\sum_{m=1}^{M+N}\sum_{k=1}^{K}\left(\left(C_m^{(c)}(\xi_{i+1})-C_m^{(c)}(\xi_{i-1})\right)\Gamma_{m,j,p}^{(s)}T_{k,j,q}^{(css)}+\left(C_m^{(s)}(\xi_{i+1})-C_m^{(s)}(\xi_{i-1})\right)\Gamma_{m,j,p}^{(c)}T_{k,j,q}^{(scs)}\right)\\
&+2\sum_{m=1}^{M+N}\left(C_m^{(0)}(\xi_i)\Lambda_{m,q,p}^{(c)}+C_{m,q}^{(c)}(\xi_i)\Lambda_{m,p}^{(0)}\right)+\sum_{m=1}^{M+N}\sum_{k=1}^{K}\sum_{j=1}^{K}\left(C_{m,k}^{(c)}(\xi_i)\Lambda_{m,j,p}^{(s)}T_{k,j,q}^{(css)}+C_{m,k}^{(s)}(\xi_i)\Lambda_{m,j,p}^{(c)}T_{k,j,q}^{(scs)}\right)\\
&+\delta_{k,q}\frac{1}{\Delta\xi^2}D_h\sum_{m=1}^{M+N}\left(2C_m^{(c)}(\xi_i)-C_m^{(c)}(\xi_{i+1})-C_m^{(c)}(\xi_{i-1})\right)\Psi_{m,p}^{(\mathrm{id})}\\
&=0
\end{aligned}\tag{F.28}$$

Surface Boundary Condition, test function $\sin(q\omega t)$

$$w_s \sum_{m=1}^{M} (-1)^m C_{m,q}^{(s)} - \frac{1}{2} w_s C_{M+2,q}^{(s)} - \frac{\pi c_n}{h} \left(C_{M+1}^{(0)} D_q^{(s)} + C_{M+1,q}^{(s)} D^{(0)} + \sum_{k=1}^{K} \sum_{j=1}^{K} \left(T_{k,j,q}^{(css)} C_{M+1,k}^{(c)} D_j^{(s)} + T_{k,j,q}^{(scs)} C_{M+1,k}^{(s)} D_j^{(c)} \right) \right) = 0 \tag{F.29}$$

Bottom Boundary Condition, test function $\sin(q\omega t)$

$$- \frac{c_\eta}{h} \sum_{m=M+1}^{M+N} \left(C_m^{(0)} D_q^{(s)} + C_{m,q}^{(s)} D^{(0)} + \sum_{k=1}^{K} \sum_{j=1}^{K} \left(T_{kj,q}^{(css)} C_{m,k}^{(c)} D_k^{(s)} + T_{k,j,q}^{(scc)} C_{m,k}^{(s)} D_k^{(c)} \right) \right) \left(1 - \delta_{m,M+1}(1-\pi)\right) = \alpha_s a(r) X_q^{(s)} \tag{F.30}$$

F.3. Model equations at the side walls

The equations in the previous section are valid for the locations ξ_2-ξ_{L-1}. At the side walls, locations ξ_1 and ξ_L, different model equations must hold to meet the boundary conditions.

For the flow, it was imposed that u_r and u_θ must be 0 at the side walls. Therefore all variables U_m and V_m must be 0 at the first and last point along the transect. Furthermore, E is assumed to be 0 at these boundaries.

For the concentration, the derivative of c to r must be 0 at the side walls. Expressing C_m as a sum of tidal components and applying the Galerkin method to equation (E.46) leads to the equations that hold at the side walls. For ξ_1 this results in the following equations for test function 1, $\cos(k\omega t)$ and $\sin(k\omega t)$,

$$\sum_{m=1}^{M+N} C_m^{(0)}(\xi_1) \left(-\frac{1}{\Delta\xi} \Psi_{m,p}^{(id)} + \Psi_{m,p}^{(bnd)} \right) + \frac{1}{\Delta\xi} C_m^{(0)}(\xi_2) \Psi_{m,p}^{(id)} = 0, \tag{F.31}$$

$$\sum_{m=1}^{M+N} C_{m,q}^{(c)}(\xi_1) \left(-\frac{1}{\Delta\xi} \Psi_{m,p}^{(id)} + \Psi_{m,p}^{(bnd)} \right) + \frac{1}{\Delta\xi} C_{m,q}^{(c)}(\xi_2) \Psi_{m,p}^{(id)} = 0, \tag{F.32}$$

$$\sum_{m=1}^{M+N} C_{m,q}^{(s)}(\xi_1) \left(-\frac{1}{\Delta\xi} \Psi_{m,p}^{(id)} + \Psi_{m,p}^{(bnd)} \right) + \frac{1}{\Delta\xi} C_{m,q}^{(s)}(\xi_2) \Psi_{m,p}^{(id)} = 0, \tag{F.33}$$

for $p = 1 \ldots M$. Moreover, for $m = M+1$ and $m = M+2$,

$$C_m^{(0)}(\xi_1) - C_m^{(0)}(\xi_2) = 0, \tag{F.34}$$

$$C_{m,q}^{(c)}(\xi_1) - C_{m,q}^{(c)}(\xi_2) = 0, \tag{F.35}$$

$$C_{m,q}^{(s)}(\xi_1) - C_{m,q}^{(s)}(\xi_2) = 0, \tag{F.36}$$

must hold.

Similarly, at ξ_L, the model equations are for test function 1, $\cos(k\omega t)$ and $\sin(k\omega t)$,

$$\sum_{m=1}^{M+N} C_m^{(0)}(\xi_L) \left(\frac{1}{\Delta\xi} \Psi_{m,p}^{(id)} + \Psi_{m,p}^{(bnd)} \right) - \frac{1}{\Delta\xi} C_m^{(0)}(\xi_{L-1}) \Psi_{m,p}^{(id)} = 0, \tag{F.37}$$

$$\sum_{m=1}^{M+N} C_{m,q}^{(c)}(\xi_L) \left(\frac{1}{\Delta\xi} \Psi_{m,p}^{(id)} + \Psi_{m,p}^{(bnd)} \right) - \frac{1}{\Delta\xi} C_{m,q}^{(c)}(\xi_{L-1}) \Psi_{m,p}^{(id)} = 0, \tag{F.38}$$

$$\sum_{m=1}^{M+N} C_{m,q}^{(s)}(\xi_L)\left(\frac{1}{\Delta\xi}\Psi_{m,p}^{(id)} + \Psi_{m,p}^{(bnd)}\right) - \frac{1}{\Delta\xi}C_{m,q}^{(s)}(\xi_{L-1})\,\Psi_{m,p}^{(id)} = 0, \tag{F.39}$$

for $p = 1 \ldots M$ and for $m = M+1$ and $m = M+2$,

$$C_m^{(0)}(\xi_L) - C_m^{(0)}(\xi_{L-1}) = 0, \tag{F.40}$$

$$C_{m,q}^{(c)}(\xi_L) - C_{m,q}^{(c)}(\xi_{L-1}) = 0, \tag{F.41}$$

$$C_{m,q}^{(s)}(\xi_L) - C_{m,q}^{(s)}(\xi_{L-1}) = 0. \tag{F.42}$$

F.4. Coefficients

Coefficients Φ

$$\Phi_{m,p}^{(icd)} = \int_0^1 f_m f_p \,\mathrm{d}\sigma \tag{F.43}$$

$$\Phi_{m,n,p}^{(ar)} = \int_0^1 \left(\frac{\partial f_m}{\partial \xi} + \frac{\partial f_m}{\partial \sigma}\frac{\partial \sigma}{\partial r}\right) f_n f_p \,\mathrm{d}\sigma \tag{F.44}$$

$$\Phi_{m,n,p}^{(arx)} = \int_0^1 f_m f_n f_p \,\mathrm{d}\sigma \tag{F.45}$$

$$\Phi_{m,n,p}^{(az)} = -\int_0^1 \frac{\partial f_m}{\partial \sigma}\int_\sigma^1 \left(\frac{\partial f_n}{\partial \xi} + \frac{\partial f_n}{\partial \sigma'}\frac{\partial \sigma'}{\partial r} + \frac{f_n}{r}\right)\mathrm{d}\sigma' f_p \,\mathrm{d}\sigma \tag{F.46}$$

$$\Phi_{m,n,p}^{(azx)} = -\int_0^1 \frac{\partial f_m}{\partial \sigma}\int_\sigma^1 f_n \,\mathrm{d}\sigma' f_p \,\mathrm{d}\sigma \tag{F.47}$$

$$\Phi_{m,n,p}^{(cur)} = \frac{1}{r}\int_0^1 f_m f_n f_p \,\mathrm{d}\sigma \tag{F.48}$$

$$\Phi_p^{(dr)} = h\int_0^1 (1-\sigma) f_p \,\mathrm{d}\sigma \tag{F.49}$$

$$\Phi_p^{(dt)} = h\frac{r_0}{r}\int_0^1 (1-\sigma) f_p \,\mathrm{d}\sigma \tag{F.50}$$

$$\Phi_p^{(sr)} = \int_0^1 f_p \,\mathrm{d}\sigma \tag{F.51}$$

$$\Phi_p^{(st)} = \frac{r_0}{r}\int_0^1 f_p \,\mathrm{d}\sigma \tag{F.52}$$

$$\Phi_m^{(q)} = \int_0^1 f_m \,\mathrm{d}\sigma \tag{F.53}$$

$$\Phi_{m,p}^{(mix)} = \frac{1}{h^2}\int_0^1 \frac{\partial}{\partial \sigma}\left(\phi\frac{\partial f_m}{\partial \sigma}\right) f_p \,\mathrm{d}\sigma = \begin{cases} -\left(p-\frac{1}{2}\right)^2 \frac{\pi^2}{h^2}\int_0^1 f_p^2 w \,\mathrm{d}\sigma & ; \quad m = p \\ -\frac{\pi^2}{h^2}\int_0^1 f_{M+1} w f_p \,\mathrm{d}\sigma & ; \quad m = M+1 \\ -\frac{1}{h^2}\int_0^1 w f_p \,\mathrm{d}\sigma & ; \quad m = M+2 \\ 0 & ; \quad \text{otherwise} \end{cases} \tag{F.54}$$

$$\Phi_{m,p}^{(dif)} = \int_0^1 \left(\frac{1}{r}\frac{\partial f_m}{\partial \xi} + \frac{\partial^2 f_m}{\partial \xi^2} + 2\frac{\partial \sigma}{\partial r}\frac{\partial}{\partial \sigma}\left(\frac{\partial f_m}{\partial \xi}\right) + \left(\frac{\partial \sigma}{\partial r}\right)^2 \frac{\partial^2 f_m}{\partial \sigma^2} + \left(\frac{\partial^2 \sigma}{\partial r^2} + \frac{1}{r}\frac{\partial \sigma}{\partial r}\right)\frac{\partial f_m}{\partial \sigma}\right) f_p \,\mathrm{d}\sigma \tag{F.55}$$

$$\Phi_{m,p}^{(difx)} = \int_0^1 \left(\frac{f_m}{r} + 2\frac{\partial f_m}{\partial \xi} + 2\frac{\partial \sigma}{\partial r}\frac{\partial f_m}{\partial \sigma}\right) f_p \,\mathrm{d}\sigma \tag{F.56}$$

$$\Phi_m^{(grx)} = \left(2\frac{\partial\sigma}{\partial r}\frac{\partial}{\partial\sigma}\left(\frac{\partial f_m}{\partial\xi}\right) + \left(\frac{\partial\sigma}{\partial r}\right)^2 \frac{\partial^2 f_m}{\partial\sigma^2} + \left(\frac{\partial^2\sigma}{\partial r^2} + \frac{1}{r}\frac{\partial\sigma}{\partial r}\right)\frac{\partial f_m}{\partial\sigma}\right)\Bigg|_{\sigma=0} \tag{F.57}$$

$$\Phi_m^{(gr)} = 2\frac{\partial\sigma}{\partial r}\frac{\partial f_m}{\partial\sigma}\Bigg|_{\sigma=0} \tag{F.58}$$

Coefficients Ψ

$$\Psi_{m,p}^{(id)} = \int_0^1 d_m d_p \,\mathrm{d}\sigma \tag{F.59}$$

$$\Psi_{m,n,p}^{(az)} = -\int_0^1 \frac{\partial d_m}{\partial\sigma}\int_\sigma^1 \left(\frac{\partial f_n}{\partial\xi} + \frac{\partial f_n}{\partial\sigma'}\frac{\partial\sigma'}{\partial r} + \frac{f_n}{r}\right)\mathrm{d}\sigma' d_p \,\mathrm{d}\sigma \tag{F.60}$$

$$\Psi_{m,n,p}^{(ar)} = \int_0^1 \left(\frac{\partial d_m}{\partial\xi} + \frac{\partial d_m}{\partial\sigma}\frac{\partial\sigma}{\partial r} + \frac{d_m}{r}\right) f_n d_p \,\mathrm{d}\sigma \tag{F.61}$$

$$\Psi_{m,n,p}^{(azx)} = -\int_0^1 \frac{\partial d_m}{\partial\sigma}\int_\sigma^1 f_n \,\mathrm{d}\sigma' d_p \,\mathrm{d}\sigma \tag{F.62}$$

$$\Psi_{m,n,p}^{(arx)} = \int_0^1 d_m f_n d_p \,\mathrm{d}\sigma \tag{F.63}$$

$$\Psi_{m,p}^{(ws)} = \frac{1}{h}\int_0^1 \frac{\partial d_m}{\partial\sigma} d_p \,\mathrm{d}\sigma \tag{F.64}$$

$$\Psi_{m,p}^{(mix)} = \frac{1}{h^2}\int_0^1 \frac{\partial}{\partial\sigma}\left(\phi\frac{\partial d_m}{\partial\sigma}\right) d_p \,\mathrm{d}\sigma = \begin{cases} 0 & ; \quad m = p = 1 \\ -\frac{1}{h^2}\frac{1}{2}(p-1)^2\pi^2 c_\eta^2 & ; \quad m = p \quad \wedge \quad p = 2 \dots M \\ \frac{\pi^2}{h^2}\frac{\pi c_\eta^2}{p(2-p)}((-1)^p - 1) & ; \quad m = M+1 \quad \wedge \quad p = 1 \dots M \\ -\frac{1}{h^2}c_\eta^2 & ; \quad m = M+2 \quad \wedge \quad p = 1 \\ 0 & ; \quad m = M+2 \quad \wedge \quad p = 2 \dots M \end{cases} \tag{F.65}$$

$$\Psi_{m,p}^{(dif)} = \int_0^1 \left(\frac{1}{r}\frac{\partial d_m}{\partial\xi} + \frac{\partial^2 d_m}{\partial\xi^2} + 2\frac{\partial\sigma}{\partial r}\frac{\partial}{\partial\sigma}\left(\frac{\partial d_m}{\partial\xi}\right) + \left(\frac{\partial\sigma}{\partial r}\right)^2\frac{\partial^2 d_m}{\partial\sigma^2} + \left(\frac{\partial^2\sigma}{\partial r^2} + \frac{1}{r}\frac{\partial\sigma}{\partial r}\right)\frac{\partial d_m}{\partial\sigma}\right) d_p \,\mathrm{d}\sigma \tag{F.66}$$

$$\Psi_{m,p}^{(difx)} = \int_0^1 \left(\frac{d_m}{r} + 2\frac{\partial d_m}{\partial\xi} + 2\frac{\partial\sigma}{\partial r}\frac{\partial d_m}{\partial\sigma}\right) d_p \,\mathrm{d}\sigma \tag{F.67}$$

$$\Psi_{m,p}^{(bnd)} = \int_0^1 \frac{\partial d_m}{\partial\sigma}\frac{\partial\sigma}{\partial r} d_p \,\mathrm{d}\sigma \tag{F.68}$$

Coefficients T

$$T_{k,j,q}^{(ccc)} = \frac{\omega}{\pi}\int_{-\pi/\omega}^{\pi/\omega} \cos k\omega t \cos j\omega t \cos q\omega t \,\mathrm{d}t \tag{F.69}$$

$$T_{k,j,q}^{(ccs)} = \frac{\omega}{\pi}\int_{-\pi/\omega}^{\pi/\omega} \cos k\omega t \cos j\omega t \sin q\omega t \,\mathrm{d}t \tag{F.70}$$

$$T_{k,j,q}^{(csc)} = \frac{\omega}{\pi}\int_{-\pi/\omega}^{\pi/\omega} \cos k\omega t \sin j\omega t \cos q\omega t \,\mathrm{d}t \tag{F.71}$$

$$T_{k,j,q}^{(css)} = \frac{\omega}{\pi}\int_{-\pi/\omega}^{\pi/\omega} \cos k\omega t \sin j\omega t \sin q\omega t \,\mathrm{d}t \tag{F.72}$$

$$T_{k,j,q}^{(scc)} = \frac{\omega}{\pi} \int_{-\pi/\omega}^{\pi/\omega} \sin k\omega t \cos j\omega t \cos q\omega t \, \mathrm{d}t \tag{F.73}$$

$$T_{k,j,q}^{(scs)} = \frac{\omega}{\pi} \int_{-\pi/\omega}^{\pi/\omega} \sin k\omega t \cos j\omega t \sin q\omega t \, \mathrm{d}t \tag{F.74}$$

$$T_{k,j,q}^{(ssc)} = \frac{\omega}{\pi} \int_{-\pi/\omega}^{\pi/\omega} \sin k\omega t \sin j\omega t \cos q\omega t \, \mathrm{d}t \tag{F.75}$$

$$T_{k,j,q}^{(sss)} = \frac{\omega}{\pi} \int_{-\pi/\omega}^{\pi/\omega} \sin k\omega t \sin j\omega t \sin q\omega t \, \mathrm{d}t \tag{F.76}$$

indices	ccc	ccs	csc	css	scc	scs	ssc	sss
$k, j, q = 0$	2	0	0	0	0	0	0	0
$k = 0$ and $(j = \pm q; j, q \neq 0)$	1	0	0	±1	0	0	0	0
$j = 0$ and $(k = \pm q; k, q \neq 0)$	1	0	0	0	0	±1	0	0
$q = 0$ and $(j = \pm k; k, j \neq 0)$	1	0	0	0	0	0	±1	0
$k, j, q \neq 0$ and $k + j + q = 0$	$1/2$	0	0	$-1/2$	0	$-1/2$	$-1/2$	0
$k, j, q \neq 0$ and $k + j - q = 0$	$1/2$	0	0	$1/2$	0	$1/2$	$-1/2$	0
$k, j, q \neq 0$ and $k - j + q = 0$	$1/2$	0	0	$1/2$	0	$-1/2$	$1/2$	0
$k, j, q \neq 0$ and $k - j - q = 0$	$1/2$	0	0	$-1/2$	0	$1/2$	$1/2$	0

Table F.1: A table with the values of each coeffficient T for varying k, j and q.

G

Structure of Jacobi matrix

In Chapter 3 is explained that the Jacobi matrix of the model equations is required to solve the system of equations. Since there is a large number of model equations and unknown variables for each location along the transect, it is necessary to have a clear ordering in this matrix. This appendix explains how the Jacobi matrix is set up.

The ordering of the Jacobi matrix starts by the order of the model equations. The model equations are primary ordered by location, so first ξ_1, then ξ_2 and so on until ξ_L. Next, the equations are ordered by test function, so first the equations for test function 1, then $\cos(\omega t)$, next $\sin(\omega t)$, after that $\cos(2\omega t)$ and last $\sin(2\omega t)$. If K were larger than two, this would continue in the same way for higher values of K. Finally, for one location and test function, the equations for the flow are arranged as

- Momentum equation, cross-channel for $m = 1 \ldots M$
- Wind equation, cross-channel
- Gibbs effect equation, cross-channel
- Momentum equation, along-channel, for $m = 1 \ldots M$
- Wind equation, along-channel
- Gibbs effect equation, along-channel
- Rigid lid equation

and for the concentration as

- Concentration equation, for $m = 1 \ldots M$
- Surface boundary equation
- Bottom boundary equation

For the vector of unknowns a similar ordering is used. So at first the unknowns for ξ_1, then ξ_2 and so on till ξ_L. Next, the unknowns are ordered by the tidal component, first the variables for M_0, then the M_2 cosine variables followed by the M_2 sine variables, next the M_4 cosine variables and finally the M_4 sine variables. If more tidal components were included, these would follow afterwards in the same way. Within the same location and tidal component, the vector of unknowns for the flow first contains the cross-channel variable U_m for $m = 1 \ldots M + N$, then the along-channel variables V_m for $m = 1 \ldots M + N$ and last the variable E. For the concentration, after ordering by location and tidal component, the variables C_m are simply ordered by ascending m from 1 till $M + N$.

As a result of this ordering, the Jacobi matrix has a clear structure. It contains $L \times L$ blocks with $((2K+1)(2(M+N)+1)) \times ((2K+1)(2(M+N)+1))$ elements for the flow or $((2K+1)(M+N)) \times ((2K+1)(M+N))$ elements for the concentration. The block (i, j) contains the derivatives of the model equations for ξ_i with respect to the variables for location ξ_j. As can be seen in Appendix F, the model equations only

contain variables for ξ_{i-1}, ξ_i and ξ_{i+1}. This is due to the use of the finite difference approximation in the radial direction. Consequently, for every i, only the blocks $(i, i-1)$, (i, i) and $(i, i+1)$ contain nonzero elements. As a result, the Jacobi matrix can be characterised as a block-tridiagonal matrix.

Within one block another clear structure is visible. Each block contains $(2K+1) \times (2K+1)$ sub-blocks with each $(2(M+N)+1) \times (2(M+N)+1)$ elements for the flow or $(M+N) \times (M+N)$ elements for the concentration. Each sub-block contains the derivatives of the model equations for one of the test functions with respect to the variables for one of the tidal components.

In Section F.3 of Appendix F is explained that different model equations are used at the side walls to meet the boundary conditions there. The Jacobi matrix is also different for these locations. Instead of three, only two blocks are used there. The blocks that would contain derivatives for variables outside the domain, so $(1, 0)$ and $(L, L+1)$, do not exist.

For the flow, all variables must be equal to zero at the boundaries. As a result, the blocks $(1, 1)$ and (L, L) are identity matrices and the blocks $(1, 2)$ and $(L, L-1)$ contain only zeros. For the concentration, the model equations contain variables for the location at the boundary and the location next to it. Therefore, the blocks $(1, 1)$, $(1, 2)$, $(L, L-1)$ and (L, L) all contain nonzero elements.

H

Other methods to compute the erosion coefficient

In chapters 2 and 3 it is explained how the erosion coefficient corresponding to the morphodynamic equilibrium is computed using a time integration method. During this project, some other methods to compute the erosion coefficient were tried. This appendix briefly discusses the methods that were tried and the problems encountered with these methods.

H.1. Differential equation methods

The first approach is inspired by the method used in [11]. Since a perturbation method is used there, it is easier to find the erosion coefficient, because in that case it is not necessary to use an iterative process. In the approach described in this section, iterations are required to find a solution for the erosion coefficient.

The suspended sediment concentration for the erosion coefficient $a(r)$, can be expressed as

$$c = a(r)\hat{c} + \tilde{c}, \tag{H.1}$$

with $\hat{c}$ the suspended sediment concentration for $a(r) = 1$. Substituting this into the morphodynamic equilibrium condition, equation (2.22), results in a differential equation for $a(r)$,

$$I_1(r)\frac{da(r)}{dr} + I_2(r)a(r) + I_3(r) = 0, \tag{H.2}$$

with

$$I_1(r) = \int_{-H}^{0} -D_v\langle\hat{c}\rangle \,\mathrm{d}z, \tag{H.3}$$

$$I_2(r) = \int_{-H}^{0} \langle u_r\hat{c}\rangle - D_v\frac{\partial\langle\hat{c}\rangle}{\partial r} \,\mathrm{d}z \tag{H.4}$$

$$I_3(r) = \int_{-H}^{0} \langle u_r\tilde{c}\rangle - D_v\frac{\partial\langle\tilde{c}\rangle}{\partial r} \,\mathrm{d}z. \tag{H.5}$$

By solving this differential equation, a distribution for the erosion coefficient $a(r)$ is found.

The iteration process to find $a(r)$ corresponding to the morphodynamic equilibrium starts with computing $\hat{c}$ and choosing an initial estimate for $a(r)$. The initial estimate is used to compute the concentration c. Next, $\tilde{c}$ is computed as $\tilde{c} = c - a(r)\hat{c}$. This is used to solve the differential equation (H.2) to find a new expression for $a(r)$. Now a new c and $\tilde{c}$ are computed, and so on. In this process $\tilde{c}$ should become smaller and once $\tilde{c}$ is below a chosen tolerance value, the solution is obtained.

To find the erosion coefficient corresponding to the the differential equation (H.2), the analytical solution of this equation is used. The analytical solution of the differential equation (H.2) is,

$$a(r) = \exp\left(-\int \frac{I_2}{I_1}\,\mathrm{d}r\right)\left[-\int \exp\left(\int\left(\frac{I_2}{I_1}\,\mathrm{d}r\right)\frac{I_3}{I_1}\right)\mathrm{d}r + C_1\right], \tag{H.6}$$

with C_1 an integration constant. This constant depends on the condition in equation (2.28). The anti-derivatives in this solution and integrals defining I_1, I_2 and I_3 are solved numerically. This is done using the composite trapezoidal rule.

A slightly different approach is to discard the $\tilde{c}$ and to compute $\hat{c}$ by dividing the concentration obtained for an erosion coefficient by this erosion coefficient. The process starts with an initial estimate for $a(r)$ and computing the corresponding concentration. This is used to compute $\hat{c}$ and then the differential equation is solved to find a new value for $a(r)$, etcetera.

In this method I_3 equals zero. This results in the analytical solution

$$a(r) = C_1 \exp\left(-\int \frac{I_2}{I_1}\,\mathrm{d}r\right). \tag{H.7}$$

The anti-derivative in the solution and integrals for I_1 and I_2 are again solved numerically by using the composite trapezoidal rule.

It is possible to circumvent the numerical approximation of anti-derivatives by transforming the differential equation to a matrix equation. To obtain a matrix equation I_1, I_2 and $a(r)$ are discretized. The discretization is similar as the discretization for the model equations in the horizontal direction. This means there are L uniformly distributed grid points used. The derivative of $a(r)$ with respect to r is expressed by a central finite difference approximation. This results in the system,

$$\begin{bmatrix} 1 & -1 & 0 & 0 & \dots & 0 \\ \frac{-1}{2\Delta r} I_1(r_2) & I_2(r_2) & \frac{1}{2\Delta r} I_1(r_2) & 0 & \dots & 0 \\ 0 & \frac{-1}{2\Delta r} I_1(r_3) & I_2(r_3) & \frac{1}{2\Delta r} I_1(r_3) & \dots & 0 \\ \vdots & \ddots & \ddots & \ddots & \ddots & \vdots \\ 0 & \dots & 0 & \frac{-1}{2\Delta r} I_1(r_{L-1}) & I_2(r_{L-1}) & \frac{1}{2\Delta r} I_1(r_{L-1}) \\ 1 & \dots & 1 & 1 & 1 & 1 \end{bmatrix} \begin{bmatrix} a(r_1) \\ a(r_2) \\ a(r_3) \\ \vdots \\ a(r_{L-1}) \\ a(r_L) \end{bmatrix} = \begin{bmatrix} 0 \\ 0 \\ 0 \\ \vdots \\ 0 \\ \frac{a_* B}{\Delta r} \end{bmatrix}. \tag{H.8}$$

The first row states that $a(r)$ must be equal in the first and second grid point. The last row is used to let the solution for $a(r)$ meet the condition (2.28). Different boundary conditions can be imposed by changing these lines. A benefit of this method is that there are no anti-derivatives with respect to r which have to be evaluated numerically. The integrals that define I_1 and I_2 are again computed using the composite trapezoidal rule.

Unfortunately, with the three approaches described above, the correct distribution for the erosion coefficient was not obtained. Even when the analytical solution is used as an initial estimate for $a(r)$, a correction for $a(r)$ is computed. Consequently, the model then iterates away from this solution. This shows that the analytical solution will never be obtained using this approach. An explanation for this behaviour could be that the method is not accurate enough. To investigate this further more accurate numerical approximations could be used and the number of grid points could be increased.

In the middle of the estuary the solution was generally good but closer to the boundaries there was a deviation from the equilibrium and the transport was unequal to zero. In [11] the boundary layer is not solved which could explain why these kind of problems were not encountered there.

H.2. Simple method

As long as only diffusive transport is taken into account, it is also possible to use that

$$\int_{-H}^{0} \frac{\partial \langle c \rangle}{\partial r}\,\mathrm{d}z = 0, \tag{H.9}$$

must hold in a morphodynamic equilibrium. Using Leibniz integral rule, this is equivalent to,

$$\frac{\partial}{\partial r}\int_{-H}^{0} \langle c \rangle\,\mathrm{d}z - \langle c(-H) \rangle \frac{\partial H}{\partial r} = 0. \tag{H.10}$$

As a result,

$$\int_{-H}^{0} \langle c \rangle \, \mathrm{d}z - \int \langle c(-H) \rangle \frac{\partial H}{\partial r} \, \mathrm{d}r, \tag{H.11}$$

must be constant in a morphodynamic equilibrium. Consequently, the new value for the erosion coefficient is found iteratively by dividing the old value for $a(r)$ by the expression in (H.11) and then scaling this.

Choosing the analytical solution as initial estimate for $a(r)$ resulted in an equilibrium when using this method. However, when starting with a different initial estimate for $a(r)$ the process converges very slow. It might be possible to increase the convergence. However, since this method only works for diffusive transport it is not the most suitable choice for further development.

H.3. Spline method

In this entirely different approach, splines are used. For $i = 1, 2, \ldots L$ the concentration is computed for $a(r_i) = 1$ and $a(r_j) = 0$ with $i \neq j$. Next, a linear combination of the computed concentrations is found for which the total concentration results in the tide averaged lateral transport being equal to 0. This linear combination is the distribution of $a(r)$ for a morphodynamic equilibrium, after scaling this results in the correct erosion coefficient.

The solution obtained with this method indeed resulted in a tidally averaged lateral transport equal to zero. However, the corresponding distribution of $a(r)$ is quickly oscillating and also contained negative values for a number of grid points. Since the total transport was zero, this is mathematically a correct solution for the problem but not a physically feasible one because the erosion coefficient cannot take negative values. Moreover, the occurrence of large differences in the erosion coefficient between neighbouring points is also unlikely. A more smooth solution for the erosion coefficient is expected.

If this method would be altered in such a way that only physically feasible solutions can be obtained, it would be a relatively quick solution. The concentration has to be computed L times at the start of the method but after this the erosion coefficient is obtained directly.

Results for density gradient with varying phase

This section contains the results for some of the experiments discussed in Section 4.1.4. It concerns the decomposition of the flow corresponding to the simulations for the varying phase of the M_2 tidal component of the density gradient. In these simulations the M_0 amplitude of the density gradient is equal to -10^{-4} kg/m^4 and the M_2 amplitude of the density gradient is equal to 10^{-2} kg/m^4. Figure I.1 shows the results for the M_2 phase equal to -0.5π, Figure I.2 shows the results for the M_2 phase equal to 0 and Figure I.3 shows the results for the M_2 phase equal to 0.5π.

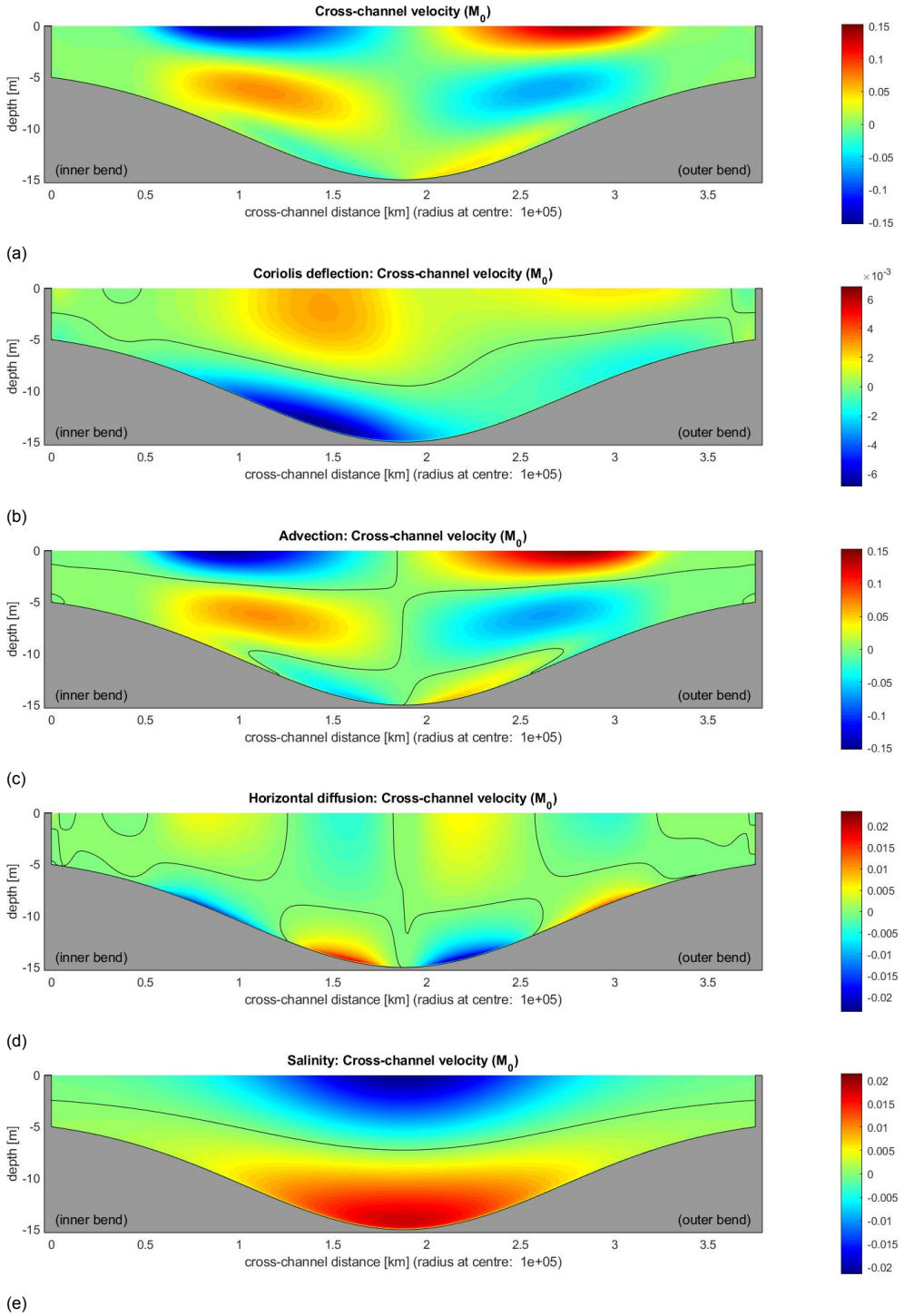

Figure I.1: The results for the cross-channel flow in m/s for an M_0 density gradient of 10^{-4} and an M_2 density gradient with amplitude 10^{-2} and phase -0.5π. The panels show the total residual flow (a) and the decomposition of the flow into the contributions for Coriolis deflection (b), advection (c), horizontal diffusion (d) and the density gradient (e).

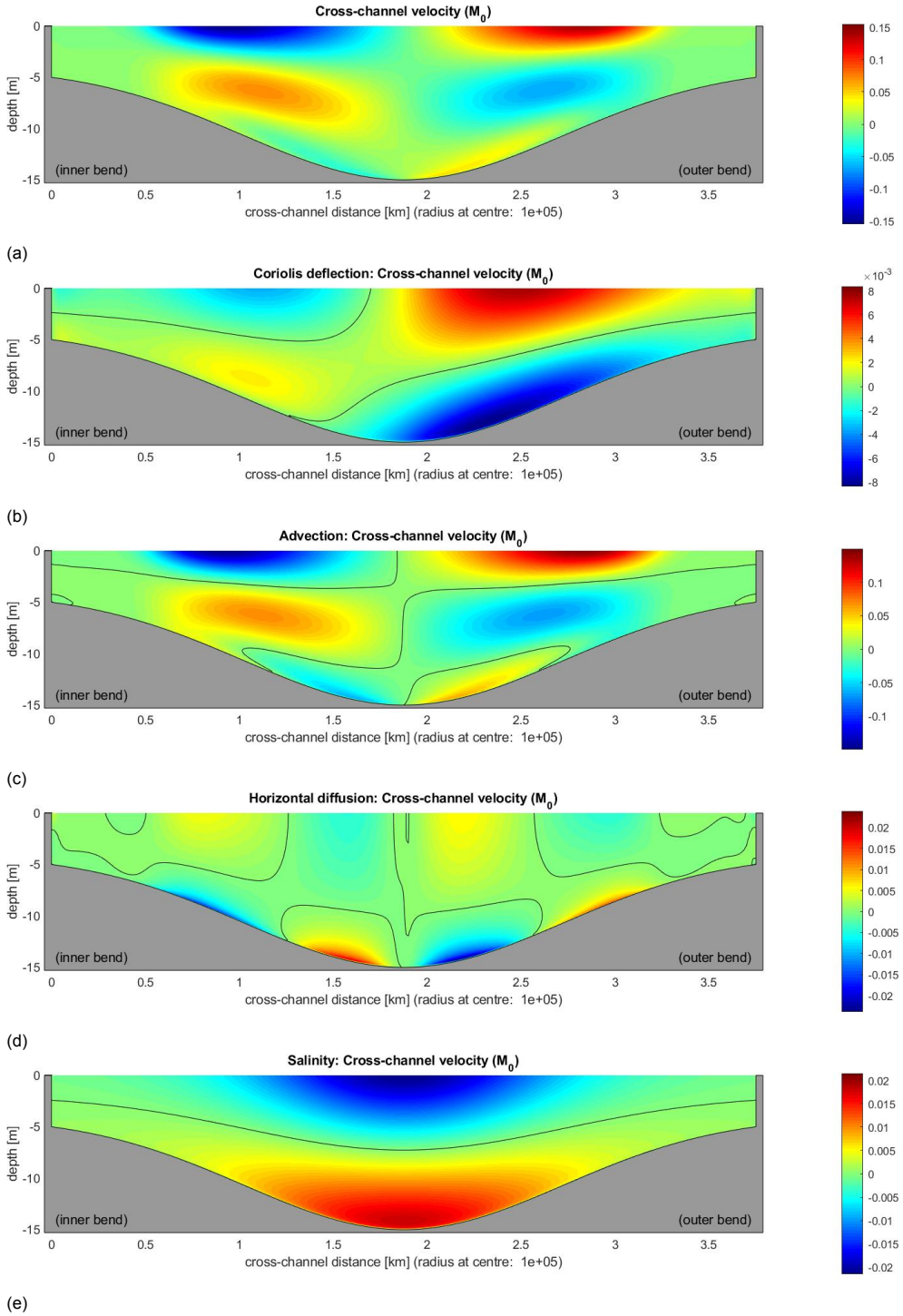

Figure I.2: The results for the cross-channel flow in m/s for an M_0 density gradient of 10^{-4} and an M_2 density gradient with amplitude 10^{-2} and phase 0. The panels show the total residual flow (a) and the decomposition of the flow into the contributions for Coriolis deflection (b), advection (c), horizontal diffusion (d) and the density gradient (e).

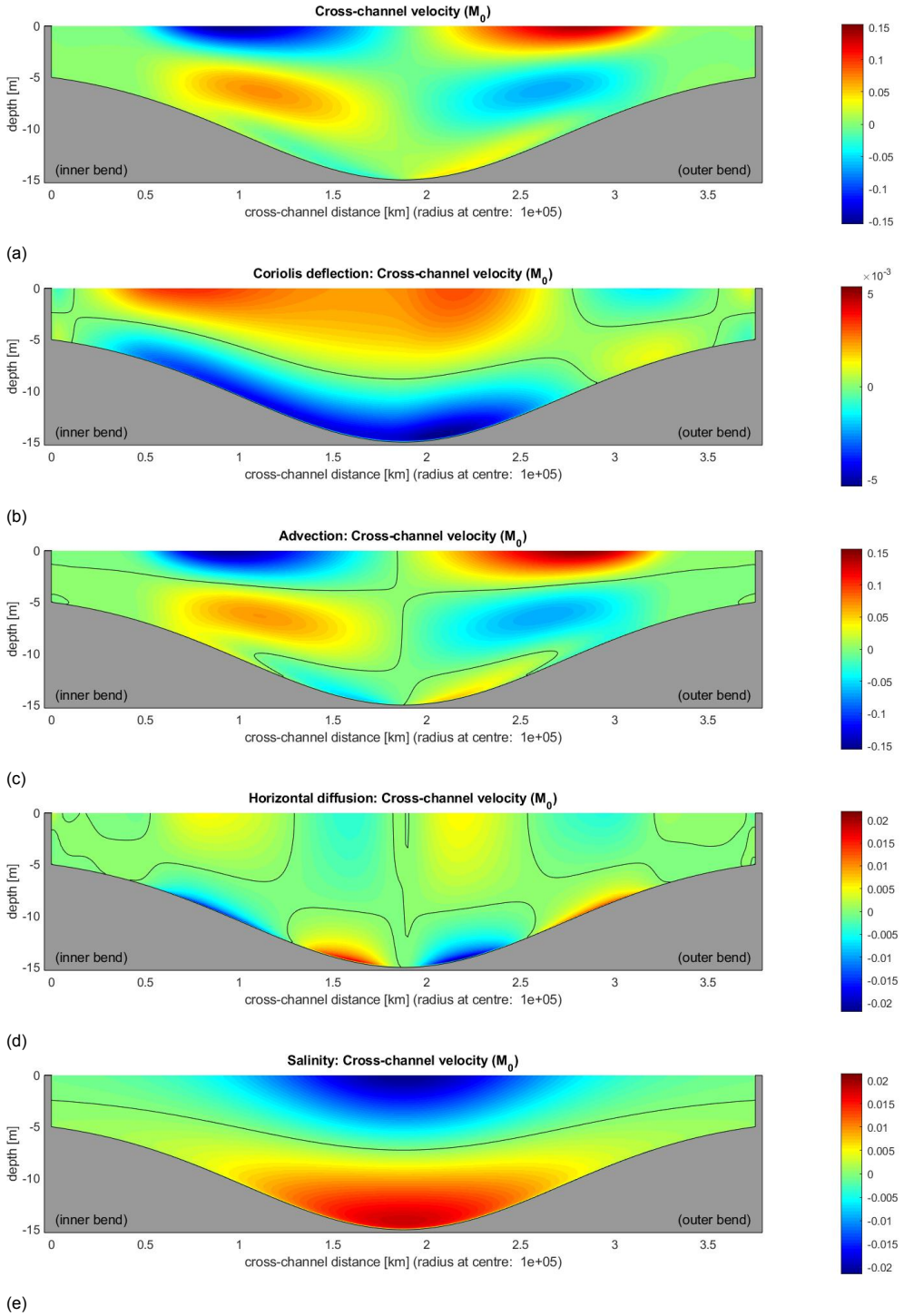

Figure I.3: The results for the cross-channel flow in m/s for an M_0 density gradient of 10^{-4} and an M_2 density gradient with amplitude 10^{-2} and phase 0.5π. The panels show the total residual flow (a) and the decomposition of the flow into the contributions for Coriolis deflection (b), advection (c), horizontal diffusion (d) and the density gradient (e).

Bibliography

[1] G. K. Batchelor. *An introduction to fluid dynamics*. Cambridge University Press, Cambridge, U.K, 1967. ISBN 9780521663960.

[2] W. E. Boyce and R. C. DiPrima. Elementary Differential Equations and Boundary Value Problems. In *Elementary Differential Equations and Boundary Value Problems*, chapter 11.2 Sturm, pages 685–699. Wiley, 10th edition, 2013. ISBN 9781118323618.

[3] H. Burchard. *Applied Turbulence Modelling in Marine Waters*. Springer-Verlag, Berlin Heidelberg, 2002. ISBN 9783540437956.

[4] P. Cheng and A. Valle-Levinson. Influence of lateral advection on residual currents in microtidal estuaries. *Journal of Physical Oceanography*, 39(12):3177–3190, 2009. doi: 10.1175/2009JPO4252.1.

[5] A. M. Davies. On extracting current profiles from vertically integrated numerical models. *Coastal Engineering*, 11(5-6):445–477, 1987. doi: 10.1016/0378-3839(87)90022-6.

[6] V. N. de Jonge. Tidal flow and residual flow in the Ems estuary. *Estuarine, Coastal and Shelf Science*, 34(1):1–22, 1992. doi: 10.1016/S0272-7714(05)80123-4.

[7] J. Dronkers and W. van Leussen. *Physical Processes in Estuaries*. Springer-Verlag, Berlin Heidelberg, 1988. ISBN 9783642736933.

[8] C. T. Friedrichs and J. M. Hamrick. Effects of channel geometry on cross sectional variations in along channel velocity in partially stratified estuaries. In *Buoyancy Effects on Coastal and Estuarine Dynamics*, pages 283–300. American Geophysical Union, Washington DC, 1996. doi: 10.1029/ce053p0283.

[9] A. E. Gill. *Atmosphere-Ocean Dynamics*. Academic Press, New York, 1982. ISBN 9780122835223.

[10] D. B. Haidvogel, H. G. Arango, K. Hedstrom, A. Beckmann, P. Malanotte-Rizzoli, and A. F. Shchepetkin. Model evaluation experiments in the North Atlantic Basin: Simulations in nonlinear terrain-following coordinates. *Dynamics of Atmospheres and Oceans*, 32(3-4):239–281, 2000. doi: 10.1016/S0377-0265(00)00049-X.

[11] K. M. H. Huijts, H. M. Schuttelaars, H. E. de Swart, and A. Valle-Levinson. Lateral entrapment of sediment in tidal estuaries: An idealized model study. *Journal of Geophysical Research: Oceans*, 111, 2006. doi: 10.1029/2006JC003615.

[12] K. M. H. Huijts, H. M. Schuttelaars, H. E. de Swart, and C. T. Friedrichs. Analytical study of the transverse distribution of along-channel and transverse residual flows in tidal estuaries. *Continental Shelf Research*, 29(1):89–100, 2009. doi: 10.1016/j.csr.2007.09.007.

[13] K. M. H. Huijts, H. E. De Swart, G. P. Schramkowski, and H. M. Schuttelaars. Transverse structure of tidal and residual flow and sediment concentration in estuaries: Sensitivity to tidal forcing and water depth. *Ocean Dynamics*, 61(8):1067–1091, 2011. doi: 10.1007/s10236-011-0414-7.

[14] S. J. Jordan. Introduction to Estuaries. In *Estuaries: Classification, Ecology and Human Impacts*, chapter 1, pages 1–13. Nova Science Publishers, 2012. ISBN 9781619420830.

[15] A. Kasai, A. E. Hill, T. Fujiwara, and J. H. Simpson. Effect of the Earth's rotation on the circulation in regions of freshwater influence. *Journal of Geophysical Research: Oceans*, 105(C7):16961–16969, 2000. doi: 10.1029/2000JC900058.

[16] K. Klingbeil, J. Becherer, E. Schulz, H. E. de Swart, H. M. Schuttelaars, A. Valle-Levinson, and H. Burchard. Thickness-weighted averaging in tidal estuaries and the vertical distribution of the eulerian residual transport. *Journal of Physical Oceanography*, 49(7):1809–1826, 2019. doi: 10.1175/JPO-D-18-0083.1.

[17] J. R. Koseff, J. K. Holen, S. G. Monismith, and J. E. Cloern. Coupled effects of vertical mixing and benthic grazing on phytoplankton populations in shallow, turbid estuaries. *Journal of Marine Research*, 51(4):843–868, 1993. doi: 10.1357/0022240933223954.

[18] J. A. Lerczak and W. R. Geyer. Modeling the lateral circulation in straight, stratified estuaries. *Journal of Physical Oceanography*, 34(6):1410–1428, 2004. doi: 10.1175/1520-0485(2004)034<1410:MTLCIS>2.0.CO;2.

[19] G. R. Lesser, J. A. Roelvink, J. A.T.M. van Kester, and G. S. Stelling. Development and validation of a three-dimensional morphological model. *Coastal Engineering*, 51(8-9):883–915, 2004. doi: 10.1016/j.coastaleng.2004.07.014.

[20] E. W. North, S. Y. Chao, L. P. Sanford, and R. R. Hood. The influence of wind and river pulses on an estuarine turbidity maximum: Numerical studies and field observations in Chesapeake Bay. *Estuaries*, 27(1):132–146, 2004. doi: 10.1007/BF02803567.

[21] University of Hawai'i. Circulation in Marginal Seas and Estuaries, 2020, accessed on 16-11-2020. URL https://manoa.hawaii.edu/exploringourfluidearth/physical/density-effects/circulation-marginal-seas-and-estuaries.

[22] G. P. Schramkowski, H. E. De Swart, and H. M. Schuttelaars. Effect of bottom stress formulation on modelled flow and turbidity maxima in cross-sections of tide-dominated estuaries. *Ocean Dynamics*, 60(2):205–218, 2010. doi: 10.1007/s10236-009-0235-0.

[23] E. Schulz, H. M. Schuttelaars, U. Gräwe, and H. Burchard. Impact of the depth-to-width ratio of periodically stratified tidal channels on the estuarine circulation. *Journal of Physical Oceanography*, 45(8):2048–2069, 2015. doi: 10.1175/JPO-D-14-0084.1.

[24] K. Schulz, H. Burchard, V. Mohrholz, P. Holtermann, H. M. Schuttelaars, M. Becker, C. Maushake, and T. Gerkema. Intratidal and spatial variability over a slope in the Ems estuary: Robust along-channel SPM transport versus episodic events. *Estuarine, Coastal and Shelf Science*, 243, 2020. doi: 10.1016/j.ecss.2020.106902.

[25] E. A. Spiegel and G. Veronis. On the Boussinesq Approximation for a Compressible Fluid. *The Astrophysical Journal*, 131:442–447, 1960. doi: 10.1086/146849.

[26] G. S. Stelling. On the construction of computational methods for shallow water flow problems. Technical report, Rijkswaterstaat, The Hague, 1984.

[27] A. Valle-Levinson, C. Reyes, and R. Sanay. Effects of bathymetry, friction, and rotation on estuary-ocean exchange. *Journal of Physical Oceanography*, 33(11):2375–2393, 2003. doi: 10.1175/1520-0485(2003)033<2375:EOBFAR>2.0.CO;2.

[28] J. van Kan, A. Segal, and F. Vermolen. *Numerical Methods in Scientific Computing*. Delft Academic Press, Delft, 2nd edition, 2014. ISBN 9789065623638.

[29] F. Vilas, B. Rubio, D. Rey, and A. M. Bernabeu. *Encyclopedia of Planetary Landforms*, chapter Estuary. Springer, New York, NY, living edition, 2014. doi: 10.1007/978-1-4614-9213-9_621-1.

[30] C. B. Vreugdenhil. *Numerical methods for shallow-water flow*. Kluwer Academic Publishers, Dordrecht, 1994. ISBN 9780792331643.

[31] C. Vuik, F. J. Vermolen, M. B. van Gijzen, and M. J. Vuik. *Numerical methods for ordinary differential equations*. Delft Academic Press, Delft, 2nd edition, 2015. ISBN 9789065623737.

[32] K. C. Wong. On the nature of transverse variability in a coastal plain estuary. *Journal of Geophysical Research*, 99(C7):14209–14222, 1994. doi: 10.1029/94JC00861.

[33] Z. Yang, H. E. de Swart, H. Cheng, C. Jiang, and A. Valle-Levinson. Modelling lateral entrapment of suspended sediment in estuaries: The role of spatial lags in settling and M4 tidal flow. *Continental Shelf Research*, 85:126–142, 2014. doi: 10.1016/j.csr.2014.06.005.

[34] T. J. Zitman and H. M. Schuttelaars. Importance of cross-channel bathymetry and eddy viscosity parameterisation in modelling estuarine flow. *Ocean Dynamics*, 62(4):603–631, apr 2012. doi: 10.1007/s10236-011-0513-5.